

Analysis of Complex Microwave Structures Using Suitable Computational Electromagnetic Techniques

Dissertation

zur Erlangung des akademischen Grades

Doktoringenieur (Dr.-Ing.)

von M.Tech. Ayan Kumar Bandyopadhyay

Geb. am 25.11.1976 in Kolkata, Indien

genehmigt durch

die Fakultät für Elektrotechnik und Informationstechnik

der Otto-von-Guericke Universität Magdeburg



Gutachter:

Prof. Dr. A. Omar

Prof. Dr. M. Leone

Dr. R. Wanzenberg

Promotionkolloquium am: 20.12.2007

Acknowledgements

This work has been carried out at the *Chair of Microwave and Communication Engineering, Otto-von-Guericke University, Magdeburg*. I owe a lot to my teachers, colleagues and friends for their support, encouragement and help during my doctoral studies.

At first, I would like to thank my supervisor Prof. A.S. Omar for providing me the opportunity to work under his supervision. I am truly grateful and indebted to him for always being supportive and a source of inspiration towards me. I owe a great deal to Dr. A. Jöstingmeier and Dr. R. Wanzenberg for their guidance in carrying out the works related to PETRA III and for the valuable suggestions and corrections while writing the thesis. Without their support it would be very difficult for me to finish this work. I am thankful to Dr. C. Tomassoni and Prof. M. Mongiardo of the *University of Perugia, Italy*, for their support and cooperation concerning the GMT related work. I am also indebted to my colleagues Mr. N. Spiliotis, Mr. M. Anis, Dr. O. Aly and Dr. T. Meyer for their support and help whenever it was necessary. My sincere thanks to all other members and colleagues at the *High Frequency and Communications* group in the *Faculty of Electrical Engineering* for their friendly assistance during my entire stay in this group.

I would like to express my sincere gratitude towards all of my friends in Magdeburg, who have provided me a home away from my home. I would specially mention Dr. J. Akhtar, Dr. B.V. Mishra and his family, Dr. J. Gangadwala, Dr. M. Tulapurkar, Mr. N. Spiliotis for their unconditional and unlimited support during the beginning phase of my stay in a foreign country. I am also very thankful to Mr. S. Kavuri, Mr. F. Haroon, Dr. A. Fatima, Dr. K.P. Chary and his family, Dr. S. Ganesan and his family, Dr. S. Pervez, Ms. R. Raithore, Mr. Y. Gokhale and Dr. S. Baksi for their help and support. I owe a lot to my sister Mrs. C. Singh and Dr. J. Kumar for the encouragement and support, especially during the finishing phase of the thesis work. I am also thankful to others who have helped me during my stay in Magdeburg whom I might have forgotten to mention unknowingly and unintentionally.

I am grateful to my friends Mr. S. Mozumdar, Mr. S. Chatterjee, Dr. K. Chatterjee, Mr. K. Chakraborty, Mr. A. Kumar, Mr. H. Rahman, Mr. A. Bera and Mrs. R. Shyam for their support and encouragement - in spite of being at different parts of the globe.

I would like to express my thanks and regards to my teachers in India for their constant support and inspirations. I want to express my gratitude to Dr. A.K. Sharma of *CEERI*, India, for his constant encouragement and support. I am also indebted to Dr. R.S. Raju, Prof. B.N. Biswas, Prof. B.C. Sarkar, Dr. A. Bose, Dr. D. Mandal and my other beloved teachers for always encouraging me to pursue doctoral studies.

I want to express my hearty gratitude towards every member of my extended family, my friends and well-wishers in India. It would never be possible for me to pursue doctoral studies in a foreign country without their unconditional love, support and blessings. Finally, I want to express my deepest appreciation towards my parents. They have always been a constant source of inspiration and encouragement to me. Their blessings and love have always shown me the way out whenever I felt myself entangled in problems. Hence, I dedicate this dissertation to my beloved parents and my family.

A.K. Bandyopadhyay
Magdeburg, December, 2007.

Zusammenfassung

Diese Dissertation befasst sich mit einigen Anwendungen von elektromagnetischen Feldberechnungen im Mikrowellenbereich. Im Rahmen dieser Arbeit werden dreidimensionale elektromagnetische Simulationstools zur Modellierung, Charakterisierung und Analyse von verschiedenen Mikrowellenkomponenten verwendet. Zu diesem Zweck werden moderne kommerzielle elektromagnetische Simulationstools basierend auf der Finiten-Integrations-Technik und nicht kommerzielle Programme basierend auf der Generalized-Multipole-Technik Mode-Matching-Technik Hybridmethode benutzt. Die kommerziellen Simulationstools wurden zur Analyse von zwei komplexen Anwendungsfällen und die nicht kommerziellen Programme zur Charakterisierung von abstrahlenden Aperturen verwendet. In diesem Zusammenhang wurden numerische Methoden, die auf Matrizenzerlegung basieren, zur Identifizierung von redundanten Multipole vorgestellt. Durch Entfernung der redundanten Multipole kann die Generalized-Multipole-Technik Mode-Matching-Technik Hybridmethode verbessert werden.

Die erste Anwendung bezieht sich auf PETRA III, eine Synchrotron-Lichtquelle der dritten Generation. Mehrere Komponenten von PETRA III (Strahlungsmonitore an zwei Stellen des Strahlrohres sowie ein longitudinales Feedback-Cavity) wurden in Hinblick auf Wakefelder, Impedanzen, verschiedener Verlust- und Kickparameter detailliert untersucht. Außerdem wurden für diese Komponenten Modalanalysen durchgeführt. Den Einfluss des sogenannten ‘Nose cones’ auf die Eigenschaften des Feedback-Cavities sowie des Auftretens von Trapped-Moden in der Nähe (des Knopfes) des Strahlungsmonitors wurden ebenfalls untersucht.

Die zweite Anwendung befasst sich mit der Modellierung und Analyse einer Ultrabreitband-Antenne für die Kommunikation im Hf-Bereich. Zur Bestimmung der Parameter, welche die Eigenschaften dieser Antenne wesentlich beeinflussen, wurde ihre komplexe Form modelliert und analysiert. Unter Verwendung der Ergebnisse der Analyse ist es möglich, die Antenne für verschiedene Anwendungszwecke anzupassen. Eine optimierte Version dieser Antenne wird mit den dazugehörigen Messergebnissen präsentiert.

Der dritte Schwerpunkt ist die Charakterisierung abstrahlender Aperturen unter Verwendung einer Hybridmethode, welche sich aus der Generalized-Multipole-Technik und der Mode-Matching-Technik zusammensetzt. Ein kritisches Problem dieser Methode ist die Verteilung der Multipole entlang der

Antenne. Unpassend platzierte Multipolen oder die Verwendung von redundanten Multipolen verursachen eine numerische Instabilität, die wiederum zu ungenauen Ergebnissen führt. Zwei Algorithmen zur Bestimmung der redundanten Multipolen wurden vorgeschlagen und am Beispiel einer Hornantenne mit elliptischer Apertur getestet. Diese Algorithmen beruhen auf zwei bekannte Verfahren zur Zerlegung von Matrizen. Die Effektivität der beiden Algorithmen wurde überprüft, indem die tatsächlichen Randbedingungen mit den berechneten verglichen wurden. Außerdem wurde ein Vergleich der Fernfeldcharakteristik simuliert mit einer kommerziellen Finiten-Integrations-Technik Software und der vorgestellten Hybridmethode durchgeführt.

Abstract

This thesis is concerned with the application of computational electromagnetics in the area of microwave engineering. Within the framework of this thesis, three-dimensional computational electromagnetic tools have been used for the modeling, characterization, and analysis of several microwave components. State-of-the art commercial electromagnetic simulation tools based on the finite integration technique and a non-commercial code based on the generalized multipole technique-mode matching technique hybrid method have been used for the computations. The commercial simulation tools have been applied to two real life complex applications, whereas the non-commercial code has been used for characterization of radiating apertures. In this context, some numerical techniques based on matrix decompositions to identify the redundant multipoles have been proposed to improve the generalized multipole technique-mode matching technique hybrid method.

The first application is concerned with the third generation synchrotron radiation facility, PETRA III. Several components (the button type beam position monitors at two sections of the beam pipe, the longitudinal feedback cavity) of PETRA III have been extensively analyzed in terms of wakes, impedances, various loss and kick parameters and modal analysis. The effect of the ‘nose cones’ on the characteristics of the longitudinal feedback cavity, occurrence of trapped modes near the beam position monitor button have also been investigated in this context.

The second application involves the modeling and analysis of an ultra-wideband antenna for microwave communication. The complex shape of the antenna has been modeled and analyzed to identify the crucial parameters influencing the antenna characteristics. Based on this analysis and studies of the antenna, it can be adapted for several applications. An optimized version of the antenna has been presented along with the corresponding measurements.

The third application is concerned with the characterization of radiating apertures using a hybrid method involving generalized multipole technique and mode matching technique. One of the crucial issues in this method is the multipole distribution along the antenna. Improperly placed multipoles, or presence of redundant multipoles, cause severe numerical instability leading

to inaccurate results. Two algorithms to identify the redundant multipoles have been proposed and applied in the case of horn antennas with elliptical apertures. These algorithms are based on two well-known matrix decomposition methods. The effectiveness of both approaches have been validated by comparison of the actual boundary conditions with the computed ones. Additionally, comparisons between the far-field patterns obtained from a commercial finite integration technique software and the proposed hybrid method have also been presented.

Contents

1	Introduction	1
1.1	A brief historical review of electromagnetic field theory	1
1.2	Overview of some widely used numerical techniques in CEM	2
1.2.1	Method of Moments	3
1.2.2	Finite Difference Time Domain Method	4
1.2.3	Finite Integration Technique	5
1.2.4	Finite Element Method	5
1.2.5	Transmission Line Matrix Method	7
1.2.6	Generalized Multipole Technique	8
1.2.7	Mode Matching Technique	8
1.3	Contributions presented in this thesis	9
1.4	Organization of this thesis	12
2	The Finite Integration Technique	15
2.1	Prologue	15
2.2	Theoretical formulation	15
2.2.1	Discretization of Maxwell's equations	15
2.2.2	Maxwell's grid equations in time domain	21
2.2.3	Stability condition	22
2.2.4	Excitation	22
2.2.5	Termination of the computation domain	23
2.3	Commercial CEM tools based on the FIT	24
2.3.1	Microwave Studio	24
2.3.2	MAFIA	24
3	Wake Computations and Related Analysis for PETRA III	27
3.1	Prologue	27
3.2	Synchrotron radiation facilities	28
3.3	Theoretical basics	29
3.3.1	Wakefields and impedances	29
3.3.2	Relationships between resonant cavity parameters and the beam	31
3.4	Wake computation procedure	34
3.4.1	Using MAFIA for wakefield computations	34

CONTENTS

3.4.2	Wake computations for large structures with off-axis beam	35
3.5	Simulation results for PETRA III beam position monitors	40
3.5.1	Beam Position Monitor	40
3.5.2	Eigenmode computation results for BPMs in the normal beam pipe	41
3.5.3	Time domain computations for BPMs in the normal beam pipe . .	44
3.5.4	Eigenmode computation results for BPMs in the narrow beam pipe	52
3.5.5	Time domain computations for the BPMs in the narrow beam pipe	55
3.6	Simulation results for PETRA III longitudinal feedback cavity	59
3.6.1	Longitudinal feedback cavity	59
3.6.2	Eigenmode computation results	60
3.6.3	Time domain computations	64
4	Analysis of an Ultra-wideband Antenna	75
4.1	Prologue	75
4.2	Theoretical Basics	76
4.2.1	Radiation field regions of an antenna	76
4.2.2	Definitions of different antenna parameters	77
4.3	Geometry of the antenna under analysis	80
4.4	Modeling of the antenna	80
4.5	Simulation and measurement results	82
4.5.1	Excitation	82
4.5.2	Convergence studies	84
4.5.3	Parametric studies	86
4.5.4	The effect of the loop	89
4.5.5	Comparison between simulations and measurement	92
5	Application of a Hybrid Method to Characterize Radiating Apertures	95
5.1	Prologue	95
5.2	Theoretical basics	97
5.2.1	The Generalized Multipole Technique	97
5.2.2	The GMT-MMT hybrid technique for characterization of radiat- ing apertures	98
5.2.3	Problems of ill conditioning	103
5.2.4	Solution approaches	103
5.3	Simulation results	106
5.3.1	Simulation results: SVD-angle method	107
5.3.2	Simulation results: RRQR method	110
5.3.3	Comparison of the radiation patterns	111
6	Summary and Future Works	113
	Bibliography	117

Nomenclature

Acronyms

ABC	Absorbing boundary condition
BPM	Beam position monitor
CEM	Computational electromagnetics
MGE	Maxwell's grid equations
RRQR	Rank Revealing QR (factorization)
EBCM	Extended boundary condition methods
FDFD	Finite difference frequency domain
FDTD	Finite difference time domain
FEM	Finite element method
FIT	Finite integration technique
FVTD	Finite volume time domain
GMT	Generalized multipole technique
HOM	Higher order mode
MMT	Mode matching technique
MoM	Method of moments
PML	Perfectly matched layer
RADAR	Radio detection and ranging
RFID	Radio frequency identification
RF	Radio frequency

Nomenclature

SVD	Singular value decomposition
TEM	Transverse electric and magnetic
TE	Transverse electric
TLM	Transmission line matrix
TM	Transverse magnetic

Symbols

B	Magnetic flux density vector
b	Magnetic flux
D	Electric flux density vector
d	Electric flux
Δt	Time step
Δx	Step size in the x direction
Δy	Step size in the y direction
Δz	Step size in the z direction
E	Electric field vector
e	Electric voltage
H	Magnetic field vector
h	Magnetic voltage
J	Current density
j	Total electric current
$[\mathbf{M}_\sigma]$	Conductivity matrix
$[\mathbf{M}_\varepsilon]$	Permittivity matrix
$[\mathbf{M}_\mu]$	Permeability matrix
q	Electric charge
ρ	Electric charge density
<i>c</i>	Speed of light in vacuum

F	Force
j	Imaginary unit
k_{\parallel}	Total loss parameter
k_{\perp}	Kick parameter
λ	Line density
ω	Angular frequency
p	Momentum
P	Power
Q	Quality factor
R_{shunt}	Shunt impedance
s	Distance in bunch coordinate
t	Time
U	Total energy
W^{δ}	Wake potential due to a point charge
W_{\perp}	Transverse wake potential
Z_{\parallel}	Transverse impedance
Z_{\perp}	Transverse impedance
ϵ_0	Permittivity of free space
$[I]$	Identity matrix
μ_0	Permeability of free space
ς	Singular value

Chapter 1

Introduction

1.1 A brief historical review of electromagnetic field theory

Electromagnetics is concerned with interrelated electric and magnetic fields, an effect which occurs when the two fields are time-varying. Although interest in static electricity and magnetism dates back to ancient times, the cornerstone of modern electromagnetic theory is the mathematical formulation of the propagation of electromagnetic waves by James Clerk Maxwell [1, 2]. The works of Maxwell are based on the earlier theoretical and empirical knowledge developed by Gauss, Ampere, Faraday and others. Later, Oliver Heaviside transformed the whole formulation of Maxwell into its modern vector form removing many of the mathematical complexities and provided a foundation for practical applications of guided waves and transmission line [3]. Although Maxwell's equations are of great importance and together with the continuity relations at the boundaries and other auxiliary relations form the basics of modern electromagnetics, many scientists of Maxwell's time were skeptical of his theories. The first experimental proof of the electromagnetic theory of Maxwell was provided by a set of experiments by Heinrich Hertz during 1887-1891 [4].

Hertz's work inspired a number of scientists around the globe to get involved in the investigation of electromagnetic waves. In 1892, Nikola Tesla delivered a widely reported presentation before the Institution of Electrical Engineers of London in which he noted, among other things, that information could be transmitted without wires by the electromagnetic waves [5]. During 1894-1900, J.C. Bose carried out researches to generate and investigate the optical properties of microwave (mm waves) and used the same for signaling purposes [6, 7]. Bose reported on his microwave (millimeter-wave) experiments to the Royal Institution and other societies in England in 1897. Around the same time, Alexander Popov demonstrated the transmission of radio waves between different campus buildings in St. Petersburg [8]. The first practical application of the concepts of electromagnetism came from Marconi when he took a patent in England on a system of "wireless telegraphing" in 1896 and later was able to demonstrate the

1. Introduction

transmission and reception of electromagnetic waves across the Atlantic Ocean [9].

The concept of relativity by Albert Einstein [10, 11] has shown that the gravitation and electromagnetics are related to each other and predicted that the electromagnetic waves passing by a massive star would be bent or reflected. Later the confirmation of this prediction has led to the search of an “unified field theory” or a “theory of everything” in which Maxwell’s equation would be a special case. Such a unification has not been yet achieved, but its realization remains as a major goal of modern physics and electromagnetics till date [12, 13, 14].

The electromagnetic field theory got much attention and a boost during the World War II mainly for military applications of radar systems. The desire for radars operating at microwave frequencies put high priority on the works related to waveguides, waveguide devices, antennas etc. A variety of devices were developed to replace low-frequency lumped circuit elements. Along with these devices, the underlying theories, methods of analysis were also developed. Various mathematical concepts and tools were proposed and applied to solve Maxwell’s equations for design and analysis of radio frequency components and devices. Most of the numerical techniques and theories upon which the modern electromagnetic computations rely on have been initiated and formulated during the 1960s. The next section will provide a brief survey of the widely used numerical techniques today.

Since the last few decades the computational electromagnetics (CEM) techniques have been conceptualized, developed and matured to such a level that it forms an essential part of the current radio frequency (RF) and microwave engineering activities. CEM has now become a multi-disciplinary field with electromagnetic and numerical methods being at the central subject. Other constituents of modern CEM techniques include geometrical modeling and visualizations, mathematical algorithms, computer science etc. The CEM techniques not only allow to test a device before prototyping, it also provides a strong insight into the functioning of the device. From the viewpoint of research, this is a very important feature and in some cases is more valuable than the proper functioning of the particular device itself. The applications of CEM are complex, vast and almost impossible to count in numbers. Some of the areas at present in which CEM is extensively used include the applications in aviation and communications, biomedical devices and health, high speed circuits and switches, electronic packaging, geophysical prospecting, non-destructive testing, nuclear and particle physics applications in particle accelerators, medical diagnosis and imaging, industrial heating and drying etc.

1.2 Overview of some widely used numerical techniques in CEM

The industrial and engineering demands for sophisticated electromagnetic modeling for a wide range of applications are continuously increasing. This ever increasing demand has made computational electromagnetics into an “industry” of its own, involving a

1.2 Overview of some widely used numerical techniques in CEM

large number of researchers in academic, government and industrial laboratories. As a consequence, the number of methods, techniques, algorithms and their variations involved with computational electromagnetics have become almost innumerable. Many criteria may be used to classify the techniques involved in CEM, like the domain in which they are operating (time/frequency), the type of equations on which they are based (integral/differential), the dimensionality of the problem (two-dimensional/three-dimensional) etc. However it is extremely difficult to distinctly classify the techniques based on such criteria, as many of them share common features or are interconnected with each other. In this section, some of the state-of-the-art numerical techniques which are widely used in CEM will be briefly discussed along with their advantages and disadvantages.

1.2.1 Method of Moments

The method of moments (MoM), also known as the method of weighted residuals, is widely used in CEM, especially for the antenna engineering. Development of this method was initiated in Russia [15]. This method has become popular since the works of Richmoned and Harrington [16, 17]. Detailed information about the early history and development of the MoM can be found in [18] by Harrington. It has been successfully applied to a wide variety of electromagnetic problems like the thin wire antennas and arrays, scattering problems, analysis of microstrips etc.

In this method, an appropriate integral equation is derived for the problem under consideration. At the next step this integral equation, which typically involves surface currents, is discretized into a matrix equation using proper basis functions and weighting functions. The Greens functions [19] are widely involved in this procedure. Afterwards, the matrix elements are evaluated and finally the corresponding linear system of equations is solved using a suitable solver. From the solution, the parameters of interest are evaluated. Usually the MoM is applied in the frequency domain, so the matrices involved in this method are fully populated with complex valued entries. Some time-domain integral equation formulations are also reported in the literature [20]. Usually, a marching on time (MOT) scheme is implemented in such formulations. However, usage of the MoM in the time domain is very limited till now, mainly for the stability related issues.

The main advantage of the MoM is that highly conducting surfaces can be treated very efficiently. With this method only the surfaces are needed to be discretized - it is not needed for the whole computational volume. This makes the method computationally efficient for the problems with small surface/volume ratio. The radiation condition is automatically incorporated, requiring no additional computational efforts. Extension of this method towards stratified media can efficiently be formulated increasing its applicability.

There are also some weak points of the MoM formulation. Firstly, it can not handle the electromagnetically penetrable materials very efficiently. Secondly, the computational requirements for the MoM increase very sharply with increasing frequency. So

1. Introduction

for high frequency applications, this method can be computationally inefficient compared to other techniques. This problem becomes even worse in the cases where an inhomogeneous meshing is required.

A large number of commercial and non-commercial softwares are available based on MoM. The “Numerical Electromagnetic Code (NEC) - Method of Moments” which is popularly known as “NEC2” is one of the widely used non-commercial MoM software. The state-of-the-art softwares based on the MoM includes “FEKO” [21], “SONNET” [22], “superNEC” [23], “GEMACS” [22] etc.

1.2.2 Finite Difference Time Domain Method

The finite difference time domain (FDTD) method is based on direct discretization of Maxwell’s equations in their differential form [24]. It is one of the most popular techniques based on finite differences. The application of finite difference method in computational electromagnetics was initiated around 1920 under the title “the method of squares” [25]. In general, the finite difference techniques approximate Maxwell’s equations by difference equations. A number of finite difference schemes exist with different accuracies, convergence and complexities in the approximation of the differentials. Under these schemes, the value of the dependent variable at a point in the solution region is related to the values at some neighboring points. There are plenty of finite difference techniques applied in CEM besides the FDTD method e.g. the finite difference frequency domain (FDFD) method, finite volume time domain (FVTD) method etc. All of these methods are quite similar in formulation, sharing the common advantages and disadvantages. The FDTD method was first proposed by Yee in 1966 [26]. Due to the higher computational cost and the difficulty to model open problems, it was not widely used at the beginning. Later, advent of the techniques like the absorbing boundary condition (ABC), perfectly matched layers (PML) [27, 28] etc. have made this method capable to model open problems. The exponential increment in the computational power have made this method extremely popular in the recent days.

In FDTD method, the whole computation domain is discretized into a grid of nodes where the electric and magnetic field values are evaluated. Different material properties can be assigned to different mesh cells, enabling a straightforward way to model inhomogeneous media. Usually the electric and magnetic field grids are spatially and temporally offset from each other. These spatial and temporal offsets are closely related to the stability and accuracy of the scheme. The present values of the electric or magnetic fields throughout the whole computational domain are obtained from the past field values, using the update equations derived from the Maxwell’s equations. The update equations are used in a leapfrog scheme to incrementally march the electric and magnetic fields forward in time [26]. This implies that the electric fields are updated at the middle of each time step between successive magnetic field updates, and vice versa.

There are several advantages of the FDTD method. The method relies on a versatile and simple modeling technique. This makes the application of this method very simple and straightforward. Being a time domain technique, a broad band frequency response

1.2 Overview of some widely used numerical techniques in CEM

can be obtained from a single simulation. Since this method computes the electric and magnetic fields at each grid point, it is possible to have an animated view of the fields. This can provide a very useful insight for design and optimization of microwave devices. Modeling of inhomogeneous media of magnetic media can be readily realized with FDTD.

The main weakness of the FDTD method is that the entire computational domain has to be discretized resulting in very large computational domains for some problems. This leads to very long computation times for such problems. This problem becomes severe for large structures containing some tiny complex features. In this case, the spatial resolution (grid or mesh size) must be kept small for modeling the tiny part precisely - resulting a manyfold increase in computational effort. The open problems cannot be solved straightforwardly with this method, approximations like the ABCs or PMLs are to be used in this case. Although the electric and magnetic fields are computed at each grid points, the farfield computations (which is a key requirement for the antenna problems) cannot be done in a straightforward way. Usually the near field to far field transformations are used for this purpose which usually require extensive computational efforts.

Plenty of commercial and non-commercial FDTD codes are available, because of the simplicity of the method. Among the popular non-commercial FDTD codes, “MEEP” [29] from Massachusetts Institute of Technology (MIT), “EM Explorer” [30] etc. can be mentioned. The widely used commercial softwares based on FDTD include “XFDTD” [31], “SEMCAD X” [32], “FIDELITY” [33], “Empire” [34] etc. The commercial codes and in some cases also the non-commercial codes include user friendly visualization tools and the necessary post processing tools.

1.2.3 Finite Integration Technique

The finite integration technique (FIT) is based on a consistent discrete representation of Maxwell’s equations on grids. It was first proposed in frequency domain by T. Weiland [35]. In this method the integral form of the Maxwell’s equations are used for discretization, instead of the differential form. This method coincides with the FDTD method when it is used in time domain together with the leapfrog time stepping scheme. It can be considered as a generalization of the FDTD method [36] sharing the similar pros and cons of the earlier one. The FIT will be discussed in more detail in chapter 2.

The widely used commercial softwares based on FIT are “Microwave Studio” and “MAFIA” [37, 38], both from Computer Simulations Technology (CST). These two softwares have been extensively used for most of the simulations presented in this thesis.

1.2.4 Finite Element Method

The finite element method (FEM) is a very powerful and versatile numerical method capable of modeling complex geometries and inhomogeneous media. However the FEM

1. Introduction

formulation is more complex than the MoM or the FDTD method. The FEM was originated from the need to solve complex elasticity, structural analysis problems in civil and aeronautical engineering. Its development can be traced back to the works by Hrennikoff and Courant [39, 40]. The applications of finite element method in electromagnetics began in the late 1960s for the analysis of waveguides and cavities [41]. In the beginning, its applications in electromagnetics were limited to the closed boundary problems because of the problem of terminating the computation domain in case of open boundary problems. Later developments of the concepts like the absorbing boundary conditions, perfectly matched absorbers etc., have resulted in successful application of the FEM to the open domain problems in scattering, microwave circuits and antennas. The generality of this method makes it possible to build general purpose computer programs which can be applied to solve a wide range of problems.

The FEM can be formulated mainly with two approaches - the first one is using the variational analysis and the second one is using the method of weighted residuals. In the first approach, the partial differential equation form of the Maxwell's equations is chosen. Afterwards a variational function is found whose extremal point, subject to certain boundary condition, corresponds with the solution of the problem. The second approach also starts with the partial differential form of Maxwell's equations and then a weighted residual is introduced. At the next stage, one of the differentials in the partial differential equation is shifted to the weighting function using Green's theorem. In both approaches, the unknown field is discretized using a finite element mesh. Usually meshing for the surface areas are formed with triangular elements and tetrahedral elements are used for volumetric meshes. Other types of mesh elements can also be used, but the triangular and tetrahedral shapes are the simplest geometrical forms to mesh two and three dimensional geometries.

There are several advantages associated with the FEM. With this method, complex geometries and inhomogeneous media can be straightforwardly and conveniently treated. With FEM, each mesh element can be defined independently. Thus, a large number of fine mesh elements can be used in regions with complex geometry and fewer, larger elements can be used in relatively simpler or open regions. This feature allows an efficient modeling of complex and large structures. Being a general method, this method has the potential to couple many problems like the mechanical, thermal and electromagnetic problems together. Commercial software packages on this subject have already been developed, specially for the high power applications - coupling electromagnetics and thermal analysis.

One of the weak points of the FEM is: it does not include the radiation condition. As a consequence, implementation of absorbing boundaries are musts to solve problems with open boundaries. Secondly, for large three dimensional problems, the FEM mesh can be very complex. In some cases the required time to mesh a certain structure can be larger than the time required for the field commutation. The FEM method is more complex to implement than the FDTD method.

As FEM is a quite mature computational technique and is applicable to solve many problems related to several branches of physics, there are many commercial and non-

1.2 Overview of some widely used numerical techniques in CEM

commercial computer programs available. Some public domain libraries are also available including FEM discretization, FEM solvers and related problems. Among the most popular FEM softwares in electromagnetics the “HFSS” package from “Ansoft” [42], “HFWORK” from “ElectroMagneticWorks” [43], “COMSOL RF module” [44] can be mentioned. Most of them also provide modules to analyze coupled problems.

1.2.5 Transmission Line Matrix Method

The transmission line matrix (TLM) or the transmission line modeling is a numerical method to solve field problems using their circuit equivalent [45, 46]. It is based on the equivalence between Maxwell’s equations and the equations for the voltages and currents on a mesh of continuous two-wire transmission line. Although the idea of replacing a complex electric network by a simple equivalent circuit is very old, the idea of applying the same in the scattering problems is due to Johns and Beurle [47]. The performance of the TLM is better at higher frequencies where the transmission and reflection properties of geometrical discontinuities cannot be considered as lumped elements. The symmetrical condensed node formulation is widely used for the three-dimensional TLM analysis [48].

The TLM method is a time-domain technique and depends on a discretization process. In this method, the problem is at first replaced by the equivalent network using transmission lines. The whole solution domain is discretized into a rectangular mesh of transmission lines, interconnected with each other at different nodes. Each node is connected with its neighboring node with a pair of orthogonally polarized transmission lines. Dielectric loading can be realized by loading the appropriate nodes with reactive stubs. These stubs are usually half the length of the mesh spacing having a characteristic impedance appropriate for the desired loading. The termination of the mesh at the boundary of the solution domain is accomplished by terminating the boundary node transmission lines with corresponding characteristic impedances.

The main advantage of the TLM method is that, it is based on a relatively simpler formulation than the FEM. This method is flexible and can be used to model arbitrary and complex structures. Inhomogeneous media can be modeled very conveniently, and the impulse response and time domain performance of the system can be obtain straightforwardly. Also this technique can be implemented into parallel machines.

Some disadvantages of the TLM method can also be noted in this context. This method relies on rectangular meshing. Therefore, the number of mesh cells to accurately model complex structures becomes very large. The smallest size of the mesh cell is determined by the smallest details of the structure. Thus large structures having some small complex geometries usually require large and dense grids. This problems become more severe for the structures containing large free space regions. In these situations, hybridization of this method with some other method (e.g integral equation method) can be a better choice in terms of computational efficiency [49].

The commercial softwares FLO/EMC from FLOMERICS [50] and MEFiSTo from FAUSTUS Scientific Corporation [51] are based on the TLM method.

1. Introduction

1.2.6 Generalized Multipole Technique

The generalized multipole technique (GMT) is a frequency domain technique for electromagnetic field computation [52]. Researches in this topic have been carried on by different groups using different names for the method [53, 54, 55].

The generalized multipole technique is based on the method of weighted residues. The expansion functions used in this method are analytic solutions of the fields generated by sources (multipoles) located at some distance from the boundary surfaces. The scattered field is expressed as the weighted summation of the fields radiated by the multipoles. Boundary conditions are enforced to the scattered field as expressed with the help of the expansion functions. This gives rise to a system of linear equations which is then solved to determine the strengths of the expansion functions. The accuracy of the method depends largely on the number and locations of the multipoles. Since the multipole fields are already solutions of the spherical wave equations, the radiation conditions are readily satisfied and the fields can be directly calculated. This method will be discussed in detail in the chapter 5.

One of the advantages of the generalized multipole technique is that it requires less computational efforts as it does not require discretization of the whole computation domain. The radiation conditions are readily satisfied and the far fields can be directly computed. This method also provides the possibility to directly estimate errors in field computations, avoiding the time consuming convergence tests.

There are also some disadvantages of the GMT. In this method, the field computation is largely dependent on the locations and number of the multipoles. The presence of redundant multipoles lead to serious erroneous results. As this is a frequency domain technique, the computations are to be repeated (including the multipole placement) at each frequency point to obtain a broad-band response.

A three dimensional commercial software based on the GMT is the MAX-1 [56]. The non-commercial versions of this software are also available from the ETH, Zurich.

1.2.7 Mode Matching Technique

The mode matching technique (MMT) is a semi analytical frequency domain technique best suited for the analysis of closed structures. It is one of the widely used CEM techniques and has been initiated mainly for studies of waveguide discontinuities [57, 58]. This method has been very successfully applied to analyze problems like waveguide junctions, discontinuities, corrugated sections, waveguide arrays, cavity resonators, accelerating structures etc.

In this method the fields inside the closed structures are expressed as a series expansion using analytical solutions of the Maxwell's equations as the basis functions (modes). The Fourier series or the Fourier-Bessel series are extensively used for this purpose. For the analysis of discontinuities, the whole structure is subdivided into a number of subdomains. Fields in each subdomain are expressed individually as the summation of several modes with unknown strengths. By enforcing the matching of the

fields at the common interfaces, the unknown strengths of the modes can be found out. The complete solution of the whole structure can be found out by proper cascading the solutions for each subdomain.

The main advantages of this method include very fast and computationally efficient field computations, as discretization of the computational domain is not required. In case of large structures, the computation domain can be divided into smaller subdomains. Each sub-domain can be analyzed separately and then the results can be combined to obtain the response of the whole structure.

The main drawback of this method is, it is best suited for the closed structures or structures with semi-infinite extents. Analysis of open problems are possible for very limited geometries or when it is combined with some other suitable methods. Another limitation of this method is, the structure under analysis must be simple enough to have analytical basis functions. For the same reason, it is extremely difficult to efficiently analyze the structures having complex geometries with this technique.

Several computer programs based on mode matching technique are available with the books related to modal analysis, e.g. [59]. The commercially available program “WASP-NET” from “MiG” [60] includes a mode matching solver for electromagnetic analysis.

1.3 Contributions presented in this thesis

The area of CEM has undergone a vast development in the past years - giving rise to powerful electromagnetic simulation tools and techniques. The goal of all these techniques is to determine and predict performances of RF and microwave components, networks and machines in a very accurate and reliable way. The advent of powerful computers and computer systems allows us to analyze large and complicated structures, with the numerical efficiency and accuracy remaining at the focal point of today’s research interests. Each of the existing computational techniques, as has been seen in the previous sections, has their own merits and demerits. A significant amount of research works of today is being carried out with the goal to couple the advantages of one or more computational techniques, giving rise to different hybrid methods. Such hybrid methods usually combine the advantages of both the methods involved, thereby increasing either the computing efficiency or the memory efficiency or both. In this thesis, at first, the scope and capability of the modern CEM softwares to analyze complex microwave structures have been elaborated through two examples. Both the chosen examples are real life examples and are far apart from each other. The first example presented here represents a closed boundary problem whereas the second one belong to the category of open boundary problems. These two examples analyzed are:

1. Electromagnetic field computations and analysis of some components of a third generation synchrotron radiation facility, namely PETRA III, which is recently under development.

1. Introduction

2. Modeling and analysis of a ultra-wideband microwave antenna.

1. Electromagnetic field computation for PETRA III: In the synchrotron light sources, charged particle bunches with certain energy are circulated inside a metallic beam pipe maintained at high vacuum. Along some parts of the beam pipe, the particle bunches are subjected to traverse through certain devices ('insertion devices') which provide them predefined accelerations. As effects of these accelerations, the particle bunches emit synchrotron radiations. In course of traveling along the beam pipe, the particle beams pass through many discontinuities. It is known that whenever a charged particle bunch traverses any discontinuity along the beam pipe, it excites an electromagnetic field (wakefields or wakes). This field can ring there for a long period of time, or can propagated through the beam pipe depending upon the geometry of the discontinuity and the beam pipe. Any other particle bunch following the first bunch (or the same bunch after one cycle) has a chance of getting influenced by this field. Wakefields due to the leading part of a particle bunch (head of the bunch) can even affect rest of the bunch (tail of the bunch). During the design of an accelerator efforts are made to minimize these unwanted effects. In an accelerator, hundreds of pick-up devices (Beam Positioning Monitors), transitions, tapers, vacuum pump ports, etc., are present along the beam pipe. These are merely discontinuities in "view" of the particle beam. Hence they can generate considerable amount of wakefields. This part of the thesis is involved in estimations of wakefields due to some discontinuities in the PETRA III beam pipe, related analysis like the possibilities of excitation of trapped modes and characterizing these modes in terms of different parameters.

The Beam Position Monitors (BPMs) of a particle accelerator are pick-ups, which are used to measure the position of the particle beam circulating inside the metallic beam pipe. Reliable operation of the entire accelerator largely depends on the proper functioning and accuracy of the BPMs. In PETRA III, BPM systems with button pickups will be used for monitoring the beam. Computation of the calibration constants for the button type of beam positioning monitors, corresponding wake fields estimation, possibilities of any trapped modes near the BPM button etc., have been thoroughly analyzed in this section.

The multibunch operations in a particle accelerator are affected by various instabilities of the particle bunches, which quenches the maximum achievable current of the machine. One of the available remedies is to employ feedback systems to prevent the instabilities. These feedback systems usually consist of three parts. The first part measures the position or phase of the beam with the help of BPMs. The second part is the electronic and signal-processing part, which generates an appropriate correction signal based on a reference signal. The third part is the device, which delivers the correction signal to the beam, correcting its error.

The next section of the thesis is on the analysis of the longitudinal feedback cavity to be employed in PETRA III. The main goals of this study are to estimate the wakefields due to the cavity and to identify higher order modes (HOM) that may have negative influences on the beam performance. Another important design parameter of these type of cavities is the shunt impedance. The shunt impedance of such cavities describe how

efficiently the “kick” (energy corrections) is supplied to the beam by the cavity. Any improvement in the shunt impedance actually will lead to some decrease in the costs of the amplifiers. It is known that addition of “nose cones” can considerably increase shunt impedance of the feedback cavities. The effect of the nose cones on shunt impedances for the proposed PETRA III longitudinal feedback cavity has been studied. The increment of the shunt impedance due to the nose cones has been estimated and compared with the corresponding values for similar devices in operation.

2. Modeling and analysis of a ultra-wideband RF antenna: The antennas are essential parts of any RF communication systems which are used to transmit and receive electromagnetic signals. Numerous types of such devices are used in modern day communication systems, depending upon the application. The antenna which is investigated in this thesis is a compact, lightweight and inexpensive antenna having a very large bandwidth. Combination of these features makes it a strong candidate for various portable applications. The ultra-wideband characteristics of the antenna is achieved by means of a specially designed taper which minimizes reflections from the antenna edges and transitions. Due to its unconventional and complex shape, it is almost impossible to analyze the antenna analytically. This necessitates to model it with a electromagnetic simulator. A MATLAB [61] based program has been developed to create the unconventional geometry of the antenna inside the electromagnetic simulator. From the simulations, the crucial parameters influencing various antenna characteristics have been found out. Based upon these investigations, the antenna design has been customized for different applications and tested successfully. A more compact form of the same antenna has also been produced and successfully applied for the radio frequency identification (RFID) applications.

Most of the modern full-wave CEM techniques require discretization of the whole computational domain. This was also the case for the two examples presented earlier. In order to achieve numerically efficient computations with the available computer memory, one must define a finite computational domain enclosing the problem under analysis and rely on the ways to terminate the computational domain at the boundaries. Although this does not create a big problem for closed structures, but for the open structures the termination of the domain is a very important issue. Usually the termination is accomplished using some artificial absorbing layers at the domain boundaries, or terminating the domain with some perfectly matched layers. Although termination of the computational domain by means of these methods usually lead to quite accurate results for most of the practical applications, there is still some debate about the most appropriate termination methods and the appropriate distance of these layers from the domain boundaries. However, if some hybrid techniques involving two separate methods for the closed and open problems are used, this problem can be totally avoided. Such a hybrid method is presented afterwards which combines a computational method best suited to analyze closed problems with another one suitable to analyze open problems. This hybridization allows to analyze an open problem without the issues of artificially terminating the computational domain, whereas the internal part of the device under analysis can be analyzed with any numerical CEM technique.

1. Introduction

The generalized multipole technique, also called the multiple multipole technique, belongs to the category of “source methods”. As has been mentioned in 1.2.6, GMT can be conveniently used to analyze the open problems. Combination of the GMT with the mode matching technique (1.2.7) provides the possibility to analyze open problems combined with closed problems. A very common example of this type of problem are aperture antennas. The GMT-MMT hybrid method allows to realistically analyze this type of problems without discretizing the whole computation domain. Artificial approximations of the domain boundaries (like absorbing boundaries etc.) are not needed in this method, thus decreasing the computational effort. This method also provides an easy and straightforward way to estimate the error in the field computation.

The generalized multipole technique used in this context is a relatively new technique in computational electromagnetics. One of the major and crucial issues in this method is the proper placement of the sources or multipoles inside the computation domain. Improperly placed multipoles usually lead to large errors in the computed field. In order to counter this problem, some numerical techniques based on the decomposition of the system matrices have been proposed. These methods are capable to identify the wrongly placed or redundant sources in the system, so that they can be excluded. The proposed techniques have been applied successfully for field computation of radiating apertures and the results have been validated by comparing the results with those obtained using standard electromagnetic simulation tools.

1.4 Organization of this thesis

In the current chapter, at the beginning, a brief historical review of the CEM is provided. Short descriptions of the most used CEM techniques along with their merits and demerits are briefly discussed in this chapter. Afterwards the contributions in the field of CEM within the framework of this thesis is stated, which is followed by the organization the thesis.

In the second chapter a basic formulation of the FIT has been provided. Some related topics are discussed and basic features of the commercial CEM simulation tools Microwave Studio and MAFIA are presented.

The third chapter presents electromagnetic field computations related to the third generation synchrotron radiation facility PETRA III, using commercially available CEM tools. Wakefields, impedances and related electromagnetic analysis of some parts of PETRA III are reported in this section.

The fourth chapter is concerned with the electromagnetic analysis of a three dimensional ultra-wideband antenna. Modeling, parametric studies and investigations about the operation of the antenna using a commercial CEM tool are presented in this chapter.

The fifth chapter presents a hybrid method for analyzing radiating apertures. This hybrid method involves the semi-analytical CEM techniques GMT and MMT. After a brief introduction to these techniques, methods to overcome the critical problem of multipole placement are suggested. Simulation results for several cases implementing those

1.4 Organization of this thesis

techniques are presented and compared with the results obtained from the commercial simulation software.

The sixth chapter, which is also the last chapter of this dissertation provides summary of the works covered in the framework of this thesis.

Chapter 2

The Finite Integration Technique

2.1 Prologue

The finite integration technique (FIT) was proposed by T. Weiland as a computational tool to solve the Maxwell's equations [62]. This technique depends upon a discrete reformulation of Maxwell's equations in their integral form, making it suitable for numerical computations with the help of computers. In this technique, the six components of electric field strength and magnetic flux density are computed on a dual grid mesh system. This technique is based on a matrix formulation and can be applied to non-orthogonal coordinate systems in addition to the Cartesian coordinate system. It can be applied either in the frequency or in the time domain. The applications of the FIT has been extended to acoustic, elastic and piezoelectric wave propagations [63, 64]. The commercial software packages CST Microwave Studio and CST MAFIA (MAXwells Equations using Finite Integration Algorithm) [65] are directly based on this technique and are widely used as a state-of-the-art electromagnetic design and analysis tool. As these two software packages have been extensively used for the electromagnetic simulations in this thesis, the basics of the FIT is summarized in this chapter. It may be noted here that a detailed description of this method is beyond the scope of this chapter. Further details and elaborated description of this method can be found in [66, 67, 68].

2.2 Theoretical formulation

2.2.1 Discretization of Maxwell's equations

Computational electromagnetics deals with the problem to accurately compute the electromagnetic fields due to a device or structure of interest. In order to compute the electromagnetic fields with the help of a computer with finite memory, the first step is to define a finite calculation domain out of the infinite extent of the open boundary. The considered application problem is enclosed by this finite calculation domain. The Maxwell's equations in integral form, which are the governing equations used for the

2. The Finite Integration Technique

field computation in FIT are given by,

$$\oint \mathbf{E} \cdot d\mathbf{s} = - \int \frac{\partial \mathbf{B}}{\partial t} \cdot d\mathbf{A} \quad (2.1)$$

$$\oint \mathbf{H} \cdot d\mathbf{s} = \int \left(\frac{\partial \mathbf{D}}{\partial t} + \mathbf{J} \right) \cdot d\mathbf{A} \quad (2.2)$$

$$\oint \mathbf{D} \cdot d\mathbf{A} = \int \rho dV \quad (2.3)$$

$$\oint \mathbf{B} \cdot d\mathbf{A} = 0 \quad (2.4)$$

Here, \mathbf{E} and \mathbf{H} are the electric and magnetic field vectors, \mathbf{D} and \mathbf{B} are the electric and magnetic flux density vectors, ρ is the electric charge density and \mathbf{J} is the current density, respectively. The electromagnetic fields which are related to each other according to equations 2.1-2.4 are to be computed within the computational domain defined earlier. It may be noted that in this chapter the field quantities ($\mathbf{E}, \mathbf{H}, \mathbf{D}, \mathbf{B}$) are in the time domain.

In the next step, the computational domain is decomposed into a finite number of volumetric cells, termed as FIT cells. The FIT cells are formulated in such a way that they exactly fit to each other. In this way, the intersection of two different cells is either empty or a polygon, an one-dimensional edge, or a point shared by both the cells. This decomposition scheme yields the finite integration grid which serves as the computational grid.

Although the FIT allows non-orthogonal and irregular gridding, orthogonal Cartesian grids will be considered here for simplicity. Each grid can be filled with a homogeneous material, according to the geometrical and material details of the device under analysis. In this way the whole computational domain is composed of the finite set of elementary cells with volumes, V_n . The non-empty intersection of two elementary volumes is an area, non-empty intersection two elementary areas is a line and the intersections of two lines is a point. The state variables in FIT (the electromagnetic fields and fluxes) are generally allocated along the elementary lines or on the elementary areas.

Now let us consider a single cell with volume $V_{i,j,k}$ inside the computational domain as shown in Fig. 2.1. The electric voltage along one side of the surface $A_z(i, j, k)$ can be written as,

$$e_x(i, j, k) = \int_{x_i, y_i, z_i}^{x_{i+1}, y_i, z_i} \mathbf{E} \cdot d\mathbf{s}. \quad (2.5)$$

Here, x_i, y_i and z_i denote the coordinates of a cell node with indices i, j and k . In the same way, the voltages along the other edges can be computed to obtain the exact values of the integrals over the electric fields along these edges. The integral over a large area can be computed by summing up the integrals of the elementary areas constituting the larger one.

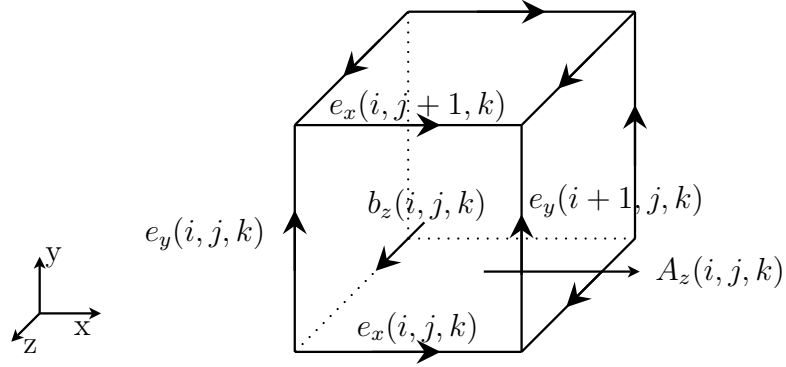


Figure 2.1: A single FIT cell with the allocation of electric grid voltages on the edges of an elementary area.

The total magnetic flux through the area $A_z(i, j, k)$ can be computed as the integral of the magnetic flux density over this area as,

$$b_z(i, j, k) = \int_{A_z(i, j, k)} \mathbf{B} \cdot d\mathbf{A}. \quad (2.6)$$

Total magnetic flux through a larger area can be computed as the sum over the magnetic fluxes of the constituting elementary areas. Now, the equations 2.5 and 2.6 can be used to reformulate the equation 2.1 for the elementary area $A_z(i, j, k)$ as,

$$e_x(i, j, k) + e_y(i+1, j, k) - e_x(i, j+1, k) - e_y(i, j, k) = -\frac{d}{dt} b_z(i, j, k). \quad (2.7)$$

Equation 2.7 is the integral formulation of Faraday's law for a single surface element of the elementary FIT cell. It may be noted here that equation 2.7 is the exact representation of the equation 2.1 as no approximation has been used.

The electric voltages and the magnetic fluxes over the whole cell complex are collected in an appropriate order and are arranged as a matrix equation of the form,

$$\begin{pmatrix} & & & & & & & \\ & & & & & & & \\ & & \dots & \dots & \dots & & & \\ 1 & \dots & 1 & \dots & -1 & \dots & -1 & \\ & & \dots & \dots & \dots & & & \end{pmatrix} \begin{pmatrix} e_{n1} \\ \vdots \\ e_{n2} \\ \vdots \\ e_{n3} \\ \vdots \\ e_{n4} \end{pmatrix} = -\frac{d}{dt} \begin{pmatrix} \vdots \\ b_n \\ \vdots \end{pmatrix}. \quad (2.8)$$

Here, the subscript n contains information about the cell index and the field components. The equation 2.8 can be written more compactly as,

$$[\mathbf{C}] \mathbf{e} = -\frac{d}{dt} \mathbf{b}. \quad (2.9)$$

2. The Finite Integration Technique

Here, the matrix $[\mathbf{C}]$ contains all the topological information about the electric fields according to their orientations on the cell edges within the grid G . So, the coefficients of $[\mathbf{C}]$ are only 1 and -1. The matrix $[\mathbf{C}]$ is so organized that it represents a discrete curl operator on the grid G . Further details about the arrangement of the matrix $[\mathbf{C}]$ can be found in [66]. The equation 2.9 represents the discrete form of the equation 2.1. Now

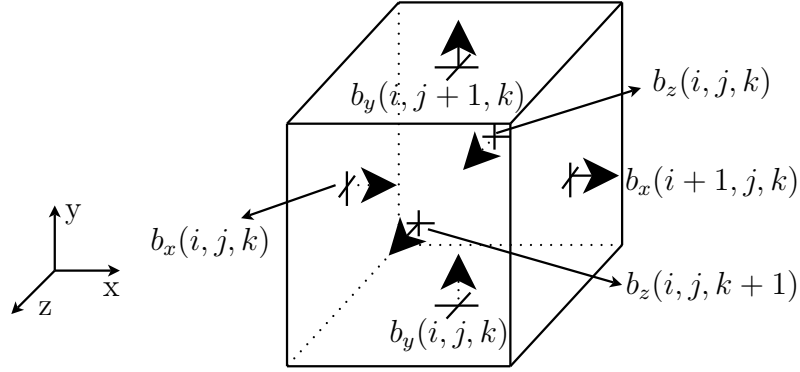


Figure 2.2: Allocation of the magnetic fluxes through the six surfaces of a FIT cell.

let us consider the equation 2.4, which describes the non-existence of magnetic charges. The total integral in this case can be expressed as the algebraic sum of the individual integrals over all the elementary areas constituting a FIT cell. The allocation of the magnetic flux vectors through the surfaces of a single FIT cell is shown in Fig. 2.2.1. So, the equation 2.4 can now be written as,

$$-b_x(i, j, k) + b_x(i+1, j, k) - b_y(i, j, k) + b_y(i, j+1, k) - b_z(i, j, k) + b_z(i, j, k+1) = 0 \quad (2.10)$$

Again, the above equation for a single cell can be extended to the whole computation domain and can be arranged as,

$$\begin{pmatrix} \dots & -1 & 1 & -1 & 1 & -1 & 1 & \dots \\ & & & \dots & \dots & & & \\ & & & & & & & \end{pmatrix} \begin{pmatrix} \vdots \\ b_{n1} \\ b_{n2} \\ b_{n3} \\ b_{n4} \\ b_{n5} \\ b_{n6} \\ \vdots \end{pmatrix} = 0. \quad (2.11)$$

The above equation can be written in a more compact form as,

$$[\mathbf{S}] \mathbf{b} = 0 \quad (2.12)$$

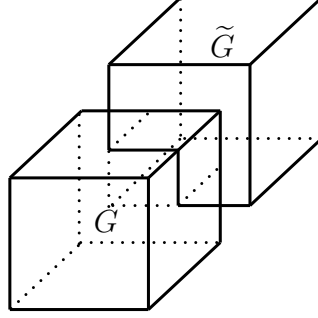


Figure 2.3: Geometrical orientation of the grid G and the dual-grid \tilde{G} in FIT.

The matrix $[\mathbf{S}]$ contains only the topology of the grid as in the case of the $[\mathbf{C}]$. The equation 2.12 is the discrete representation of the fourth Maxwell's equation.

Another grid system \tilde{G} is introduced in order to discretize the other two of Maxwell's equations. This is termed as the dual grid and there is a direct one-to-one correspondence between the grid G and the dual grid \tilde{G} . For the Cartesian system considered here, the dual grid is formed by taking the centers of the cells of G as the grid points of \tilde{G} . The spatial arrangements of the grids G and \tilde{G} are shown in Fig. 2.3.

The discretization of the second and third Maxwell's equations are accomplished in the similar way discussed for the two other equations. The magnetic voltages (h_i) are assigned as a state variable to each dual elementary line (\tilde{L}_i), the electric flux (d_i) and the total electric current (j_i) normal to the elementary dual grid surface (\tilde{A}_i) are assigned as state variables to each dual elementary area (\tilde{A}_i) whereas the discrete charges (q_i) are assigned as state variables to each elementary volume (\tilde{V}_i). So, the previously mentioned quantities can be expressed as,

$$h_i = \int_{\tilde{L}_i} \mathbf{H} \cdot d\mathbf{s} \quad (2.13)$$

$$d_i = \int_{\tilde{A}_i} \mathbf{D} \cdot d\mathbf{A} \quad (2.14)$$

$$j_i = \int_{\tilde{A}_i} \mathbf{J} \cdot d\mathbf{A} \quad (2.15)$$

$$q_i = \int_{\tilde{V}_i} \rho dV. \quad (2.16)$$

$$(2.17)$$

Storing the values of the state variables in column vectors (h, d, j and q) and the topological values in matrices ($\tilde{\mathbf{C}}$ and $\tilde{\mathbf{S}}$), the discrete form of equations 2.2 and 2.3 can be written as,

$$[\tilde{\mathbf{C}}] \mathbf{h} = \frac{d}{dt} \mathbf{d} + \mathbf{j} \quad (2.18)$$

2. The Finite Integration Technique

$$[\tilde{\mathbf{S}}] \mathbf{d} = \mathbf{q} \quad (2.19)$$

The voltages and fluxes allocated on the two different cell complexes G and \tilde{G} are to be related to each other according to the constitutive material relations. Since the voltages are allocated to the elementary cell edges and the fluxes are related to the elementary cell areas, an averaging of the material properties of the surrounding cells is required. One such allocation has been illustrated in Fig. 2.4. Here the electric voltage (e_n) is allocated along the elementary edge (L_n) of the elementary cell in G whereas the electric flux (D_n) is associated to the elementary area \tilde{A}_n within the dual grid \tilde{G} . Let the permittivities of the elementary cells 1, 2, 3 and 4 in G be denoted by ε_{n1} , ε_{n2} , ε_{n3} and ε_{n4} respectively, and their average by $\bar{\varepsilon}_n$. Then the relation between the electric field intensity and the flux density is written as,

$$D_n = \bar{\varepsilon}_n e_n \quad (2.20)$$

Proceeding in the similar way to couple the voltages and fluxes along with the corre-

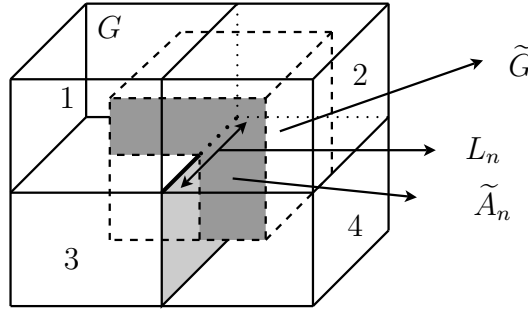


Figure 2.4: The elementary cell edge in G along which the electric voltages are allocated and the elementary cell area on \tilde{G} along which the electric fluxes are allocated.

sponding material relations over all the cells in the dual grid G and \tilde{G} , we obtain,

$$\mathbf{D} = [\mathbf{M}_\varepsilon] \mathbf{e} \quad (2.21)$$

$$\mathbf{B} = [\mathbf{M}_\mu] \mathbf{h} \quad (2.22)$$

$$\mathbf{J} = [\mathbf{M}_\sigma] \mathbf{e} + \mathbf{j}_s. \quad (2.23)$$

Here, $[\mathbf{M}_\varepsilon]$, $[\mathbf{M}_\mu]$, $[\mathbf{M}_\sigma]$ denote the permittivity, permeability and conductivity matrices and \mathbf{j}_s denote the impressed current.

The equations 2.9, 2.18, 2.19, 2.12 along with equations 2.21-2.21 are the discrete representation of the Maxwells equations used in the FIT formulation. These equations are generally termed as Maxwell's grid equations (MGEs).

The most important feature of the MGEs compared with other numerical methods for the solution of field problems is that the set of matrix equations is a consistent discrete representation of the original field problem. Moreover, the properties of the fields are maintained while transforming from the continuous case to the discrete one.

Due to this consistent formulation the numerical problems like the spurious modes or the parasitic charges does not appear in computations. Another aspect of this formulation is the possibility of cross checking the solutions at different stages during the computations. This is possible because they are vectors with exact algebraic properties.

As discussed earlier, the state variables are defined as the surface integrals or the line integrals over the elementary areas or elementary lines of the dual grid system G and \tilde{G} . These integrals involved in the computations are evaluated numerically using standard numerical integration schemes. This discretization is analogous to the discretization of the differential equations in case of the FDTD methods.

2.2.2 Maxwell's grid equations in time domain

For the time domain computations, a discretization of the time axis is also to be considered. The time derivatives involved in the Maxwells equation are approximated according to the central difference formula and the electric and magnetic field update equations are derived from those discretized equations. Using these update equations, the present electric and magnetic fields are obtained from the previous field values. Let

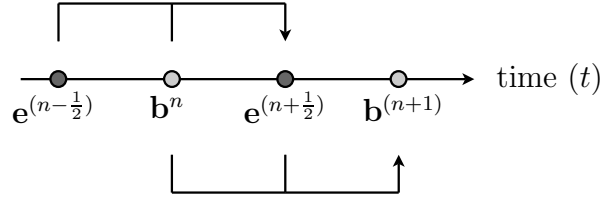


Figure 2.5: The time stepping scheme used for evaluating the fields in FIT ([69]).

us consider the step-size of time axes as Δt and the field values at n -th step be denoted by the superscript n . Using this notations, any function $f(t)$ in $t \geq 0$ is represented at the n -th time step as $f^n = f(t^n)$ with $t^n = n \Delta t$. Using this notation scheme, the update equations for the electric and magnetic fields from the equations 2.19 and 2.9 can be expressed as,

$$\mathbf{e}^{(n+\frac{1}{2})} = \mathbf{e}^{(n-\frac{1}{2})} + \Delta t [\mathbf{M}_\varepsilon]^{-1} \left[[\tilde{\mathbf{C}}][\mathbf{M}_\mu]^{-1} \mathbf{b}^{(n)} + \mathbf{j}_s^{(n)} \right] \quad (2.24)$$

$$\mathbf{b}^{(n+1)} = \mathbf{b}^{(n)} - \Delta t [\mathbf{C}] \mathbf{e}^{(n+\frac{1}{2})} \quad (2.25)$$

From the update equations, it can be noticed that the electric and magnetic fields are offset with respect to each other in time (half of the time step). The electric field at a particular instant is computed using the electric fields at one time step before, and the magnetic flux and the current source values half a time step before. This time stepping scheme is known as the leap-frog scheme and is also used in the FDTD method. The time stepping scheme is shown in the Fig. 2.5, where the horizontal axis denotes the time axes. The electric and magnetic fields are evaluated alternately at the time intervals marked as the circles along the time axis.

2. The Finite Integration Technique

2.2.3 Stability condition

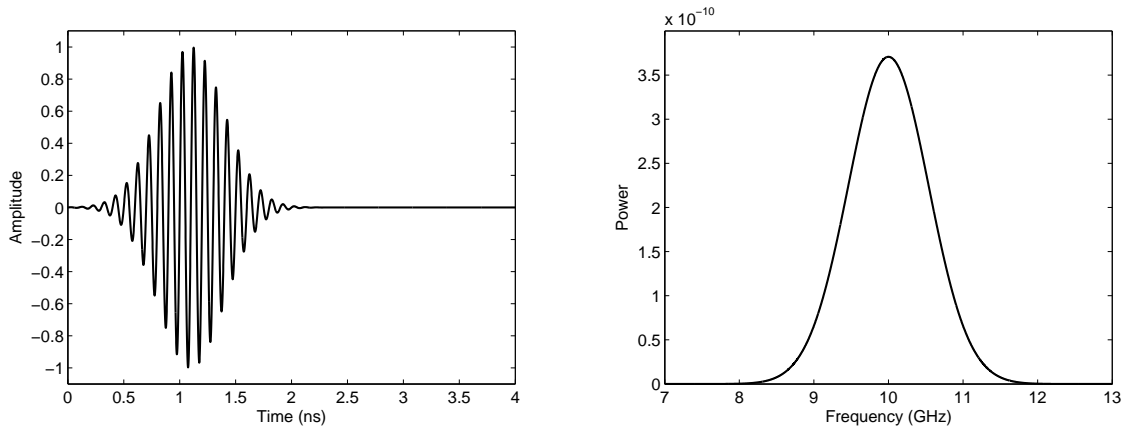
It can be shown that the coupled difference equations represented by the set of difference equations in 2.24 and 2.25 are conditionally stable. The stability criteria for this marching on time scheme is given by the well known Courant-Friedrichs-Levy condition [70]. For regular equidistant coordinate grids filled with homogeneous materials, this condition relates the largest time step Δt allowed with the smallest mesh steps in the three spatial directions as,

$$\Delta t \leq \frac{\sqrt{\mu\varepsilon}}{\sqrt{\left(\frac{1}{\Delta x}\right)^2 + \left(\frac{1}{\Delta y}\right)^2 + \left(\frac{1}{\Delta z}\right)^2}} \quad (2.26)$$

here, Δx , Δy and Δz are step sizes in the x, y and z direction respectively, whereas μ and ε denote the permittivity and permeability of the material in the cell. The stability condition in 2.26 basically enforces the causality condition by keeping the maximum allowed time step value equal to the time taken by electromagnetic waves to pass the smallest cell. It can be seen from 2.26 that in order to obtain a stable scheme for a problem with very fine mesh size, the allowed time step should be very small leading to a large simulation time.

2.2.4 Excitation

The excitation signal plays a very important role in obtaining the correct response of the system under analysis in the desired frequency range. Initially, the plane wave sources were used [26] for the time domain simulations. Since the real advantage of



(a) A modulated Gaussian pulse excitation signal in time domain. (b) Frequency spectrum of the excitation pulse.

Figure 2.6: A modulated Gaussian excitation pulse in time domain and its frequency domain spectrum.

the time domain formulations is to obtain the response of a system for a frequency range from a single run, it is advantageous to use pulsed excitations as functions of time. In order to characterize general microwave devices pulsed signal sources are used and specific field components at certain locations of the device under analysis are excited. The spatial characteristics of the excitation signal ensure propagation of the desired mode through the device whereas its temporal characteristic ensures obtaining the response of the device in the proper frequency band. The excitation waveform should include all the frequencies of interest and should have a smooth turn on and turn off in order to minimize any undesired high frequency components. Signals with Gaussian or modulated Gaussian temporal profile are most commonly used for excitations. These types of signals have well defined waveforms and Fourier spectrum. Fig. 2.6(a) shows a sine modulate Gaussian pulse in time domain suitable to obtain the response of a device in the frequency range from 8 to 12 GHz. The frequency spectrum of the same excitation pulse is shown in Fig. 2.6(b). The other source waveforms like the Blackman-Harris [71], derivative of Gaussian, Ricker and other wavelets [72] are also used as excitations sources.

2.2.5 Termination of the computation domain

As the computers have finite memory and computation capabilities, the physical problems to be solved are needed to be confined inside a finite computation domain. These is usually achieved by employing proper boundary conditions at the physical boundaries of the structure under analysis. However, for solving open problems using the fully numerical computational techniques like the FDTD, FEM, FIT etc. the computation domain is needed to be terminated artificially creating a free space surrounding the structure. Numerous methods have been proposed and are used for this purpose till date. The main purpose of these termination schemes is to totally absorb any electromagnetic field incident on it irrespective of the incidence angle, frequency etc. This effectively allows modeling of the free space, the efficiency and accuracy of which depends on the used scheme.

The mostly used truncation schemes can be categorized into two groups. The first group is differential equation based absorbing boundary conditions (ABC). These methods depend on providing the continuity of the propagating waves [73, 74] during the computations. ABCs in this category do not require addition of any further mesh layers but their performance is not so good as the other group. The second group relies on adding some totally absorbing material layers at the mesh boundaries. These layers are termed as perfectly matched layers (PML) [28]. The implementation of this type of mesh termination is a bit complicated and requires additional computational efforts due to the additional mesh layers to be added. Stability and related issues for the PML boundaries are still under investigations. However, usage of the PML boundaries have become more popular due to its superiority in performance over the differential equation based ABCs. A number of improvements have been reported in the literature in the recent days in the formulation of PML boundaries with the aim to simplify and improve

2. The Finite Integration Technique

their performances [75, 76].

2.3 Commercial CEM tools based on the FIT

2.3.1 Microwave Studio

CST Microwave Studio (MWST) is a Windows based user friendly electromagnetic simulation tool directly based on the FIT [37]. It is a subset of the general purpose electromagnetic software “CST Studio Suite” from Computer Simulation Technology [65]. This simulation tool provides a very good visual feedback at all stages of the simulation process, starting from modeling the geometry till post processing and visualization of the results. Advanced meshing schemes like the “partially filled cells”, “thin sheet technique” together with the features to integrate into various other windows based programs like MATLAB [61], AutoCAD [77], etc. have made it a powerful and convenient three dimensional electromagnetic simulation tool. However, there are several parameter settings mainly related to the PML settings, meshing, solver stability etc. physical implications of which are not fully transparent to the user. There solvers are available for the high frequency electromagnetic field problems. The available solvers are the transient, frequency domain and eigenmode solver.

Transient solver: This is the mostly used time domain solver of MWST. It can be used to obtain response of the structure under analysis in a specific frequency range with a single simulation. Different boundary conditions (open, conducting, periodic etc.), two dimensional port mode computations in the frequency domain, computations for lossless and lossy structures, simulation of frequency dependent material properties, far-field computations etc. are the main features of this solver. This solver is especially suited for the devices with open boundaries e.g. antenna and scattering problems.

Eigenmode solver: This solver allows to compute the eigenmodes and modal field distributions of closed loss free structures, e.g. resonators, filters etc. Periodic boundary conditions including phase shifts, calculations of losses and quality factors (perturbation method) etc. are among the main features of this solver.

Frequency domain solver: This solver is based on frequency domain formulation of the FIT and computes the frequency response of a given structure directly in the frequency domain. It is particularly suited for narrow-band analysis of electrically small problems. Some of the key features of this solver are, analysis of lossy and loss-free structures, different boundary conditions (open, conducting, periodic etc.), far-field computations etc.

The transient and the eigenmode solver have been extensively used for the simulations presented in this thesis.

2.3.2 MAFIA

MAFIA (solution of MAXwell’s equation by the Finite Integration Algorithm) [38] is a general purpose three-dimensional electromagnetic field simulator directly based on the

2.3 Commercial CEM tools based on the FIT

FIT formulation [38]. It is widely used for computer-aided design of three-dimensional RF cavities and other electromagnetic structures. The MAFIA program is organized in a modular manner, each module having their own specific functions. The modules includes preprocessor, post processor and solvers for different cases of Maxwells equations. All these modules can be run from a common Graphical Users Interface (GUI) as well as in batch modes or semi interactive modes using predefined command sequences. The organization of the modules available in the current MAFIA version (MAFIA 4.2) is shown in Fig.2.7. Short descriptions of the MAFIA modules and their main features are summarized in Table 2.1. For the simulations presented in this thesis, the MAFIA modules M, E, T3 and P have extensively been used. Here it may be noted that in contrast to Microwave Studio, some advanced meshing features like the partially filled cells are not included in MAFIA. Moreover, some restrictions regarding meshing and the geometries of the structures are to be respected for certain type of computations e.g. wakefield computations with MAFIA. Still, features like excitation through charged particle beam, the particle in cell codes together with the other relevant solvers within one software package make it a very cost effective CEM simulation tool.

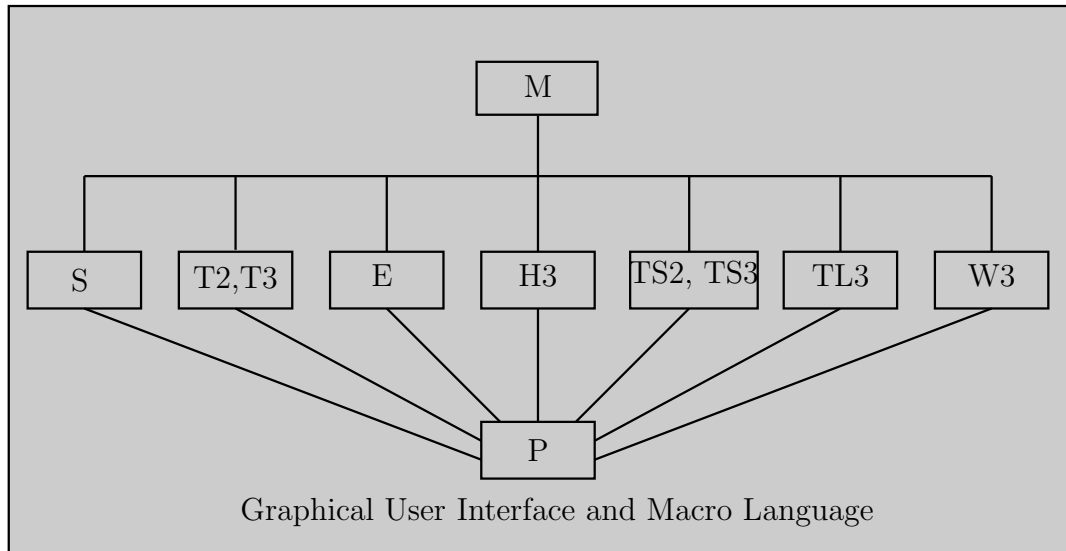


Figure 2.7: Schematic diagram of the organization of the MAFIA modules.

2. The Finite Integration Technique

Module	Description	Main features
M	Mesh generator, translates the geometry of the physical problem into mesh	Predefined shapes, import and export of CAD data, automatic mesh generation, fully parametric modeling etc.
S	Static solver, Electrostatic and Magnetostatic problems	Standard and open boundary conditions, electric currents and temperature distribution calculations, non-linear and anisotropic material properties etc.
T2, T3	Two and three dimensional time domain solvers	Broadband simulations, Absorbing boundary conditions, frequency dependent materials, calculation of particle beam wake fields, various excitations (incident plane waves, wave guide modes, superposed electric currents or voltages, particle beam) etc.
E	Eigenmode solver	Eigenmode computations (without spurious solutions), propagation parameters, accuracy determination, anisotropic materials, boundary conditions for symmetric and periodic structures etc.
H3	Thermodynamic solver	Computation of transient temperature distribution, coupled problems, external heat sources etc.
TS2, TS3	Two and three dimensional particle in cell solvers	Relativistic treatment of particle motion, electron /ion gun and tube simulations, boundary conditions (electric, magnetic, open) etc.
TL3	Low frequency time domain solver	Computation of transient low frequency fields, standard and open boundary conditions, current excitation etc.
W3	Frequency domain and Eddy current solver	Computation Eddy currents, various boundary conditions (Standard, open and waveguide), S-parameter calculations etc.
P	Post processor	Signal processing tools (DFT, FFT, AR-Filter), energy and loss computations, several post processing tools (integrals, curl, divergence etc. on the computed fields), touchstone export, different representation and visualization tools etc.

Table 2.1: Description and features of the MAFIA modules.

Chapter 3

Wake Computations and Related Analysis for PETRA III

3.1 Prologue

In this section applications of commercial CEM tools in the area of particle accelerators are reported. The computations and analysis are related to the components of the 3rd generation synchrotron light source PETRA III at DESY, which is currently under construction. The storage ring aims for a very high brilliance with a particle energy of 6 GeV and beam current of 100 mA. The main operating parameters of PETRA III are summarized in table 3.1. To achieve the aimed level of performance, it is of utmost importance to estimate the wakes, impedances and related parameters associated with various discontinuities mounted along its 2304 m long beam-pipe. In this section, the wakes, impedances and related studies for different parts of PETRA III have been presented. At first, wakes, impedances and related studies of the beam position monitors have been reported which is followed by the studies related to the longitudinal feedback cavity of PETRA III.

Parameters	Values	
Energy (GeV)	6	
Circumference (m)	2304	
RF Frequency (MHz)	500	
Total current (mA)	100	
Number of bunches	960	40
Bunch population (10^{10})	0.5	12
Bunch separation (ns)	8	192

Table 3.1: The main operating parameters of PETRA III.

3.2 Synchrotron radiation facilities

Charged particles radiate electromagnetic energy whenever they face an acceleration. In case of the charged particles moving at relativistic speeds, this radiation is confined to a narrow cone tangent to the particle trajectory [78]. The theoretical analysis of this radiation was first put forward by Liénard and further developed by Schott [79, 80]. This radiation is termed as synchrotron radiation and it depends on the energy of the charged particles and the amount of acceleration. A synchrotron radiation facility is a type of particle accelerator in which charged particles are accelerated to a high energy by an electric field while they are made to rotate along a circular path of constant radius by means of magnetic fields. During their orbit, these particles are forced to go through some predefined accelerations (usually achieved by magnetic fields) in order to make them radiate energy in the form of synchrotron radiation. The synchrotron radiations have some special properties like, high brightness, intensity and brilliance, high collimation (small angular divergence), low emittance, widely tunable in energy/wavelength, high level of polarization, pulsed light emission etc. These properties have made synchrotron radiation an important tool for applications in condensed matter physics, material science, biology and medicine. The synchrotron light sources are largely used to probe the structure of matter from the sub-nanometer level of electronic structure to the micrometer and millimeter level.

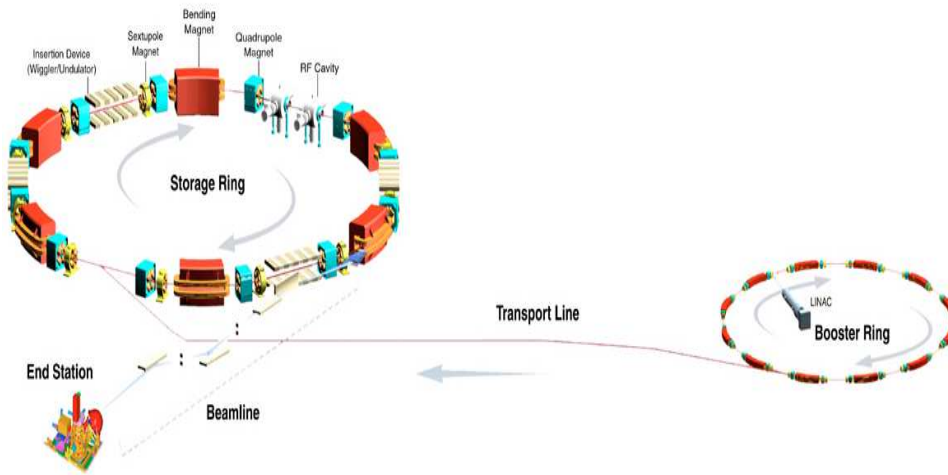


Figure 3.1: Schematic diagram of a synchrotron radiation facility [source: internet].

The largest part of a synchrotron radiation facility is a metallic beam pipe - inside which a high vacuum is maintained. The charged particles are made to travel inside the vacuum beam pipe by means of magnetic fields. The acceleration is usually accomplished in the radio-frequency cavities inserted along the beam pipe by applying suitable electric fields. Intense electric fields at the desired frequencies are provided by powerful amplifiers which are fed into those radio-frequency cavities. While the particles traverse through these cavities, some of the energy of the radio wave is transferred to them and

the particles are accelerated.

Usually, dipole magnets are used to bent the path of the particle beam. Focussing of the particle beam is achieved by quadrupole magnets or an array of quadrupole magnets, wherever necessary. Hundreds of sensors and associated electronics are installed along the beam pipe in order to monitor the position of the beam. A large number of corrector devices are used to prevent any unwanted deviation, instabilities or oscillations of the beam. Beside these, many insertion and pumping devices, safety arrangements etc. are also employed with such a facility to ensure its proper functioning. In Fig. 3.1 the schematic diagram of a synchrotron radiation facility is presented, indicating the major parts.

3.3 Theoretical basics

3.3.1 Wakefields and impedances

In a particle accelerator, the charged particle beams usually travel inside a conducting pipe (beam pipe) maintained at high vacuum. For a particle accelerator in reality, the beam encounters different cross sections of the beam pipe and interacts with the discontinuities. The interactions of the beam with its surrounding are described in detail by wakefields [81, 82]. From these fields several quantities, including the loss and kick parameters, can be calculated. The various loss and kick parameters obtained in this way represent integral measures of the interaction of the beam with the considered part of the accelerator. In order to ensure proper functioning and achieve the design goals it is therefore required to know the wakefields of different parts of the accelerator.

Let us consider a point charge moving in free space at a velocity close to the velocity of light, c . With reference to the laboratory frame, the electric and magnetic fields of such a relativistic particle lie nearly in a plane passing through the charge and perpendicular to its path. So, a second charge moving behind the first charge on the same or on a parallel path, and at the same velocity $v \approx c$ will not be subjected to any forces from the fields produced by the leading charge. The situation is different if the two charges are moving in the vicinity of metallic objects or other boundary discontinuities. The trailing charge still does not experience the direct fields in the wavefront moving with the leading charge. This wavefront can, however, scatter from the boundary discontinuities, and this scattered radiation is able to reach the trailing charge and exert forces parallel and perpendicular to its direction of motion. These scattered waves are termed wakefields, and the integrated effects of these wakefields over a given path length of the trailing charge give rise to longitudinal and transverse wake potentials [83, 84].

Let us consider the situation shown in Fig. 3.2. Here, a test charge q_2 is following a point charge q_1 along a discontinuity in the beam pipe. Let \mathbf{E} and \mathbf{B} be the electric and magnetic field excited by the point charge q_1 at the longitudinal position $z = ct$. Both the charges have the same radial offset \mathbf{r} from the axis and the test charge q_2 is

3. Wake Computations and Related Analysis for PETRA III

at a distant s from q_1 . The Lorentz force on the test charge with momentum \mathbf{p} due to the fields generated by the point charge q_1 is

$$\mathbf{F} = \frac{d\mathbf{p}}{dt} = q_2 (\mathbf{E} + c \mathbf{e}_z \times \mathbf{B}) \quad (3.1)$$

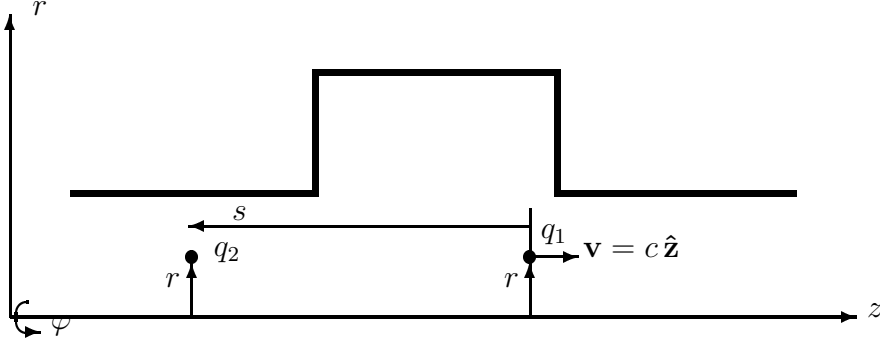


Figure 3.2: A point charge q_1 traversing a cavity with an offset r followed by a test charge q_2 with the same offset.

In this case, the wake potential due to the point charge q_1 can be defined as:

$$\mathbf{W}^\delta(r, s) = \frac{1}{q_1} \int_{-\infty}^{+\infty} dz (\mathbf{E} + c \mathbf{e}_z \times \mathbf{B})_{t=(z+s)/c} \quad (3.2)$$

The wake potential may be regarded as an average of the Lorentz force on a test charge. Causality requires $\mathbf{W}(s) = 0$ for $s < 0$. The distant s is positive in the direction opposite to the motion of the point charge q_1 . The wake potential of a Gaussian bunch with charge density:

$$\rho(\mathbf{r}, t) = q_1 \lambda(z - ct), \quad \lambda(s) = \frac{1}{\sigma\sqrt{2\pi}} \exp\left(-\frac{(s - s_0)^2}{2\sigma^2}\right)$$

is obtained by a convolution integral with the point charge wake potential \mathbf{W}^δ

$$\mathbf{W}(r, s) = \int_0^\infty ds' \lambda(s - s') \mathbf{W}^\delta(r, s') \quad (3.3)$$

From the wake potential $\mathbf{W}(s)$ of a Gaussian bunch the following loss and kick parameters are obtained:

$$k_{\parallel} = \int_{-\infty}^{\infty} ds W_{\parallel}(r = 0, s) \lambda(s) \quad (3.4)$$

$$k_{\parallel}(1) = \int_{-\infty}^{\infty} ds W_{\parallel}(r = 0, s) \frac{d}{ds} \lambda(s) \quad (3.5)$$

$$k_{\perp} = \frac{1}{r} \int_{-\infty}^{\infty} ds W_{\perp}(r, s) \lambda(s). \quad (3.6)$$

The parameter (k_{\parallel}) is termed as the total loss parameter and it is a cumulative representation of the all the losses (i.e losses due to the excited cavity modes and beam pipe modes). If the total charge of the Gaussian bunch is q_1 , the total energy loss of the bunch [85, 86] is given by,

$$\Delta W = q_1^2 k_{\parallel}. \quad (3.7)$$

The parameter $k_{\parallel}(1)$ is a crucial parameter for the longitudinal impedance model of an accelerator [87]. From the parameter $k_{\parallel}(1)$ and the kick parameter k_{\perp} the coherent tune shifts of the lowest order bunch modes in the longitudinal ($\Delta\nu_s$) and transverse planes ($\Delta\nu_{\beta}$) can be calculated according to the following equations [88, 87]:

$$\Delta\nu_s = \nu_s \frac{I_B R T_0}{2 h U_{\text{rf}}} k_{\parallel}(1) \quad (3.8)$$

$$\Delta\nu_{\beta} = \frac{I_B \langle \beta \rangle T_0}{4\pi E/e} k_{\perp}, \quad (3.9)$$

where ν_s is the synchrotron tune, I_B the single bunch current, R the average radius, T_0 the revolution time, h the harmonic number, U_{rf} the total RF voltage, $\langle \beta \rangle$ the average beta-function and E the energy of the accelerator.

The frequency domain description for the coupling between the beam and its environment can be obtained with the Fourier transform of the wake potential. The Fourier transform of the longitudinal wake potential is called the longitudinal impedance or the longitudinal coupling impedance

$$Z_{\parallel}(x, y, \omega) = \frac{1}{c} \int_{-\infty}^{\infty} W_{\parallel}(x, y, s) e^{-\frac{j\omega s}{c}} ds \quad (3.10)$$

Similarly, the transverse impedance or is defined as,

$$Z_{\perp}(x, y, \omega) = \frac{-j}{c} \int_{-\infty}^{\infty} W_{\perp}(x, y, s) e^{-\frac{j\omega s}{c}} ds \quad (3.11)$$

The impedance spectra corresponding to a discontinuity along the beam pipe contains a number of peaks. The sharp impedance peaks below the cut-off frequency of the fundamental mode of the beam pipe correspond to the resonant modes of the discontinuity under consideration. Above the cut-off frequency of the beam pipe, a continuous spectrum corresponding to the beam pipe modes are usually seen. Although the impedances and wake potential are the description of the same quantity connected by an integral transform, they are usually used to represent complementary information. The impedance representation is more appropriate for the long range phenomena, while the wake potential representation is appropriate in case of short distances.

3.3.2 Relationships between resonant cavity parameters and the beam

The electromagnetic field induced by a charged particle or particle beam at any discontinuity along the beam pipe can be represented by an infinite sum of the resonant modes

3. Wake Computations and Related Analysis for PETRA III

corresponding to the discontinuity. The resonant frequencies of these modes will depend on the geometrical details of the discontinuity. Each of the modes can be considered as a parallel LC circuit and can be characterized by their resonant frequencies, quality factors etc. In order to represent the interactions between the beam and the discontinuity, a charged particle traversing a simple pill-box cavity can again be considered. Let us consider the charged particle is traversing the cavity along the z axis, as shown in Fig. 3.2. The instantaneous electric field at a radial distance r can be represented as

$$\mathbf{E}(r, t) = \text{Re} \left\{ \sum_{n=0}^{\infty} \mathbf{E}_n(r) e^{j\omega_n t} \right\} \quad (3.12)$$

where $\omega_n = 2\pi f_n$ is the angular frequency of a mode with resonant frequency f_n .

For each resonant mode, a voltage (V_n) at a transverse distance r can be computed as the integral of the electric field along z as,

$$V_n(r) = \int_{-\infty}^{\infty} E_{z,n}(r, z) \exp(j\omega z/c) dz \quad (3.13)$$

For practical computations, the integration is evaluated over the length L of the cavity in the longitudinal direction. This voltage is experienced by the point charge traveling with the light velocity c due to the considered mode. The total energy stored in the mode, considering the time averaging factor can be computed as

$$U = \frac{\epsilon_0}{4} \int |\mathbf{E}|^2 d^3r. \quad (3.14)$$

Here, it may be noted that for numerical computation of total energy of a mode with MAFIA, the symmetries should be considered carefully.

The loss parameter (k) corresponding to a resonant mode is defined as,

$$k = \frac{|V|^2}{4U} \quad (3.15)$$

As the voltage V is dependent on the radial offset r (equation 3.13), the loss parameter is also a function of it. The longitudinal wake potential behind the point charge (for $s > 0$) can be expressed using the loss parameters as [81],

$$W_{\parallel}^{\delta}(r, s) = \sum_{n=0}^{\infty} 2k_n(r) \cos(\omega_n s/c) \quad (3.16)$$

The quality factor, which is also termed as Q-factor or Q-value is an important parameter representing the sharpness of the resonance under consideration. A resonant mode with higher quality factor resonates for a long time while that with a lower quality factor will resonate for a shorter time. The quality factor of a resonant mode with an

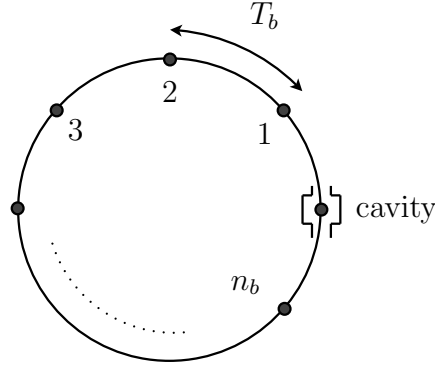


Figure 3.3: A circular accelerator with a discontinuity (cavity) traversed by n_b bunches.

angular frequency ω is defined as,

$$\begin{aligned} Q &= \omega \frac{\text{Time averaged stored energy}}{\text{Time averaged power loss}} \\ &= \frac{\omega U}{P_w} \end{aligned} \quad (3.17)$$

where P_w is the dissipated power corresponding to the considered resonant mode. Usually the quality factor is computed by perturbation method, in the post processing stage after eigenmode computations.

The induced voltage left behind a point charge with total amount of charge q traveling with light speed c in a cavity mode can be expressed as a function of the bunch coordinate as,

$$V(s) = 2kq \cos\left(\omega \frac{s}{c}\right) \exp\left(-\frac{\omega}{2Q} \frac{s}{c}\right) \quad (3.18)$$

where k and Q are the loss parameter and quality factor corresponding to the considered mode. Now let us consider a circular accelerator with one discontinuity (considered as a cavity) and n_b number of identical bunches traveling with a temporal distance T_b with each other (Fig.3.3). The induced voltage in one cavity mode after n_b number of bunches have traversed the cavity is given by,

$$V(n_b) = \sum_{i=1}^{n_b} 2kq \cos(\omega i T_b) \exp\left(-\frac{i T_b \omega}{2Q}\right) \quad (3.19)$$

In the case of all the bunches arriving at the cavity in phase with the cavity mode (the worst case) and the number of bunches traversing the cavity is very large ($n_b \rightarrow \infty$), the induced voltage ($V(\infty)$) can be obtained as,

$$V(\infty) \propto \frac{kQ}{\omega} \frac{q}{T_b} \quad (3.20)$$

$$= R_{shunt} I \quad (3.21)$$

3. Wake Computations and Related Analysis for PETRA III

Here R_{shunt} is termed as the shunt impedance and is widely used to represent the coupling between the beam and the cavity. It is generally defined as

$$R_{shunt} = \frac{2kQ}{\omega} \quad (3.22)$$

Sometimes the factor 4 is used (US definition) in stead of 2. For the computations in this thesis, equation 3.22 has been used.

The shunt impedance can also be represented in terms of the cavity voltage (equation 3.13) and dissipated power as

$$R_{shunt}(r) = \frac{|V(r)|^2}{2P_w} \quad (3.23)$$

The parameter G_1 is defined as the product of the quality factor of the mode and the surface resistance of the cavity wall [89]. The G_1 parameter can be calculated in case of a copper cavity according to the equation:

$$G_1 = R_{cu} Q, \quad (3.24)$$

where R_{cu} is the surface resistivity of copper.

3.4 Wake computation procedure

3.4.1 Using MAFIA for wakefield computations

The wakes and impedances can be calculated analytically only for a very few and simplified structures like an uniform cylindrical beam pipe with closed pill-box cavities. Semi analytical methods using point matching technique has also been reported in the literature for this purpose [90]. For the realistic accelerator components with complicated geometries, the only possible way for wake computations is to rely on numerical methods. A direct approach and an indirect approach can be used for the wake computations. The direct method for computing wakes from the electromagnetic fields is strongly affected by numerical noise. Whereas one can achieve better accuracies using the indirect method for wake computations for the particle bunches moving with the velocity of light [91]. The indirect method of wake computation have been used for all our computations.

In the indirect method, an imaginary cylinder (not necessarily circular) enclosing the beam is considered. The axis of the cylinder is considered to be axis parallel to the beam axis. The cross section of the cylinder is defined by the two transverse planes (at two ends of the computation domain transverse to the beam direction). At first, the characteristic wake function is computed evaluating the wake integral along the boundaries of the imaginary cylinder. The longitudinal component of the electric field vanishes at the metallic boundaries of the beam-pipe. Therefore the only contribution to the wake integral is due to any discontinuity or gap adjacent to the beam pipe. Using

the characteristic wake function as the expansion coefficients of a multipole expansion satisfying the Poisson's equation and related boundary conditions, it is possible to obtain the longitudinal wakes for a certain radial position [81]. Once the longitudinal wake is calculated, the transverse wakefields can be calculated applying the Panofsky-Wenzel theorem [92].

In the first step for wake computations, the structure is modeled using the mesh generator module of MAFIA. Afterwards the eigenmode solver module is used to compute the eigenmodes for the waveguide ports associated with the considered device. These modes are then loaded in the MAFIA time domain module for proper termination of the ports. In the next step, the properties of the particle beam are specified (the beam width, total charge of the beam, orientation of the beam etc.). In the time domain solver the charged particle beam with the specified properties is then used as the excitation source. The solver is then started for an appropriate time range. The minimum time range is usually taken as the time the beam takes to pass through the whole structure. The maximum time range depends on the frequency resolution required for the impedance computation. Once the computations are finished, the results are exported and further processed with MATLAB for extracting different loss parameters and kick parameters.

Here it may be mentioned that a new coordinate system is generally used to describe the positions of the particles in the bunch. This coordinate system is termed the "bunch coordinate system". This bunch coordinate system is specified by the two transverse Cartesian coordinates which are the same as before and a new coordinate axis "s" along the beam axis. The orientation of this s-axis is opposite to the direction in which the beam moves. The origin of the bunch coordinate system is moving with the bunch and is given by the position of the very first particle in the bunch.

3.4.2 Wake computations for large structures with off-axis beam

Computing wakefields for an off-axis beam usually requires at least double memory than computing those for an on axis beam. This is because although the structure is geometrically symmetric, it becomes asymmetric with respect to the exciting beam. In many instances the available memory is still the limiting factor for the time domain wakefield computations. This problem is more severe in case of large structures, containing small geometrical features. In these cases, it would be very useful if only a part (say one quarter or one half) of the geometry is modeled and the wake computation results of some combinations of different boundary conditions are obtained. Afterwards the results could be combined to get the response of the whole structure. In this way, the memory requirement is halved at the cost of computational time.

To test the validity and accuracy of this method, off-axis wake computations for very simple and small structures can be considered. At the first step two sets of wakefield computations could be done considering an off-axis beam (y-offset) and one quarter of the structure. The boundary conditions for the wake computations for the quarter geometry is tabulated in Table 3.2. Then the results are combined to obtain the actual

3. Wake Computations and Related Analysis for PETRA III

wakes for the beam with y-offset. It can be noted here that for the first set of the boundary conditions, we can consider the computed wakefields W_{gew} generated by the 1dcurrent (I) and its image current (-I) (as an electric wall has been used at the y-min boundary). Similarly, for the second set of boundary conditions (magnetic wall at the y-min boundary), the computed wakefields (W_{qmw}) were due to (I) and its image current (I). As the wakefield computations involve only linear operations, the results corresponding the excitation (I) should be simply given by $\frac{W_{gew}+W_{qmw}}{2}$. In the next step, the off axes wakes are computed directly for half of the structure with the boundary conditions shown in Table 3.3. The x-min boundary in this case is $x=0$ plane, whereas the beam pipe wall is located at the x-max boundary. The errors in computed wakes between both the methods should be very small. Fig. 3.4 shows the schematic diagrams for the wake computations considering one half and one quarter of the geometry.

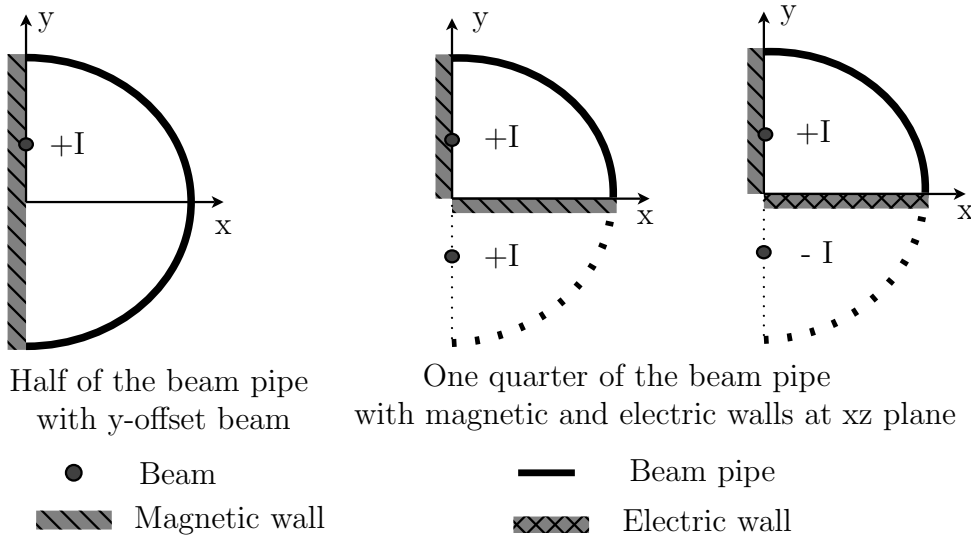


Figure 3.4: Schematic diagram depicting the excitations and boundary conditions for off-axis wake computations considering one half and one quarter of the beam pipe.

Two simple test geometries have been considered to demonstrate the suggested method. The first geometry is a simple pill-box cavity along the beam pipe, while the other geometry contains cylindrical holes in the upper part and lower parts of the

Boundaries	Boundary conditions
x-min, x-max	Magnetic (Magnetic), Electric (Electric)
y-min, y-max	Electric (Magnetic), Electric (Electric)
z-min, z-max	Waveguide(Waveguide), Waveguide (Waveguide)

Table 3.2: Boundary conditions used in MAFIA for the time domain wakefield computations for one quarter of the test structure.

3.4 Wake computation procedure

Boundaries	Boundary conditions
x-min, x-max	Magnetic, Electric
y-min, y-max	Electric, Electric
z-min, z-max	Waveguide, Waveguide

Table 3.3: Boundary conditions used in MAFIA for the time domain wakefield computations for half of the test structure.

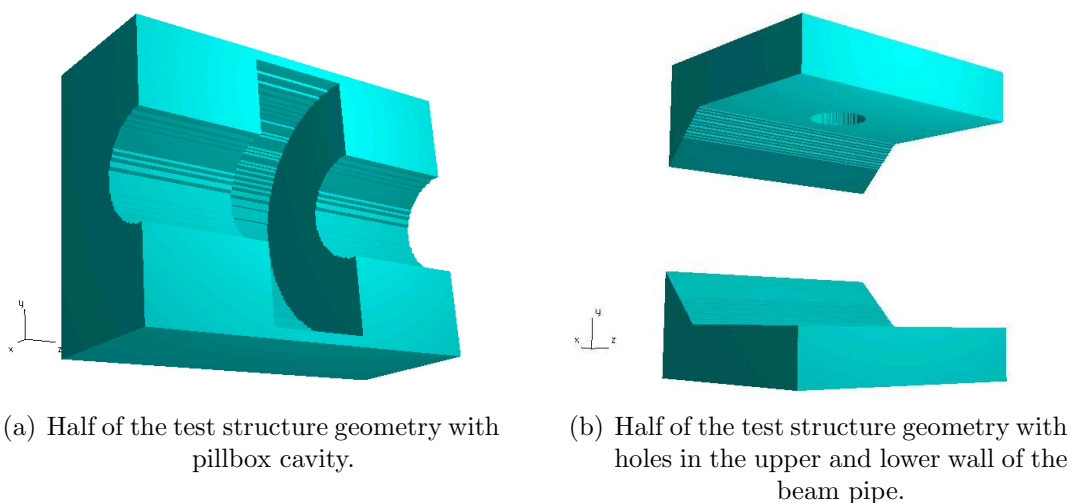


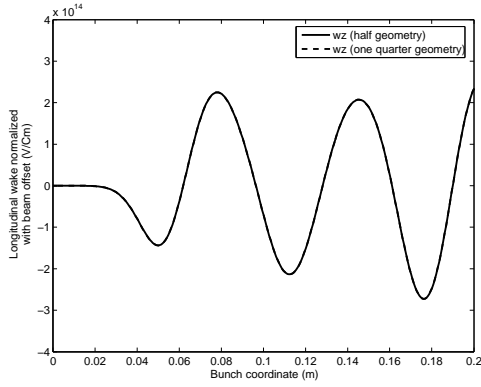
Figure 3.5: One half of the geometries considered as the test structures.

beam pipe. The first test structure can be considered as representative of the cases where a cavity is inserted along the beam pipe (i.e. the RF cavities, kickers etc.). The other structure is representative of the situations where small discontinuities are present in the beam pipe (BPMs, small transitions etc.). The MAFIA models of both the test geometries are shown in Fig. 3.5. The hole in the upper part of the beam pipe can be seen in Fig. 3.5(b), while that in the lower part of the beam pipe is not visible.

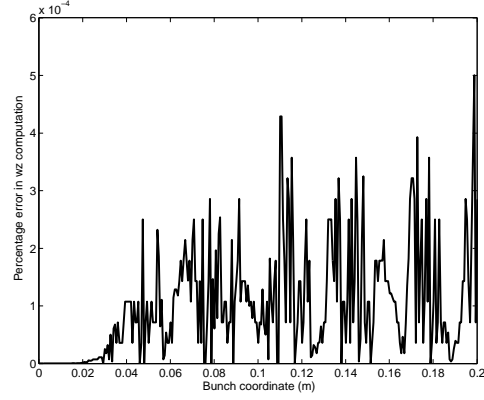
The comparison between the computed longitudinal wakefields for the test structure are shown in Fig. 3.6(a). Once the longitudinal wake was computed using one quarter of the first test structure (combining results of two different boundary conditions) and once it was computed directly using half structure. The absolute percentage error normalized to the maximum is shown in Fig. 3.6(b). Fig. 3.7 shows the comparison of the transverse wake and the corresponding absolute percentage error (normalized to maximum).

The wake computation results for the second structure are shown in Figs. 3.8 and 3.9. The absolute percentage errors normalized to the corresponding maximum values are also shown. From the figures it is clear that in this case the percentage error in transverse wake computation is much higher than that of the longitudinal component. The relative error in percent is less than 1% in case of longitudinal wake computation whereas it is less than 10% in case of transverse wake computation. One possible reason

3. Wake Computations and Related Analysis for PETRA III

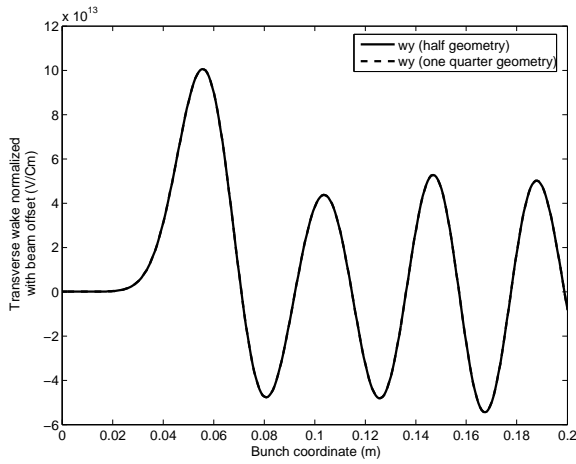


(a) Comparison between the longitudinal component of wake computed considering one half and one quarter of the first test geometry.

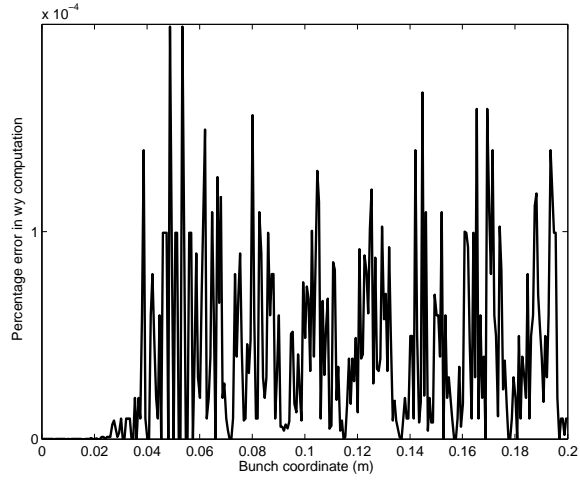


(b) Absolute percentage error (normalized to maximum) in longitudinal wake computation.

Figure 3.6: Comparison of computed longitudinal wake for the first test geometry and absolute percentage error.



(a) Comparison between the transverse component of wake computed considering one half and one quarter of the first test geometry.

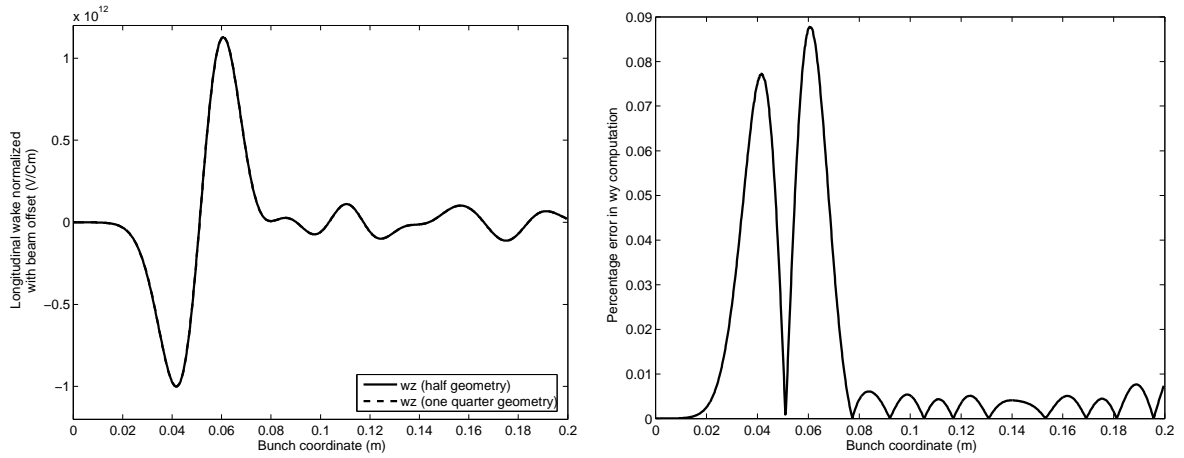


(b) Absolute percentage error (normalized to maximum) in transverse wake computation.

Figure 3.7: Comparison of computed transverse wake for the first test geometry and absolute percentage error.

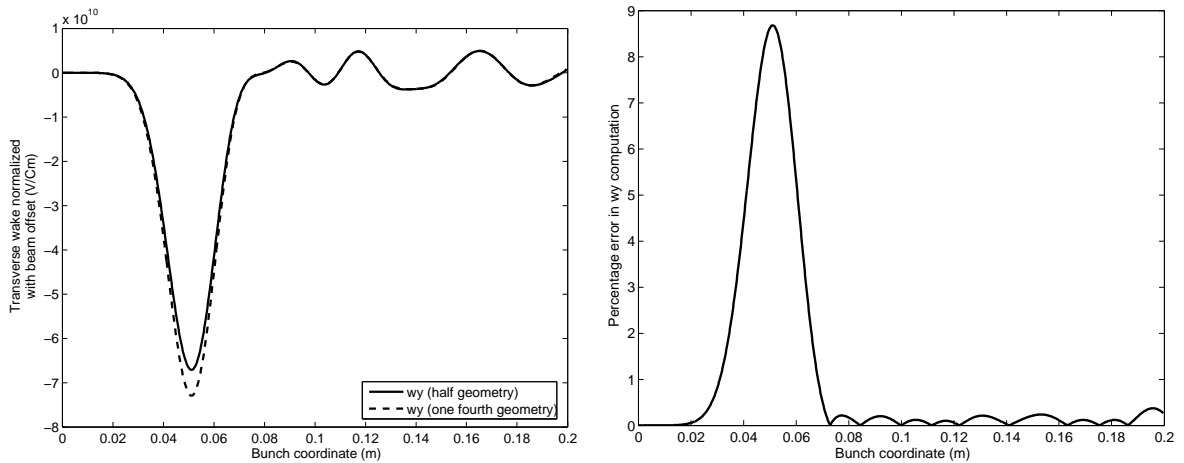
for this may be the difference in computing the transverse wakes considering one half of a structure and one quarter of the same structure. This problem has been pointed out in section 3.5.4, where a comparison between the output signals at the two coaxial ports with a on-axis beam is shown. This error is probably a numerical error originated from the difference in the sequences to numerically evaluate the curls of the fields [93, 94].

3.4 Wake computation procedure



(a) Comparison between the longitudinal component of wake computed considering one half and one quarter of the second test geometry. (b) Absolute percentage error (normalized to maximum) in longitudinal wake computation.

Figure 3.8: Comparison of computed transverse wake for the second test geometry and absolute percentage error.



(a) Comparison between the transverse component of wake computed considering half of the geometry and quarter of the geometry. (b) Absolute percentage error (normalized to maximum) in transverse wake computation.

Figure 3.9: Comparison of computed transverse wake for the second test geometry and absolute percentage error.

3.5 Simulation results for PETRA III beam position monitors

3.5.1 Beam Position Monitor

During the operation of any particle accelerator, an inevitable and very important task is to monitor the beam precisely. This task is accomplished by the beam position monitor (BPM) systems. The BPM system usually consists of a pick-up station, signal detection and processing unit and the display (or other appropriate devices). The pick-up stations consist of several transducers or pick-up devices which are directly attached to the beam-pipe. They pick up signals proportional to the beam offset and transmit it to the signal detection and processing unit. Several types of pick-up devices can be used for beam monitoring, depending upon their signal pick-up mechanisms. Some examples of the pick-up devices are, the cylindrical pillbox BPMs, the button type BPMs, stripline BPMS, the reentrant cavity type BPMs etc.

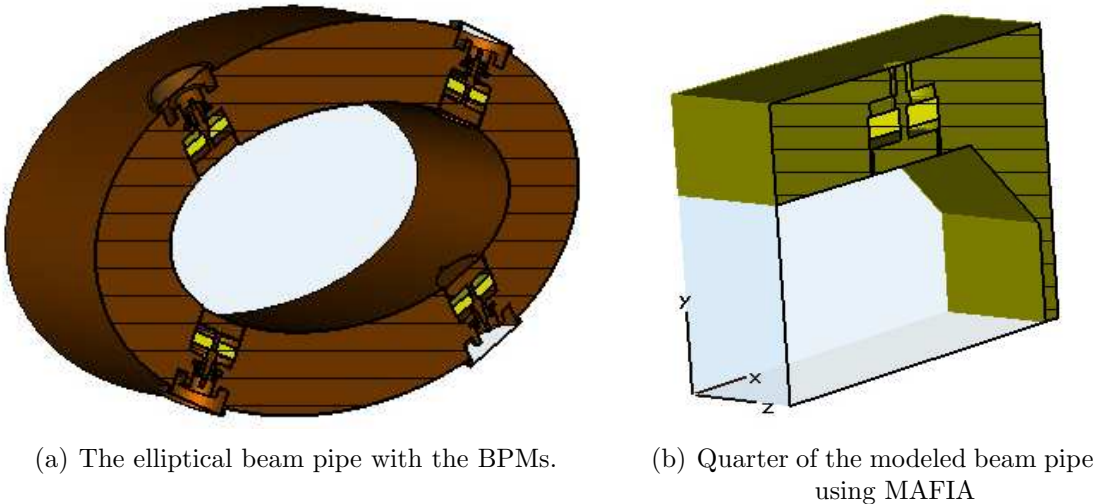


Figure 3.10: The elliptical beam pipe and the same beam pipe as modeled for the MAFIA simulations.

In PETRA III, more than 200 BPMs are foreseen to monitor the beam along its 2304 m circumference [88]. Although the stripline or resonant cavity BPMs have a potential for higher sensitivity and resolution, their practical implementation in a large scale BPM system is very complicated and expensive. So, it is planned to employ the button type BPMs in PETRA III, like most of the third generation light sources do.

In the button type of monitors, usually four button pick-ups are attached to the beam pipe. They pick up the beam induced voltages on these four buttons while the beam pass through the pick-up station. From these four signals the positions of the beam is determined with precision in the micrometer range. There is a small gap between the pick-up button and the beam pipe wall, which can cause wakefields in the vicinity of the

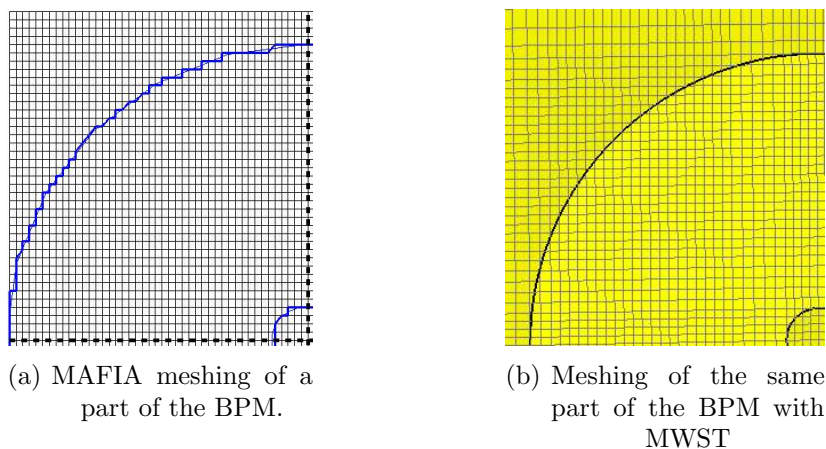


Figure 3.11: MAFIA and MWST meshing of some parts of the BPM

BPM. As the total number of BPMs to be used is large, their cumulative impedance can significantly contribute to the overall impedance of the machine. Moreover the presence of any trapped modes in the vicinity of the BPM button can significantly influence the performance of the system.

A beam pipe with the BPM buttons positioned at an angle of 45° with respect to the vertical axis is considered for analysis. The cross section of the elliptical beam pipe along with the BPMs is shown in Fig. 3.10(a). This design is not optimal for the measurement of the beam position in the vertical plane and a modified design will be installed in PETRA III. The semi major axis and the semi minor axis of the normal beam pipe are 40 mm and 20 mm respectively. Due to limitations for the shape creation and computer memory the elliptical structure was modeled in MAFIA as an octagon. One quarter of the beam pipe and the relevant coordinates as modeled in MAFIA are shown in Fig. 3.10(b).

The auto-mesh facility within MWST was used to model the beam pipe with the BPM, while the MAFIA mesh was created manually. A comparison of the MAFIA and MWST meshes is shown in Fig. 3.11. It can be noticed that MWST allows partially filled meshes, whereas MAFIA supports only diagonal meshes. So the MWST model is more realistic than the MAFIA model. This difference is prominent for the BPM, as they consist of many small cylindrical shapes.

3.5.2 Eigenmode computation results for BPMs in the normal beam pipe

To investigate the existence of any trapped modes near the BPM buttons, the eigenmode solvers have been used. A 25 mm long beam pipe section has been used with the BPM mounted at the middle of the structure. The lower boundaries at x and y directions have been taken as magnetic ones. This has been done to be consistent with the situation of a charged particle beam traveling axially through the structure. To compute the

3. Wake Computations and Related Analysis for PETRA III

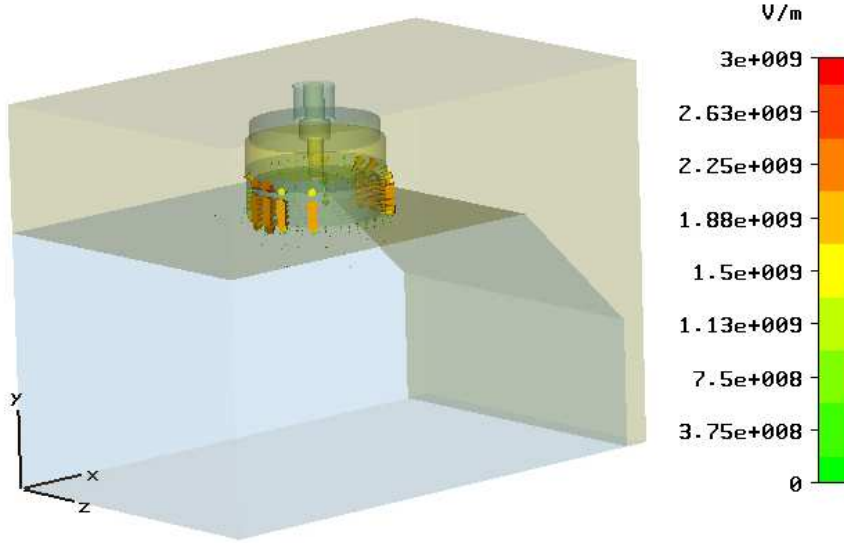


Figure 3.12: The electric field distribution corresponding to the first mode as calculated with MWST.

resonant modes corresponding to the BPM discontinuity, the boundary conditions at z boundaries have been changed, keeping the other boundary conditions fixed. The boundary conditions used for the eigenmode computations are summarized in Table 3.4. To have a cross check, the eigenmodes have been computed with eigenmode solvers of both MAFIA and MWST.

The resonant frequencies of the first ten modes using the eigenmode solvers of MAFIA and MWST are summarized in Table 3.5. From the eigenmode solver results it may be noted that the eigenfrequencies for the 1st, 6th and 7th eigenmodes do not change with the alternation of the boundary condition in the z -direction. The reason for this is that these three modes are concentrated near the BPM-button and therefore do not interact with the boundaries at z -min and z -max. This is further supported by the electric field plots for these modes as shown in the Figs. 3.12, 3.13, 3.14. The field plots clearly show that the energy of these modes is closely bound to the BPM itself.

The electric field plots corresponding to the modes 1, 6 and 7 computed with MAFIA are shown in Figs. 3.15, 3.16 and 3.17, respectively. The two-dimensional plots of the

Boundaries	Boundary conditions
x-min, x-max	Magnetic, Electric
y-min, y-max	Magnetic, Electric
z-min, z-max	Electric (Magnetic), Electric (Magnetic)

Table 3.4: Boundary conditions used in MWST and MAFIA for the eigenmode computations with respect to the coordinate axes shown in Fig. 3.10

3.5 Simulation results for PETRA III beam position monitors

Mode Number	Resonant frequencies (GHz)			
	Electric wall at z-boundaries		Magnetic wall at z-boundaries	
	MAFIA	MWST	MAFIA	MWST
1	1.8624	1.9271	1.8875	1.9282
2	4.2187	4.2094	4.5767	4.5786
3	6.8872	6.8785	7.2772	7.2862
4	7.3403	7.3286	7.4327	7.4405
5	7.5065	7.5058	7.5491	7.5533
6	8.6694	9.0355	8.6706	8.9127
7	8.6925	9.0381	8.7013	9.0225
8	9.1404	9.1301	9.1890	9.2485
9	9.5834	9.5967	9.5877	9.6157
10	10.2285	10.2229	10.2340	10.1939

Table 3.5: Resonant frequencies computed with MAFIA and MWST with the set of boundary conditions shown in Table 3.4

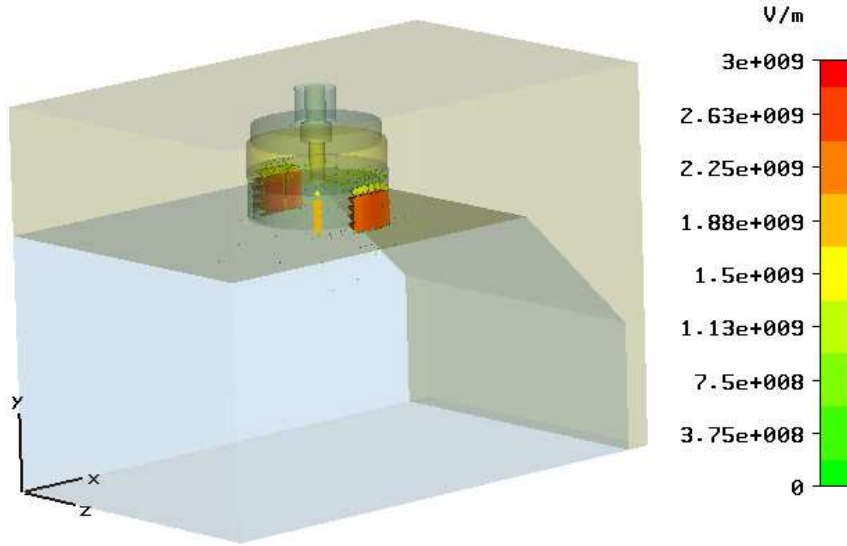


Figure 3.13: The electric field distribution corresponding to the sixth mode as calculated with MWST.

electric field distribution in the vicinity of the BPM-button are also shown in the figures. The field distributions for the 6th and 7th modes indicate that these two modes are nearly degenerate orthogonally polarized dipole modes trapped in the vicinity of the BPM button.

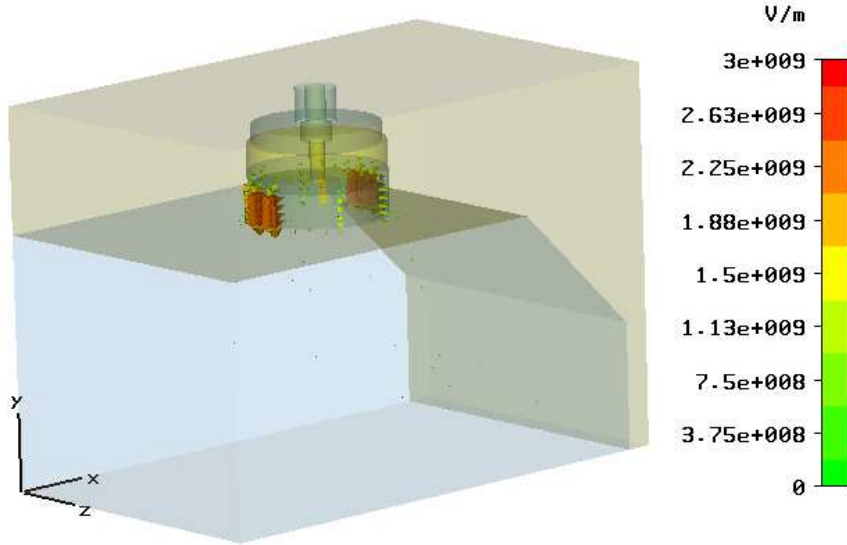
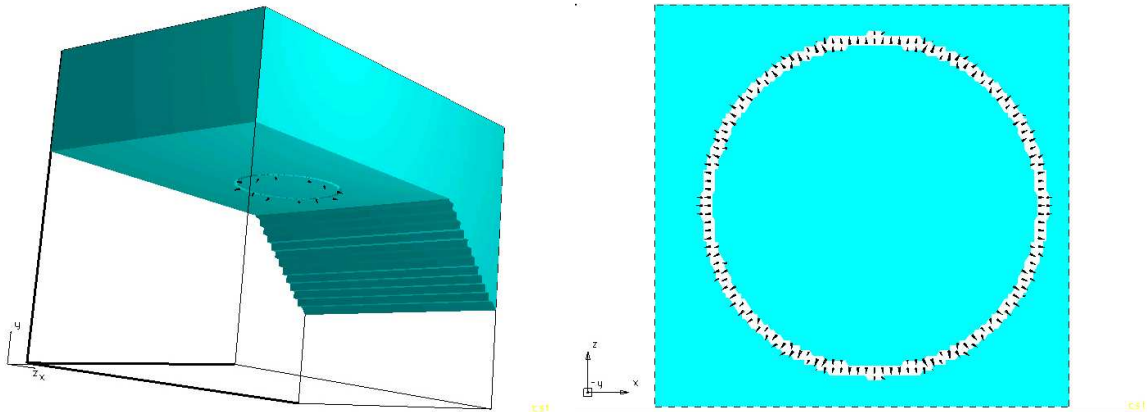


Figure 3.14: The electric field distribution corresponding to the seventh mode as calculated with MWST.



(a) Electric field distribution at the beam pipe for mode 1 from the MAFIA eigenmode solver. (b) Details of the electric field distribution near the button monitor of the BPM for mode 1 from the MAFIA eigenmode solver.

Figure 3.15: Electric field distribution for mode 1 from the MAFIA eigenmode solver.

3.5.3 Time domain computations for BPMs in the normal beam pipe

3.5.3.1 Scattering parameter

For the time domain computations, the coaxial port of the BPM has been modeled as a waveguide port. To ensure that the port definition has been correctly implemented into the MAFIA model, time domain simulations of scattering parameters for the same structure with MAFIA and MWST were compared. The boundaries in the z -direction

3.5 Simulation results for PETRA III beam position monitors

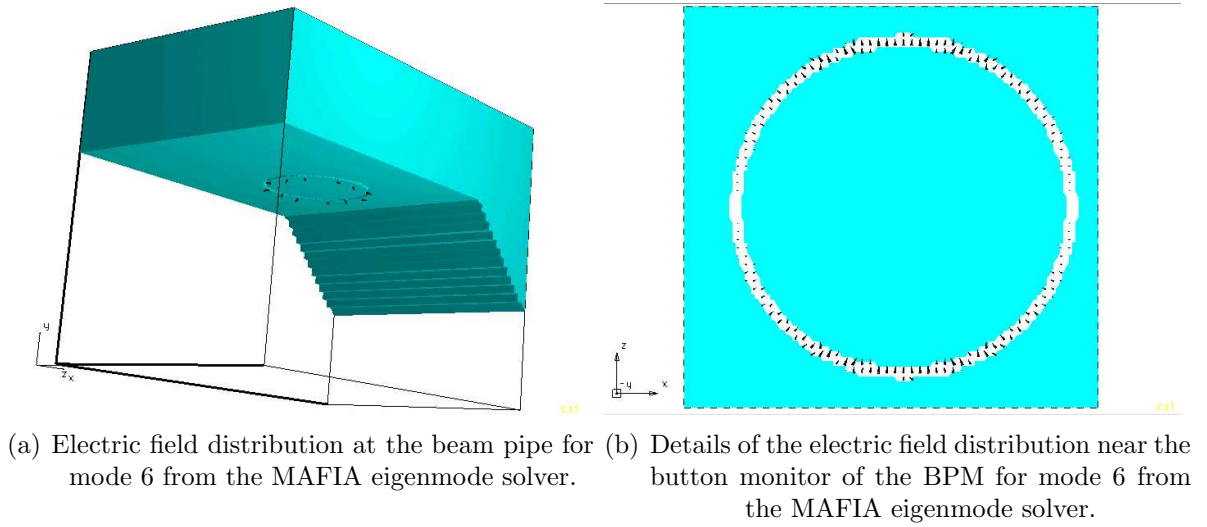


Figure 3.16: Electric field distribution for mode 6 from the MAFIA eigenmode solver.

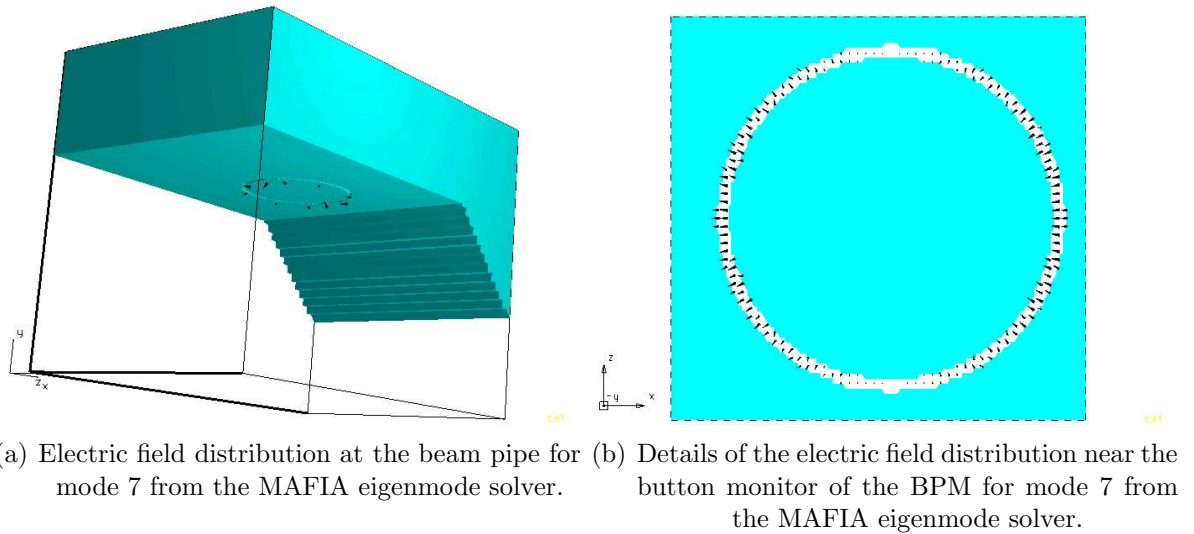


Figure 3.17: Electric field distribution for mode 7 from the MAFIA eigenmode solver.

were taken as electric boundaries. The phases of the reflection coefficient (S_{11}) recorded at the coaxial port computed with MAFIA and MWST are shown in Fig. 3.18. The good agreement between the obtained results strongly supports the accuracy of the computations and consistency of the meshing. The amplitude of the reflection coefficient in the considered frequency band computed by both the programs is one, due to the short circuit at the z -boundaries. Here it may be mentioned that in reality the coaxial waveguide port should have a 50Ω impedance. For the limitations in mesh resolution, the modeled waveguide port has an impedance of nearly 41Ω .

3. Wake Computations and Related Analysis for PETRA III

3.5.3.2 Wake computations for on-axis beam

In the next step, the time-domain computations for the wake fields were done. A beam with an rms bunch length (σ_z) of 10 mm, traversing the BPM on axis in the vacuum chamber, was used as the excitation source. For the simulation a Gaussian charge distribution with a total charge of 1 C was used. The beam pipe was considered to be 100 mm long, stretching equally at both sides of the discontinuity (the BPM). A cut through the geometry is shown in Fig. 3.19. A uniform mesh step size of 0.12 mm along the z-axis was used, which is a compromise between the available computer memory and the necessity to model the small gap of 0.4 mm between the BPM button and the vacuum chamber.

A wakefield monitor has been placed at $x = y = 0$ to record the wakefields as a function of the bunch coordinate (s). The z-component of the wake potential (longitudinal wake) and the bunch charge density versus the bunch coordinate are shown in

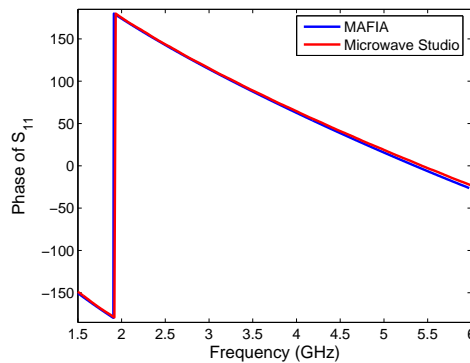


Figure 3.18: Comparison of phase vs. frequency of S_{11} computed with MWST and MAFIA at the coaxial BPM port.

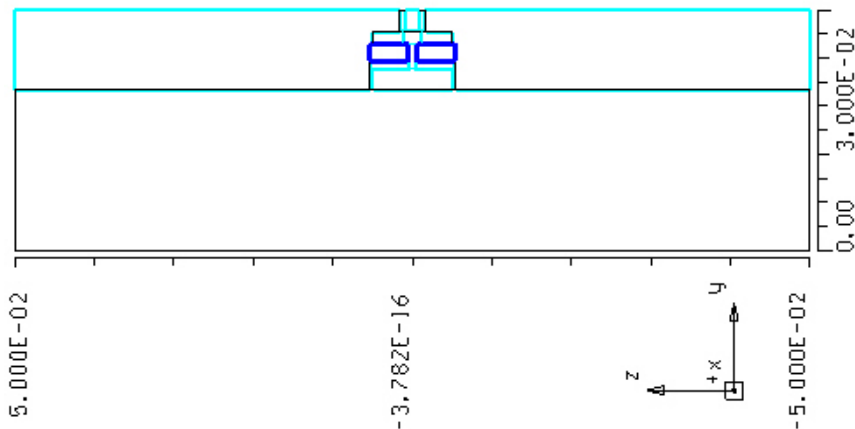


Figure 3.19: Cross section (yz plane) of the beam pipe along with the BPM.

3.5 Simulation results for PETRA III beam position monitors

Fig. 3.20.

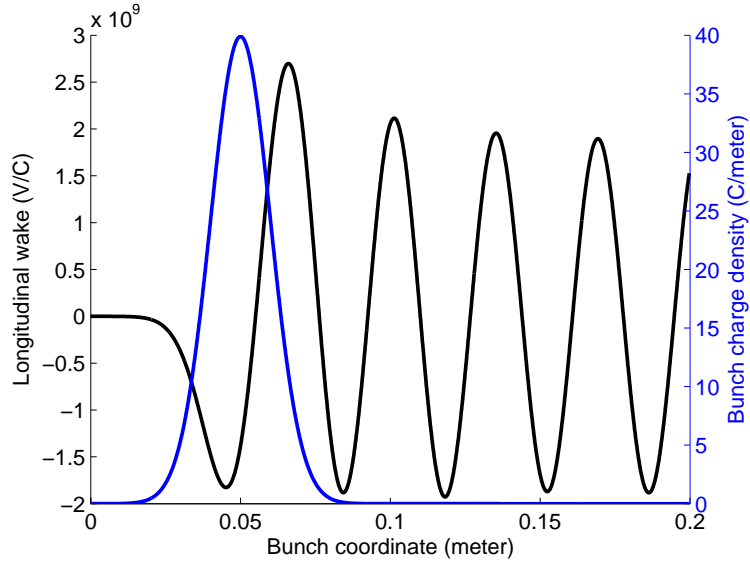


Figure 3.20: The z-component of the wake and the bunch charge density vs the bunch coordinate.

The total loss parameter computed according to equation (3.4) is found to be -4.0744×10^8 V/C. It is sufficient to evaluate the integral in equation (3.4) from zero to $10\sigma_z$ since the particle density is zero for $s > 10\sigma_z$. The trapezoidal rule was used for the integration and an interpolation of the wake data within the integration limit was used. The $k(1)$ parameter comes out to be -1.0266×10^{11} VC $^{-1}$ m $^{-1}$.

The wake calculations have been repeated with a finer mesh step. For a mesh size of 0.1 mm along the z-axis the loss parameter is -3.5276×10^8 V/C while the $k(1)$ parameter is -9.0985×10^{10} VC $^{-1}$ m $^{-1}$.

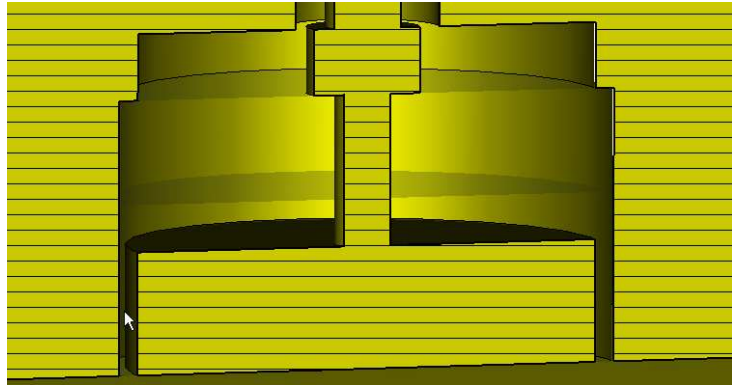
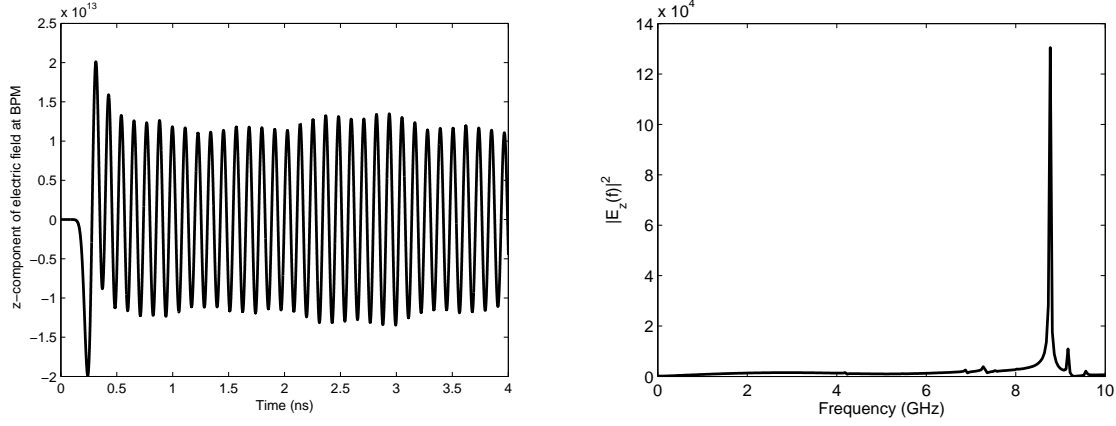


Figure 3.21: The position (indicated by the arrow) at which the electric field components are monitored at the BPM.

3. Wake Computations and Related Analysis for PETRA III



(a) Variation of the z-component of electric field in the time domain. (b) Frequency spectrum of the z-component of the electric field.

Figure 3.22: The z-component of electric field recorded at the position indicated in Fig. 3.21 in time and frequency domain.

From the previous eigenmode computations, it has turned out that some of the eigenmodes are trapped in the vicinity of the BPM. These modes can contribute significantly to the long range wake. To investigate this point in detail, electric field monitors (for all three components of the electric field) have been defined during the simulation time at a point near the BPM-button. The approximate position of the field monitor is shown by the arrow in Fig. 3.21.

The variation of the z-component of the electric field as a function of time at the field monitor position is plotted in Fig. 3.22(a). The frequency of the field is estimated from the time period. It comes out to be approximately 8.6 GHz - which is near to the frequencies of the 6th and 7th eigenmodes found with the eigenmode solver of MAFIA and MWST. A Discrete Fourier Transform (DFT) applied to the recorded electric field shows [Fig.3.22(b)] that the actual values of the associated frequencies are 8.773 GHz. A relatively weak oscillation around 9.17 GHz can also be noticed from the frequency spectra.

3.5.3.3 Estimation of the quality factors and other cavity parameters

The quality factors of the modes 6 and 7 were calculated with the codes MAFIA and MWST according to the equations 3.17. For these computations the conductivity of copper was taken as $5.8 \times 10^7 (\Omega\text{m})^{-1}$. The dielectric constant and the loss tangent of the Al_2O_3 ceramic disk were taken as 9.5 and 5×10^{-4} , respectively. The quality factors obtained from MWST are 758 and 847 for the 6th and the 7th mode, respectively. It has to be stated here that the frequencies of the 6th and the 7th modes from MWST come out to be 9.036 GHz and 9.038 GHz, respectively. This is quite far apart from the corresponding resonant frequencies obtained using MAFIA which are 8.712 GHz and 8.7476 GHz, respectively. The quality factors for the same modes obtained from

3.5 Simulation results for PETRA III beam position monitors

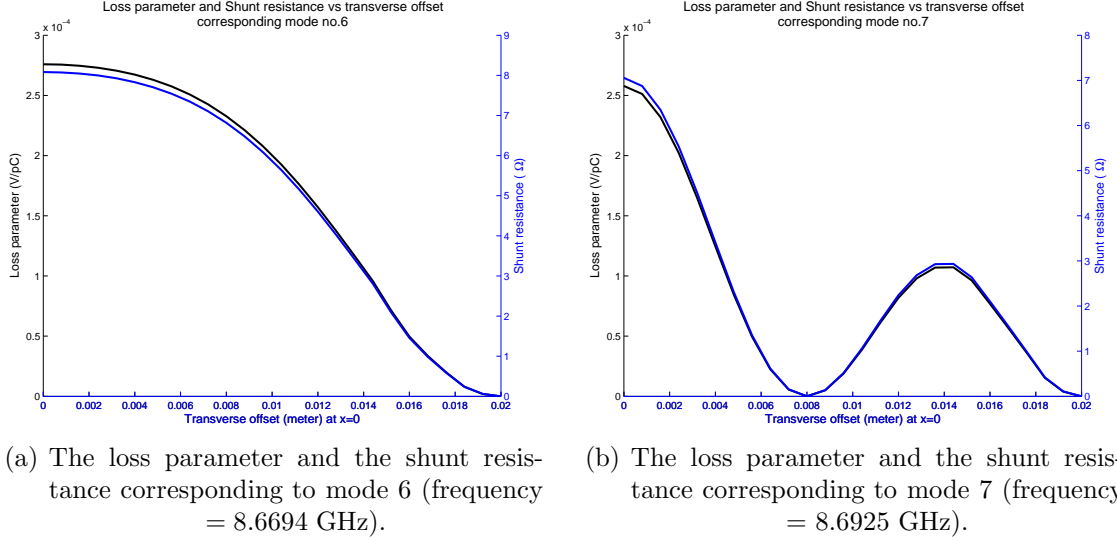


Figure 3.23: Loss parameters and shunt resistances corresponding to the 6th and 7th mode as functions of radial offset.

MAFIA are 753 and 707, respectively. The deviations of the resonant frequencies can be explained by the difference in modeling of the structure in MAFIA and in MWST. In the MAFIA calculations, the gap between the electrode of the button monitor and the shielding looks quite rough, whereas the accuracy of the MWST model is much better due to the partially filled cells. However, the differences in the quality factors computed with MAFIA and MWST are in an acceptable range. Another point to keep in mind is that the actual surface resistance of the metallic parts of the structure is about 10% higher than the theoretical surface resistance - leading to a lower conductivity of copper than the theoretical one ($\sigma_{copper} = 5.8 \times 10^7 (\Omega \text{ m})^{-1}$) used for the loss calculations.

The loss parameter $k(r)$, the shunt resistance $R(r)$ and the parameter G_1 were calculated in the next step, according to the equations 3.13-3.24. The values of G_1 was found to be 18.3Ω and 17.3Ω for the 6th and the 7th mode, respectively. The plots of the loss parameter and the shunt resistance as a function of radial offset are shown in Figs. 3.23(a) and 3.23(b) respectively.

3.5.3.4 Wake computations for off-axis beam

The next step was to compute the wakes for an off-axis beam. In this case it is no longer sufficient to consider one quarter of the structure since the symmetry for at least plane is lost. Therefore one half (considering a beam offset in only one transverse direction) of the beam pipe has been modeled instead of only one quarter. A cut along the z -axis and a cross section of the beam pipe as modeled in MAFIA for wake computations for a beam with a y -offset are shown in Figs. 3.24(a) and 3.24(b), respectively.

For the wake computations, both the upper and the lower coaxial ports were modeled as waveguide ports. The simulation results for the longitudinal wake (z -component of

3. Wake Computations and Related Analysis for PETRA III

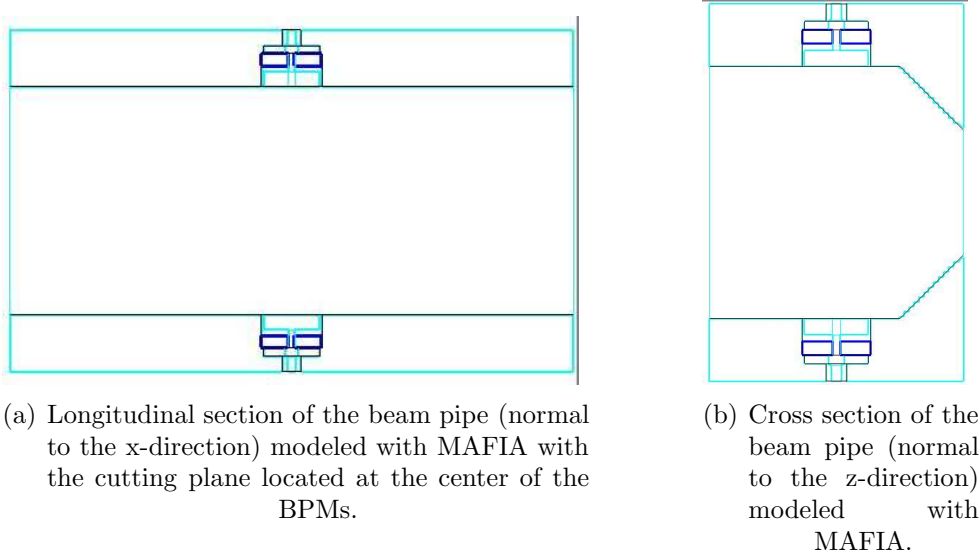


Figure 3.24: Cross sections of the beam pipe for off-axis wake computations at two different planes.

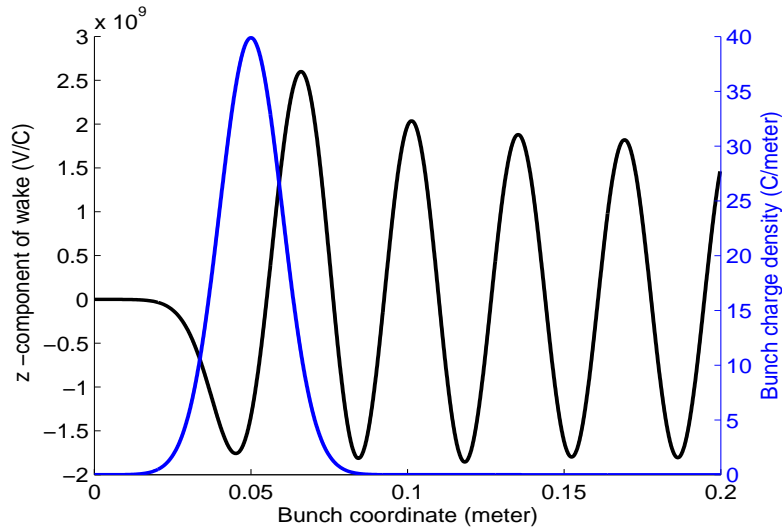


Figure 3.25: The z-component of the wake potential and the bunch charge density vs the bunch coordinate for a 5 mm y-offset of the beam (coarse mesh).

the wake), y-component of the wake and the output wave amplitudes at both coaxial waveguide ports are shown in the Figs. 3.25, 3.26 and 3.27, respectively. In this case an offset of 5 mm in the y-direction was considered. The wave amplitude recorded at the upper and the lower coaxial ports are different, as is expected. The wave amplitude at the upper coaxial port is larger than that at the lower port because the beam is now nearer to the upper coaxial port. The difference between these two wave amplitudes has

3.5 Simulation results for PETRA III beam position monitors

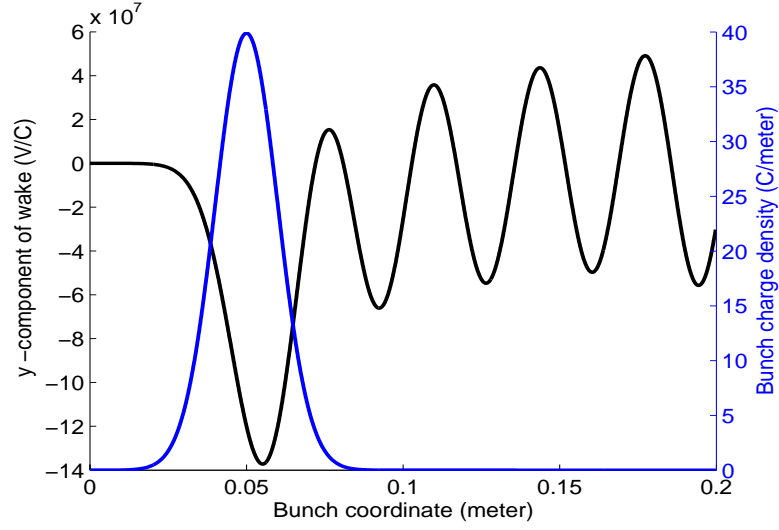


Figure 3.26: The y-component of the wake potential and the bunch charge density vs the bunch coordinate for a 5 mm y-offset of the beam (coarse mesh).

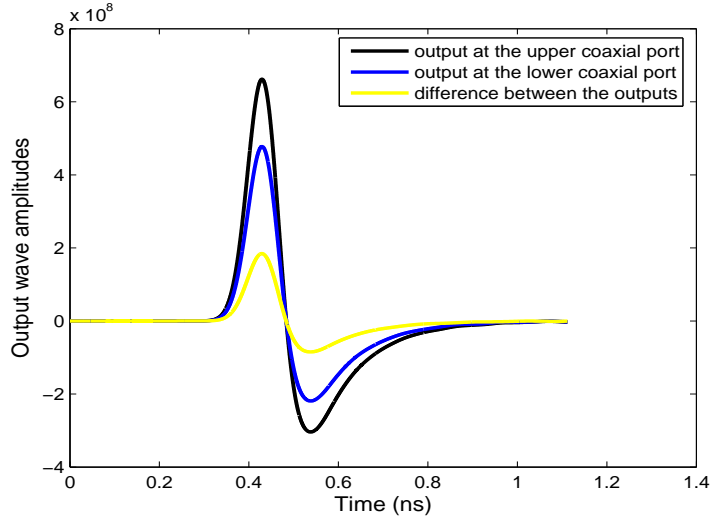


Figure 3.27: The output wave amplitude vs time at the coaxial ports for a y-offset of 5 mm (coarse mesh).

also been plotted versus time in the same graph. The loss parameter (k_{\parallel}) and the $k_{\parallel}(1)$ -parameter computed according to equations (3.4) and (3.5) for a 5 mm y-offset of the bunch are found to be -3.9167×10^8 V/C and -9.8876×10^{10} VC $^{-1}$ m $^{-1}$, respectively. With a finer meshing, the same parameters come out to be -3.3527×10^8 V/C and -8.6656×10^{10} VC $^{-1}$ m $^{-1}$, respectively.

The kick parameter has been calculated using equation (3.6) and the y-component W_y of the wake potential. The y-kick parameter, normalized to the y-offset of 5 mm,

3. Wake Computations and Related Analysis for PETRA III

comes out to be $-17.842 \times 10^9 \text{ VC}^{-1}\text{m}^{-1}$. The same parameter with a finer mesh comes out to be $-25.256 \times 10^9 \text{ VC}^{-1}\text{m}^{-1}$. The difference of the loss and kick parameters for different mesh resolutions show that the obtained results have not fully converged, but the order of these parameters are estimated correctly. Unfortunately, the present computation power does not allow us to extend the convergence studies beyond this limit.

3.5.4 Eigenmode computation results for BPMs in the narrow beam pipe

Near the undulator chambers the beam pipe will be very narrow along one axis in order to efficiently utilize the undulator magnetic fields. In this case the mounted BPMs will be much nearer to the beam - which can lead to larger wakes in those sections than in the normal beam pipe sections. For a first evaluation of the wake fields due to the BPMs in this section, the same button BPMs have been considered in the undulator chamber arranged in similar way to the BPM in the normal arc. The cross-section of the beam pipe is, in this case, also an ellipse, but the minor axis is much smaller (minor axis = 7 mm, major axis = 90 mm) than that of the arc beam pipe. The BPM buttons are placed 5 mm apart from the center. For the sake of comparison, the geometry and the dimensions of the BPM buttons and feed-throughs have been considered to be the same as in the arc. To model the structure, as in the arc, the elliptical cross section of the beam pipe has been approximated by a polygon. Although with MWST, it is possible to model the elliptical beam pipe without the polygon approximation, the same geometry (with polygon approximation) have been modeled with MWST, for consistency. The MWST model for the approximated structure is shown in Fig. 3.28(a). The meshing details near the BPM button, created by the MWST mesh generator has also been shown in Fig. 3.28(b).

The results of the eigenmode computations with the MWST and MAFIA eigen-

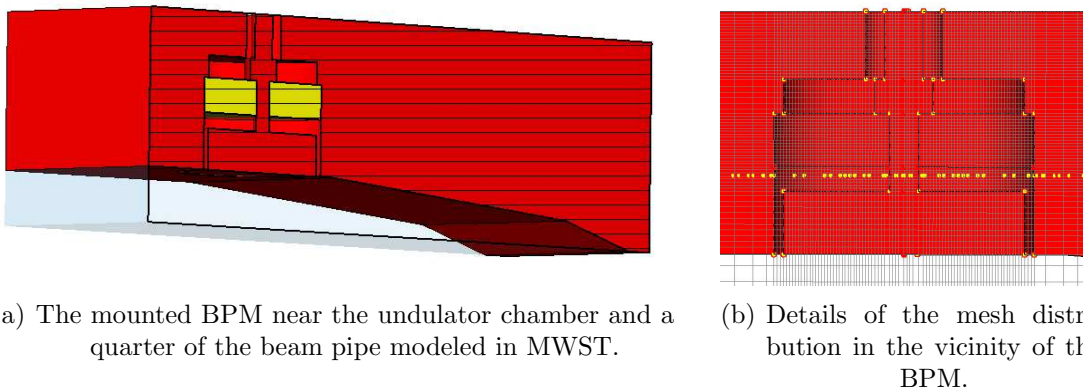


Figure 3.28: MWST model of the BPM mounted at the beam pipe near the undulator chamber and details of the corresponding mesh.

3.5 Simulation results for PETRA III beam position monitors

Mode Number	Resonant frequencies (GHz)			
	Electric wall at z-boundaries		Magnetic wall at z-boundaries	
	MAFIA	MWST	MAFIA	MWST
1	1.9185	1.9273	1.9186	1.9162
2	8.7921	8.9966	8.7916	8.9729
3	8.8578	8.9984	8.8582	8.9739
4	10.2571	10.2176	10.2571	10.1677
5	13.5909	13.6113	13.5907	13.5869
6	1.36049	13.6127	13.6052	13.5878
7	14.4717	14.5085	14.4718	14.5032
8	14.4980	14.5086	14.4978	14.5093
9	17.3480	17.2900	17.3480	17.3111
10	17.5003	17.4849	17.5003	17.4845

Table 3.6: Resonant frequencies computed with MAFIA and MWST for the BPM mounted at the narrow beam pipe with the set of boundary conditions shown in Table 3.4

mode solvers are summarized in Table 3.6. The set of boundary conditions used for the eigenmode computations are the same as the case of BPMs in the normal beam pipe (Table 3.4). From the eigenmode computation results it can be seen that all of the computed eigenmodes do not change with the boundary conditions at the z-boundaries. This suggests the possibility that all of these modes are bound to the BPM. The field distributions of these modes confirm this point. Fig. 3.29, 3.30 and 3.31 show the electric field distributions of the first three modes computed with MWST. It may be noted here that these three modes (modes 1, 2 and 3) are the same BPM modes which have been found in the previous section for the eigenmode calculations of the BPMs mounted at normal beam pipe.

3. Wake Computations and Related Analysis for PETRA III

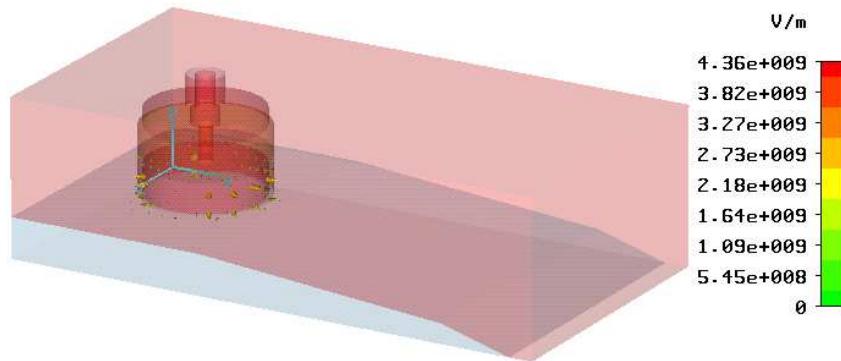


Figure 3.29: Electric field distribution of the first mode computed with MWST.

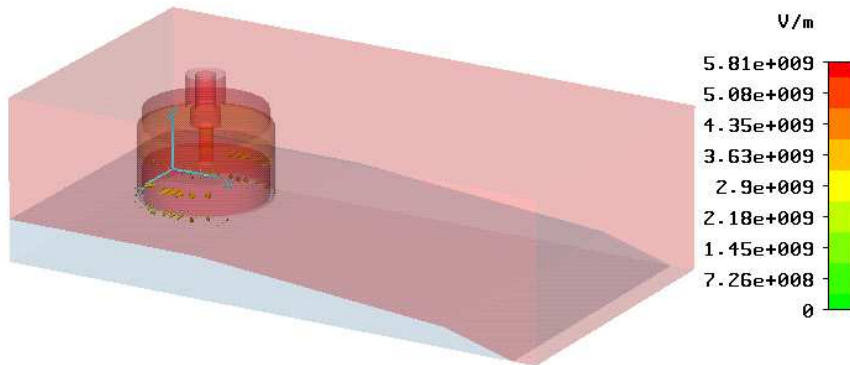


Figure 3.30: Electric field distribution of the second mode computed with MWST.

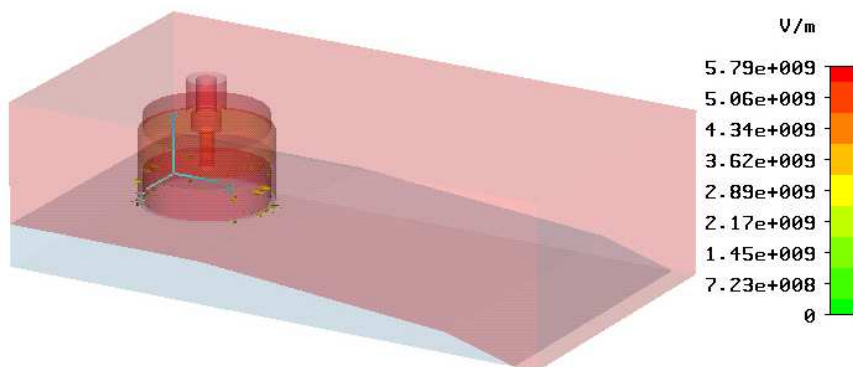


Figure 3.31: Electric field distribution of the third mode computed with MWST.

3.5.5 Time domain computations for the BPMs in the narrow beam pipe

3.5.5.1 Wake computations for on-axis beam

Half of the beam pipe with two waveguide ports (one at the upper coaxial port and another at the lower coaxial port) has been modeled in MAFIA for the wake computations. It may be noted here that in this case half of the beam pipe has been used for both the cases of on- and off-axis wake computations. The cross section of the narrow beam pipe along with the BPM is shown in Fig. 3.32, as modeled with MAFIA. The beam pipe was considered to be 100 mm long. As in the previous case, a Gaussian charge distribution with $\sigma = 10$ mm having a total charge of 1 C has been taken as the exciting beam. The constant mesh step along z-direction and the fine mesh step around the BPM button have been taken as 0.12 mm.

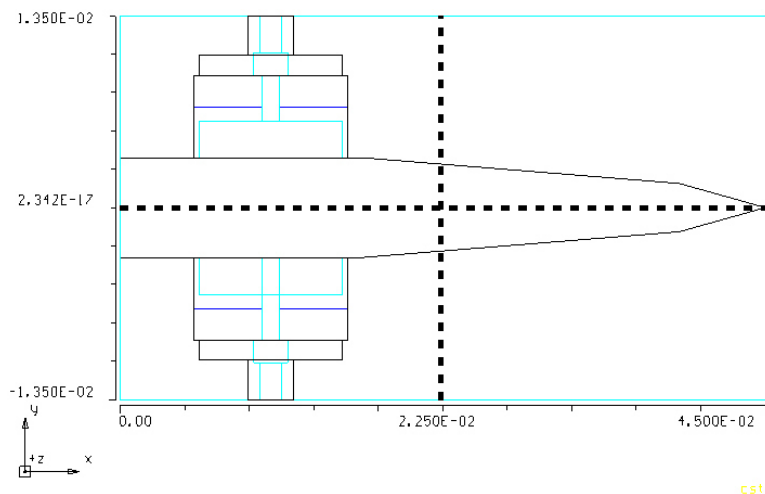


Figure 3.32: Cross section of the beam pipe and the BPM as modeled with *MAFIA*.

All the components of the wake have been recorded at the position of the beam. Fig. 3.33 shows the variation of the z-component of the wake with the bunch coordinate for an on axis beam. The output wave amplitudes at both coaxial ports were also recorded, which can be seen in Fig. 3.34. Although from Fig. 3.34 at first sight it seems that the output wave amplitudes are the same at the upper and lower coaxial ports, a detailed inspection shows that there is a small difference between the two recorded amplitudes. The details of the output amplitudes and their difference are shown in Fig. 3.35. It can be noted that the order of magnitude of the difference is much smaller than the recorded peak amplitude. This difference is probably caused by the difference in the sequence for numerical computation of curls at two symmetric positions (with respect to the xz plane). This is again supported by the fact that also a non-zero y-component of the wake field has been found for the on-axis beam as can be seen in

3. Wake Computations and Related Analysis for PETRA III

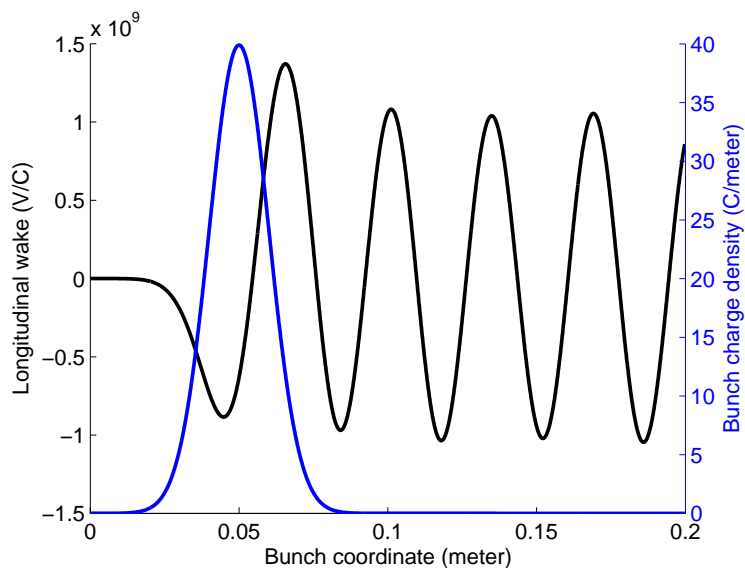


Figure 3.33: The z-component of the wake and the bunch charge density vs the bunch coordinate (on-axis beam).

Fig. 3.36.

To investigate the possibility of any trapped modes near the BPM button, similar procedure described in section 3.5.3.2 has been followed. An electric field monitor has been placed in the vicinity of the BPM button as shown in Fig. 3.21 to record all the

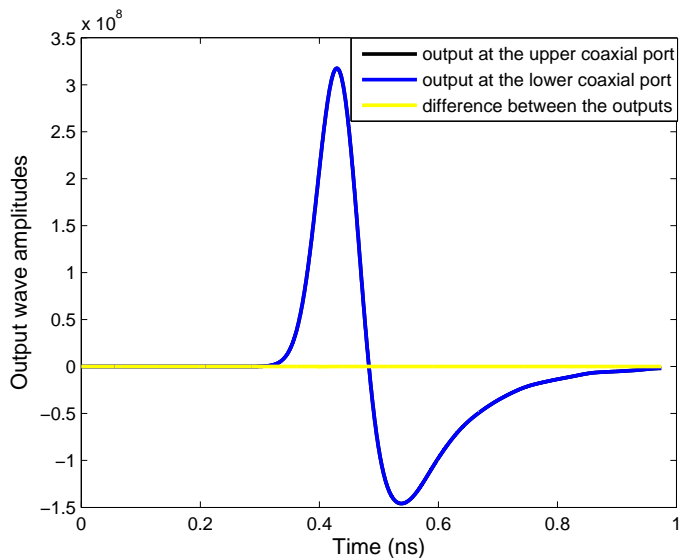
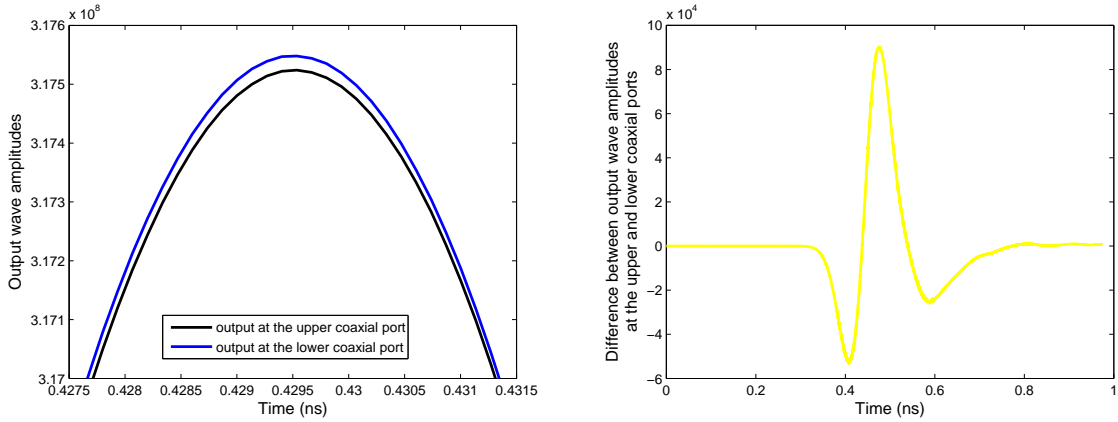


Figure 3.34: The output wave amplitudes vs time at the coaxial ports for the on-axis beam.

3.5 Simulation results for PETRA III beam position monitors



(a) Details of the output wave amplitude at the upper and lower coaxial ports for on axis beam. (b) Difference between the output wave amplitudes at the upper and lower coaxial ports vs time.

Figure 3.35: Details of the output wave amplitude at the upper and lower coaxial ports and their difference vs time.

three components of the electric field during the computation time. The z-component of the recorded electric field is shown in the frequency and time domain in Fig. 3.37. From Fig. 3.37(b) the frequency of the mode comes out to be 8.817 GHz, which is very close to the frequencies of the 2nd and 3rd eigenmode (Table 3.6). The quality factors of these two modes comes out to be 693 and 690 from MAFIA and 717 and 718 from MWST, respectively.

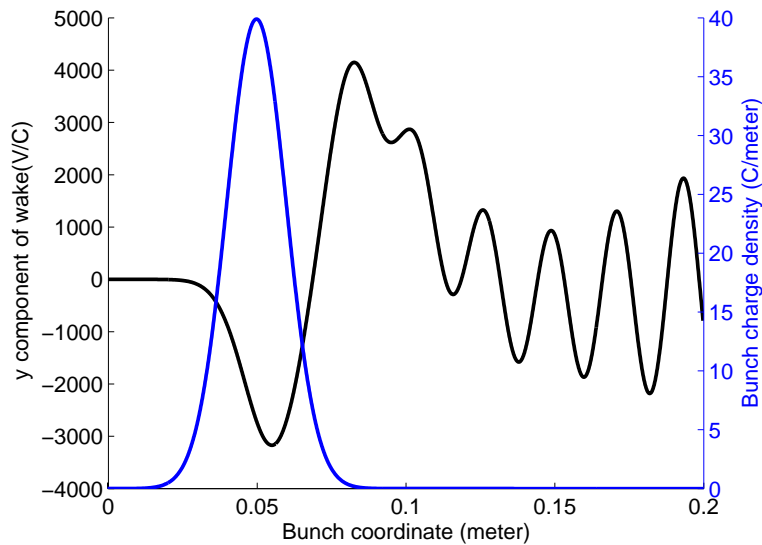
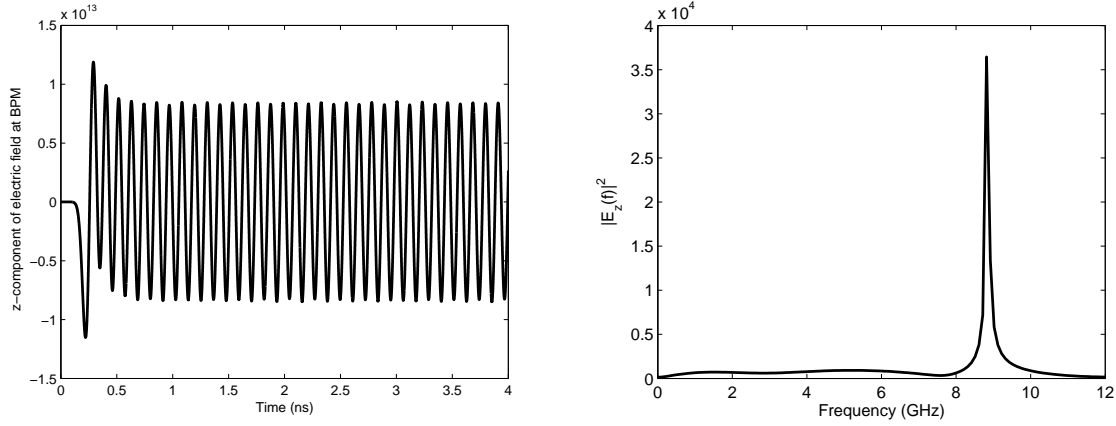


Figure 3.36: y-component of the wake for the on-axis beam.

3. Wake Computations and Related Analysis for PETRA III

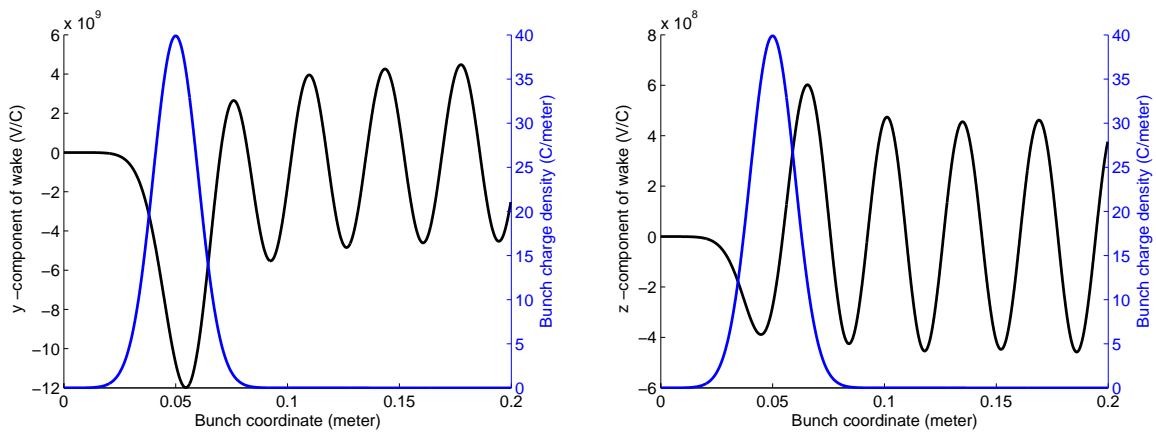


(a) Variation of the z-component of electric field in the time domain. (b) Frequency spectrum of the z-component of the electric field.

Figure 3.37: The z-component of electric field recorded at the position indicated in Fig. 3.21 in time and frequency domain for the BPMs in the narrow beam pipe.

3.5.5.2 Beam with y-offset

In the next step the wake computations have been done for a beam with an offset in the y-direction. As the beam pipe in this case is very narrow in the y-direction, an y-offset of 2.0 mm has been considered. The geometry of the beam pipe remains the same as shown in Fig. 3.32. All the components of the wake and the output wave amplitudes at the upper and lower coaxial ports have been recorded. Fig. 3.38 shows the y and z components of the wake along the beam pipe.



(a) y-component of the wake for the beam with 2 mm y-offset. (b) z-component of the wake for the beam with 2 mm y-offset.

Figure 3.38: y- and z- components of the wake along the bunch coordinate for a beam with a y-offset of 2 mm.

3.6 Simulation results for PETRA III longitudinal feedback cavity

Then the total loss parameter was calculated using equation (3.4). The estimated total loss parameter and $k_{\parallel}(1)$ -parameter come out to be -7.0962×10^7 V/C and -2.3176×10^{10} VC⁻¹m⁻¹, respectively. The y-kick parameter was computed using equation (3.6). The y-kick parameter normalized to an offset of 2 mm in this case is -3.874×10^{12} V/(C m).

3.6 Simulation results for PETRA III longitudinal feedback cavity

3.6.1 Longitudinal feedback cavity

The PETRA III synchrotron radiation facility will be operating in a multibunch mode. Multibunch operations of the accelerators are usually plagued with several instabilities which can considerably limit the desired beam current. The coupled bunch instabilities are among those instabilities which are severe constraints to achieve the desired beam current and shape. Employment of active bunch by bunch feedback system is one of the

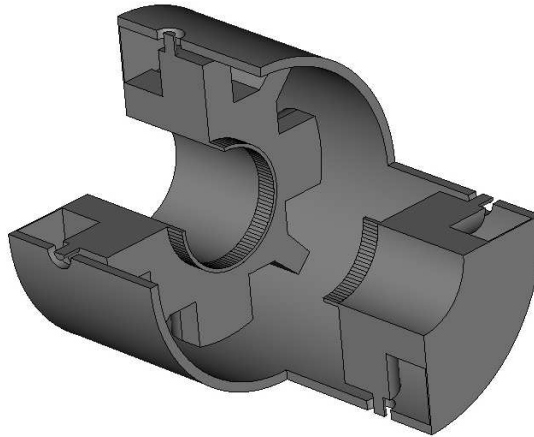


Figure 3.39: A cut view of the PETRA III longitudinal feedback cavity with nose cones.

most effective measures to dump coupled bunch instabilities. In these feedback systems, the deviations of bunches from their reference positions are measured and a correction signal is created based on the measured deviation. Afterwards, the correction signal is amplified and applied to the particle bunches. The amplified correction signal is applied to the particle bunches by means of the feedback cavities or ‘kickers’. Both longitudinal and transverse kickers are usually employed to deliver the appropriate component of kick. Several designs for the longitudinal feedback kickers exist, which includes the coaxial drift tube based design (ALS, PLS, PEP-II) [95], overdamped cavity based design (DAFNE, BESSY II, KEKB)[96], pill-box cavity with striplines (SRRC, TLS)

3. Wake Computations and Related Analysis for PETRA III

[97]. Among the designs mentioned above, the overdamped cavity based design is widely used and is planned to be used for PETRA III.

The longitudinal feedback cavity of PETRA III is basically a heavily loaded pillbox cavity. It has eight coaxial ports for connection to the driving amplifiers (input ports) and the dummy loads (output ports). A cut view of a longitudinal feedback cavity is shown in Fig. 3.39. A high shunt impedance (the ratio between the square of the kick voltage seen by the beam and the peak forward power at the input) and high bandwidth are usually the desired parameters for an efficient feedback cavity. It is known that in order to dump all of the coupled bunch instabilities, the required maximum bandwidth is $(f_{RF}/2)$, considering all the buckets filled. For a different filling mode, the bandwidth requirement will be different, depending upon the spacing between the bunches. For PETRA III, the maximum required bandwidth is 125 MHz, corresponding to a bunch spacing of 4 ns [88]. The high bandwidth of the cavity is achieved by strongly loading it with the special ridged waveguides which can be connected to the external loads.

3.6.2 Eigenmode computation results

The eigenmode solvers of MWST and MAFIA have been used to compute the resonant frequencies of the feedback cavity. The mesh views at two different planes of the cavity are shown in Fig. 3.40. The resonant frequencies of the first 14 modes according to the boundary conditions of Table 3.7, the modal loss parameters at zero offset and the quality factors computed with MAFIA are shown in Table 3.8. From the table, it can be seen that the resonant frequency of the first monopole TM_{010} mode which is to be used for the beam correction, is 1.3079 GHz with a quality factor of 10579.

The electric field distribution for the operating mode is shown in Fig. 3.41. It can be noted that the resonant frequency of the same TM_{010} mode without the nose cones comes out to be 1.398 GHz (1.392 GHz from MWST) - i.e. inclusion of the nose cones have lowered the resonant frequency of the operating mode. This may be of particular

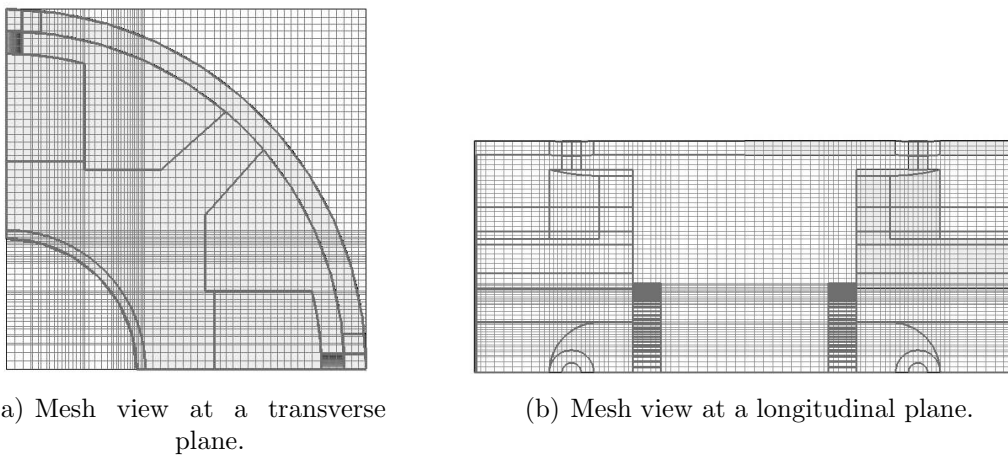


Figure 3.40: Mesh view at two planes for the feedback cavity.

3.6 Simulation results for PETRA III longitudinal feedback cavity

Boundaries	Boundary conditions
x-min, x-max	Magnetic, Electric
y-min, y-max	Magnetic, Electric
z-min, z-max	Magnetic, Magnetic

Table 3.7: Boundary conditions used for the eigenmode computations with MAFIA.

interest as there is a plan to use the nose cones for fine tuning the cavity. From Table 3.8 it can be noticed that below the cutoff frequency of the beam pipe (2.93 GHz for the TE Modes and 3.82 GHz for the TM modes) the resonant modes at frequencies 1.7692, 2.0782 and 2.4906 GHz are having relatively high loss factors. Details of the electric field distributions of these modes are shown in Figs. 3.42, 3.43 and 3.44, respectively. The conductivity of copper has been taken as $5.8 \times 10^7 (\Omega m)^{-1}$ for the computations. As can be noticed from the figures the electric field distribution is strong around the ridges of the waveguide and have a relatively weak distribution around the beam pipe for the modes near 1.77 GHz and 2.08 GHz.

Mode No.	Frequency (GHz)	Quality factor	Loss Parameter (offset = 0) [V/(p C)]
1	1.3079	10579	3.39×10^{-1}
2	1.7692	4619	1.87×10^{-2}
3	1.9281	4236	5.17×10^{-10}
4	1.9885	4151	2.82×10^{-9}
5	2.0782	4730	3.59×10^{-2}
6	2.4906	9604	7.69×10^{-2}
7	2.7216	17380	2.09×10^{-11}
8	3.1752	23884	1.77×10^{-12}
9	3.4582	26473	1.23×10^{-3}
10	3.6513	14719	2.76×10^{-11}
11	3.7201	22717	3.69×10^{-4}
12	3.8162	16699	1.37×10^{-2}
13	3.8610	13901	5.93×10^{-3}
14	4.0116	11485	1.03×10^{-10}

Table 3.8: The resonant frequencies, quality factors and modal loss parameters for the first 14 modes of the longitudinal feedback cavity. The corresponding boundary conditions are shown in Table 3.7.

3. Wake Computations and Related Analysis for PETRA III

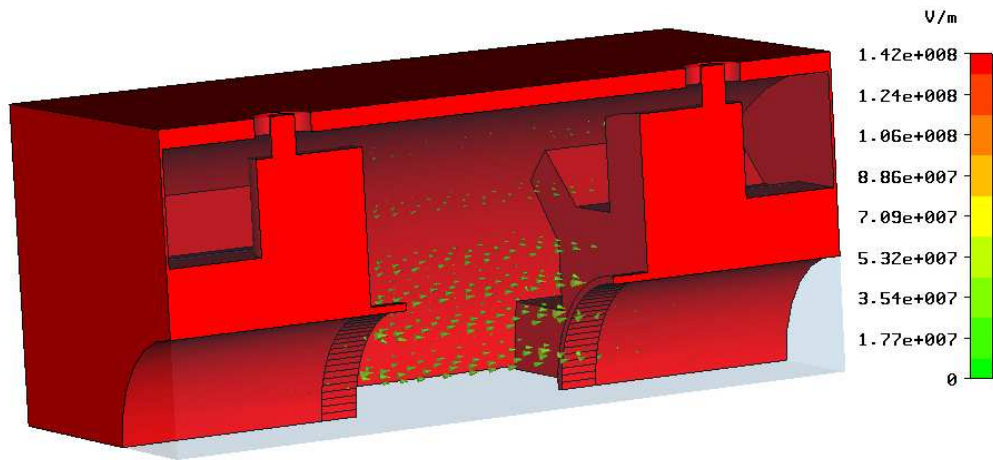


Figure 3.41: Electric field of the operating TM_{010} like mode of the longitudinal feedback cavity.

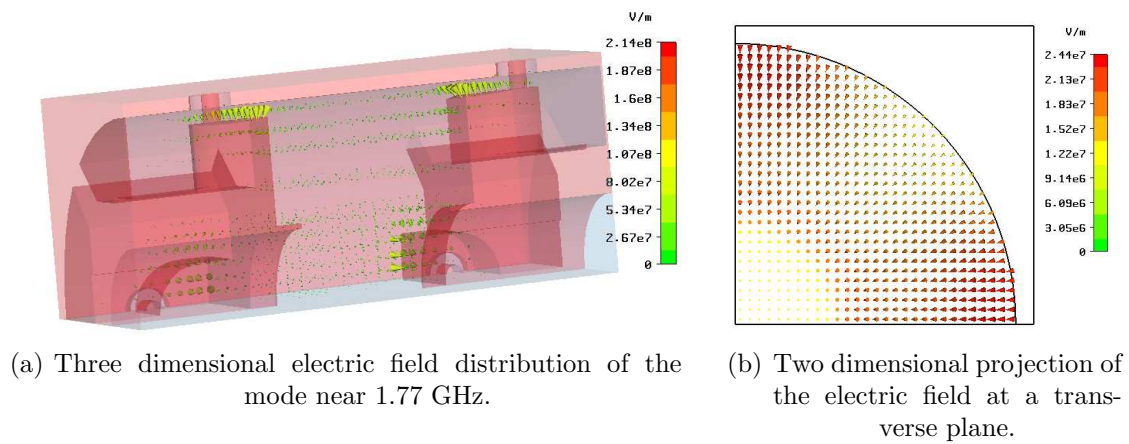


Figure 3.42: Details of the electric field near 1.77 GHz.

3.6 Simulation results for PETRA III longitudinal feedback cavity

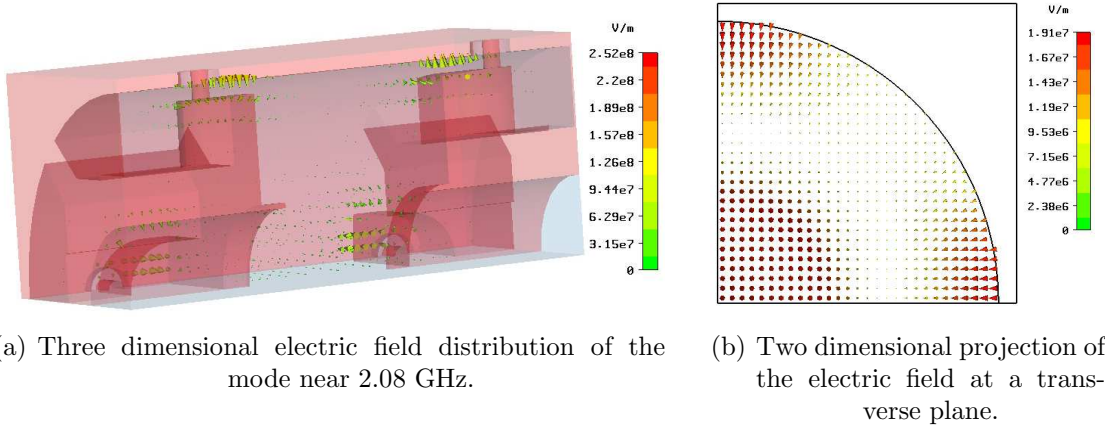


Figure 3.43: Details of the electric field at 2.08 GHz.

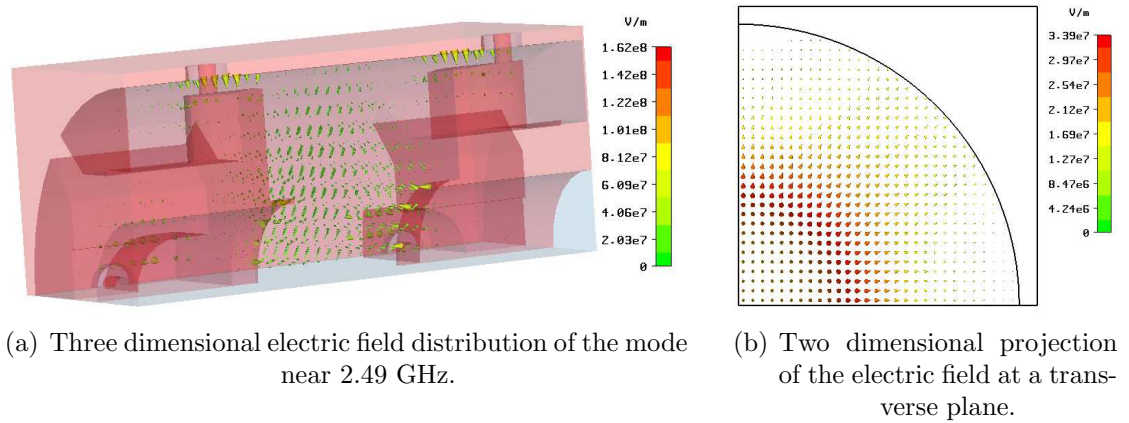


Figure 3.44: Details of the electric field at 2.49 GHz.

3. Wake Computations and Related Analysis for PETRA III

3.6.3 Time domain computations

3.6.3.1 Scattering parameters

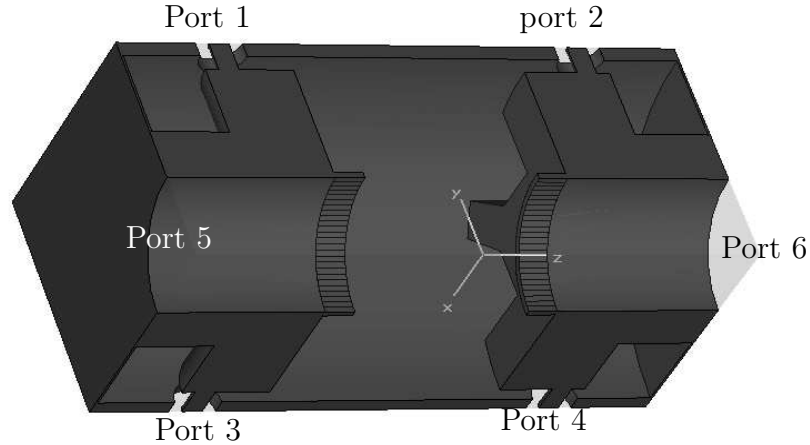
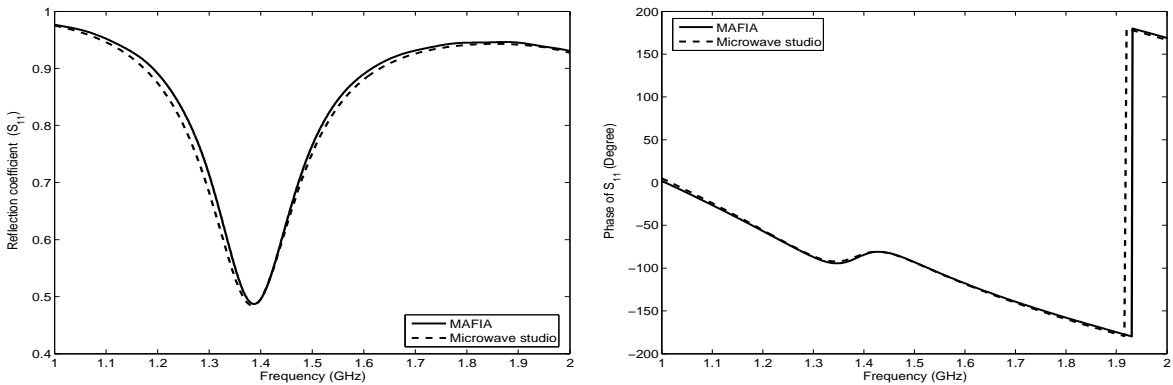


Figure 3.45: One quarter of the PETRA III longitudinal feedback cavity with the relevant coordinates and the assigned ports.

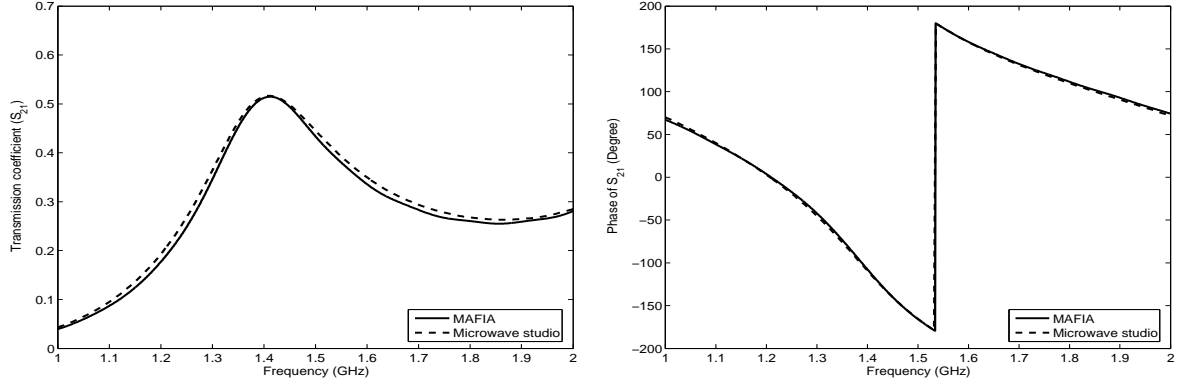
For the time domain computations of the feedback cavity, it has been modeled as a six-port device. Due to its symmetry, only one quarter of the structure was modeled. Among the six ports, four are the coaxial ports to be connected to the amplifiers and external loads. The other two ports are waveguide ports due to the beam pipe. The modeled geometry is shown in Fig. 3.45, along with the relevant coordinate system and the assignment of the ports. Only one half of each of the coaxial port is visible in the figure. The cutoff frequencies of the first five TM modes of the beam pipe are listed in



(a) Amplitude of the reflection coefficient at port 1. (b) Phase of the reflection coefficient at port 1.

Figure 3.46: Amplitude and phase of the reflection coefficient at port 1.

3.6 Simulation results for PETRA III longitudinal feedback cavity



(a) Amplitude of the transmission coefficient from port 1 to port 2. (b) Phase of the transmission coefficient from port 1 to port 2.

Figure 3.47: Amplitude and phase of the transmission coefficient from port 1 to port 2.

Table 3.9. It can be noted here that the operating frequency of the feedback cavity is 1.3079 GHz, which is well below the cutoff frequency of the beam pipe. So, there should be no influences of the beam pipe on the kicker performances in the desired frequency band. For the scattering parameter computations, the structure has been excited with a Gaussian Pulse through the coaxial port 1. All the other ports have been terminated with their corresponding wave impedances. The amplitude and phase of the reflection coefficient at port 1 are shown in Fig. 3.46. The same for the transmission coefficient from port 1 to port 2 are shown in Fig. 3.47. The agreement between the results from two softwares confirms the consistency in modeling the structure with both the softwares. To verify the point of coupling of the higher order modes of the beam pipe, the same time domain analysis has been done with electric short circuits at the both beam pipes. But no significant difference in the results could be found, which confirms that there are no coupling between the beam pipe and the cavity in that frequency range. It may be noted here that the whole structure has been taken as loss less and the automesh

Mode Number	Cutoff frequency (GHz) MWST	Cutoff frequency (GHz) MAFIA
1	3.822	3.829
2	4.852	4.852
3	8.12	8.174
4	8.42	8.443
5	8.73	8.789

Table 3.9: Cutoff frequencies of the first five TM waveguide modes of the PETRA III longitudinal feedback cavity beam pipe computed with MWST and MAFIA.

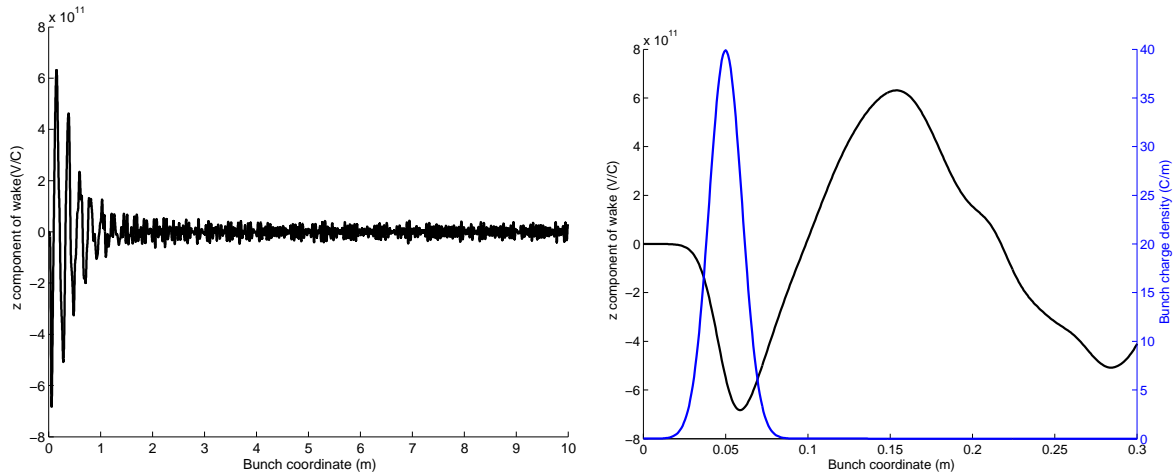
3. Wake Computations and Related Analysis for PETRA III

facility of the MWST have been used. For the MAFIA computations a manual meshing has been used. The difference between the two meshing schemes can be the cause of the slight difference of the computed results.

3.6.3.2 Wake computations with on-axis beam

The time domain wake computations have been done for the feedback cavity with an uniform mesh step size of 0.77 mm along the z -axis. This is a compromise between the available computer memory and the necessity to model the small details of the cavity geometry. A beam with an rms bunch length (σ_z) of 10 mm, traversing the feedback cavity on axis, has been used as the excitation source. The #1dcurrent section of the MAFIA module T3 has been used to determine the excitation properties. A Gaussian charge distribution with a total charge of 1 C has been used. A wakefield monitor has been placed at $x = y = 0$ to record the wakefields as a function of the bunch coordinate (s). The z -component of the wake potential (longitudinal wake) and the bunch charge density versus the bunch coordinate are shown in Fig. 3.48. Fig. 3.48(b) shows the variation of the longitudinal wake potential and the bunch charge density used for the wake computations along 0.3 meter of the bunch coordinate. Fig. 3.48(a) shows the variation of the wake along 10 meters of the bunch coordinate. The wakes were recorded for such a long time to have enough resolution for computing the impedance spectrum. The longitudinal loss parameter and the $k(1)$ parameter computed according to the equations 3.4 and 3.5 comes out to be -4.6997×10^{11} V/C and 1.7489×10^{13} V/(C m), respectively.

In order to compute the impedances of the cavity in frequency domain, a Discrete



(a) Longitudinal (z) component of the wake for PETRA III feedback cavity along 10 meters of the bunch coordinate. (b) Longitudinal (z) component of the wake for PETRA III feedback cavity and the bunch charge distribution along 0.3 meters of the bunch coordinate.

Figure 3.48: Longitudinal component of the wake along the bunch coordinate.

3.6 Simulation results for PETRA III longitudinal feedback cavity

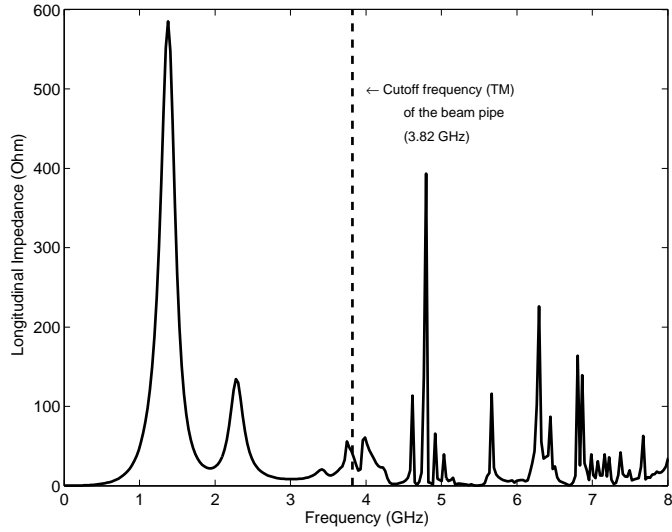


Figure 3.49: Longitudinal impedance versus frequency for the longitudinal feedback cavity.

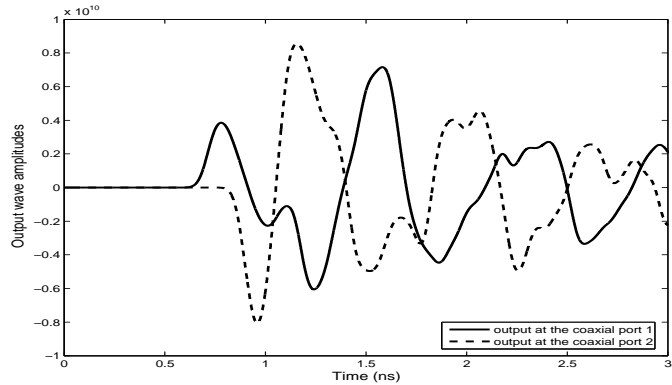
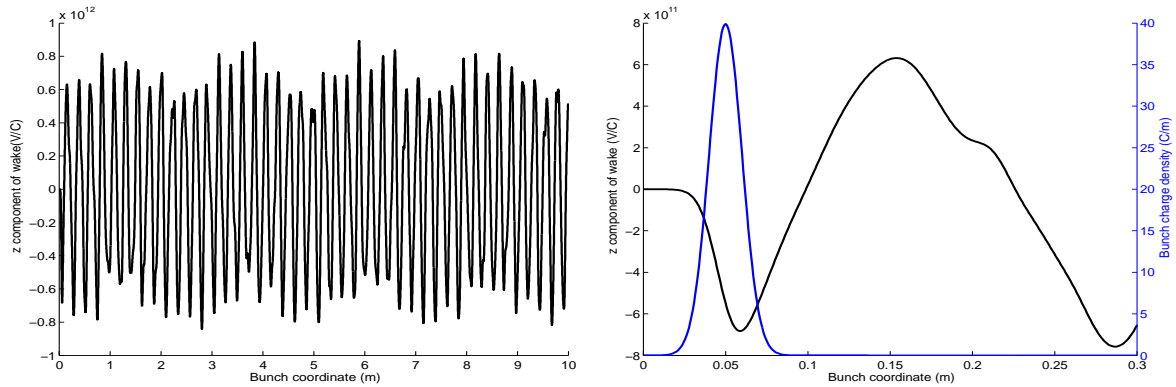


Figure 3.50: Output wave amplitudes at ports 1 and 2 during the wakefield computation.

Fourier Transform (DFT) has been applied to the longitudinal wakes shown in Fig. 3.48. The obtained impedance spectra result has been normalized to the bunch spectrum. Fig. 3.49 shows the longitudinal impedance spectrum of the feedback cavity. As can be seen from the figure that under the cutoff frequency of the kicker some impedance peaks are visible due to the resonant modes of the cavity. Above the cut off of the beam pipe more or less continuous spectra has been obtained which are due to the modes of the beam pipe. From the plot, it may be noticed that the frequency of the first peak (corresponding to the operating mode of the cavity) is 1.379 GHz. This is a bit higher than the computed resonant frequency of the cavity fundamental mode (Table 3.8). The reason for the difference is, for the eigenmode computations the coaxial ports of the cavity have been treated as short circuited. On the other hand, for the time domain wake computations they have been terminated with corresponding matched termination.

3. Wake Computations and Related Analysis for PETRA III



(a) Longitudinal (z) component of the wake for the PETRA III feedback cavity along 10 meters of the bunch coordinate with the coaxial ports terminated with short circuits. (b) Longitudinal (z) component of the wake for the PETRA III feedback cavity and the bunch charge distribution along 0.3 meters of the bunch coordinate with the coaxial ports terminated with short circuits.

Figure 3.51: Longitudinal component of the wake along the bunch coordinate with short circuited coaxial ports.

Besides the peak due to the fundamental cavity mode, presence of another impedance peak at 2.278 GHz can be noticed. The output wave amplitudes recorded at ports 1 and 2 are shown in Fig. 3.50. As the beam has been launched from the left hand side, which is nearer to the port 1, the recorded wave amplitude at port 1 becomes non-zero at first. Due to the symmetry of the cavity, the output signals recorded at ports 3 and 4 are exactly same as those recorded at port 1 and 2.

To investigate the influence of the short circuits on the coaxial waveguide ports, the

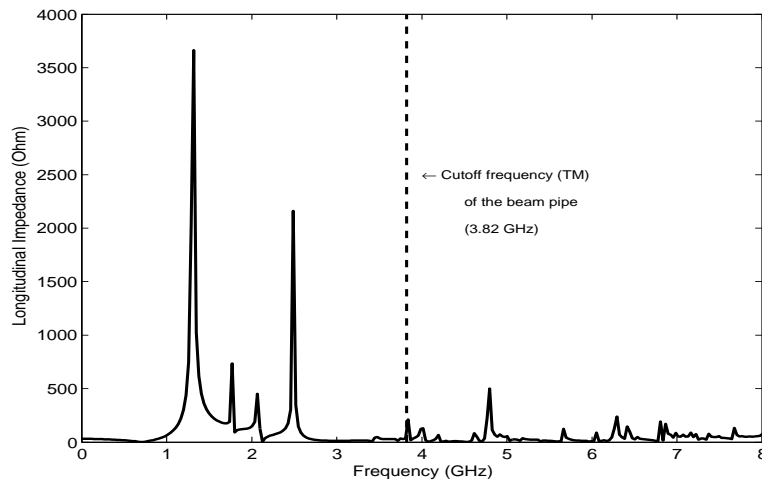


Figure 3.52: Longitudinal impedance versus frequency for the longitudinal feedback cavity with coaxial ports terminated with short circuits.

3.6 Simulation results for PETRA III longitudinal feedback cavity

wake computations were repeated with short circuits to all the coaxial ports, keeping all the other parameters unchanged. The resulting longitudinal wake potential along the bunch coordinate can be seen in Fig. 3.51. As in the previous plot, the variation of the wake potential along 10 m of the bunch coordinate is shown in Fig. 3.51(a). Fig. 3.51(b) shows the details of the short range wake along with the bunch charge density at the beginning of the bunch coordinate. The effect of matched termination at the coaxial waveguide ports are clearly noticeable comparing the variation of the wakes as plotted in Fig. 3.48(a) and Fig. 3.51(a). The corresponding longitudinal impedance spectrum of the kicker is plotted in Fig. 3.52. As compared to the previous impedance spectrum, the impedance peaks are much higher and sharp. The impedance peak corresponding to the fundamental cavity mode appears at 3.19 GHz which compares well with the eigenmode analysis results. Impedance peaks at 1.77 GHz, 2.07 GHz and 2.488 GHz appear in the impedance spectra, which were not present in the impedance spectra with the coaxial ports matched.

3.6.3.3 Wake computations with off-axis beam

To compute the transverse kick parameters and impedances, the transverse wake components are required. This requires excitation of the cavity with an off-axis beam. For these computations, the method described in section 3.4.2 has been used. A beam with 2 mm offset in the y-direction has been used as the excitation source, while the other parameters of the beam were same as before. Fig. 3.53 shows the longitudinal and transverse components of the wake potential normalized to the beam offset along the bunch coordinate. It may be noted here that for transverse wake computations, all the coaxial ports have been terminated with matched terminations. The longitudi-

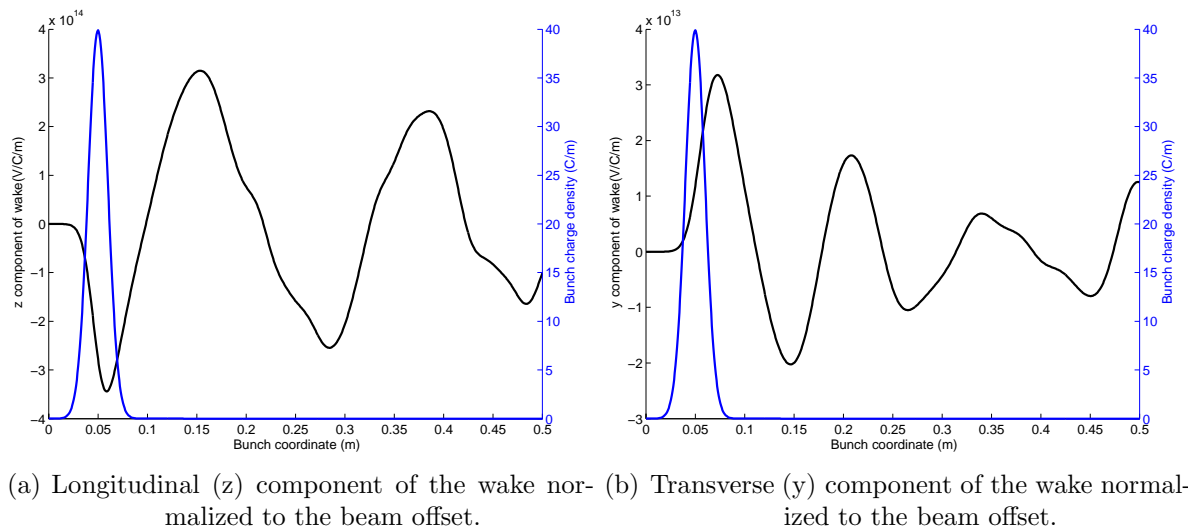
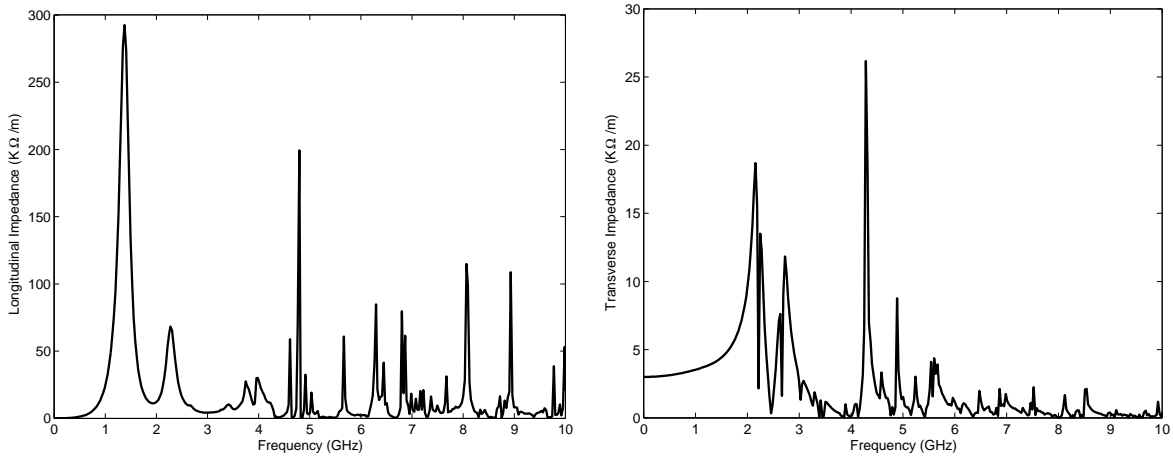


Figure 3.53: Longitudinal and transverse component of the wake normalized to the beam offset for the PETRA III feedback cavity.

3. Wake Computations and Related Analysis for PETRA III

nal and transverse impedance normalized to the beam offset is shown in Fig. 3.54. In the longitudinal impedance spectra some impedance peaks are visible at the frequencies very close to the resonant frequencies of the first dipole mode of the cavity. The longitudinal loss parameter and the $k(1)$ parameter for the transverse kick parameter computed according to the equations 3.4,3.5 for the 2 mm offset beam comes out to be -4.7400×10^{11} V/C and $1.7195e \times 10^{13}$ V/(C m), respectively. The corresponding transverse kick parameter computed according to the equation 3.6 normalized to the beam offset is 1.3150×10^{13} V/(C m). The different loss and kick parameters for the feedback cavity are summarized in the Table 3.10.



(a) Longitudinal (z) impedance normalized to the (b) Transverse (y) impedance normalized to the beam offset.

Figure 3.54: Longitudinal and transverse impedances normalized to the beam offset for the PETRA III feedback cavity.

Longitudinal loss parameter [V/C]	$k(1)$ parameter [V/(C m)]	Transverse kick parameter [V/(C m)]
-4.6997×10^{11}	1.7489×10^{13}	n.a.
-4.7400×10^{11} (offset=2.0 mm)	$1.7195e \times 10^{13}$ (offset=2.0 mm)	1.3150×10^{13}

Table 3.10: The loss and kick parameters for the PETRA III longitudinal feedback cavity with nose cones.

3.6.3.4 Shunt impedances

For the shunt impedance computations, the MAFIA T3 module has been used [98, 99]. A Gaussian beam suitable to excite the feedback cavity in the operating frequency

3.6 Simulation results for PETRA III longitudinal feedback cavity

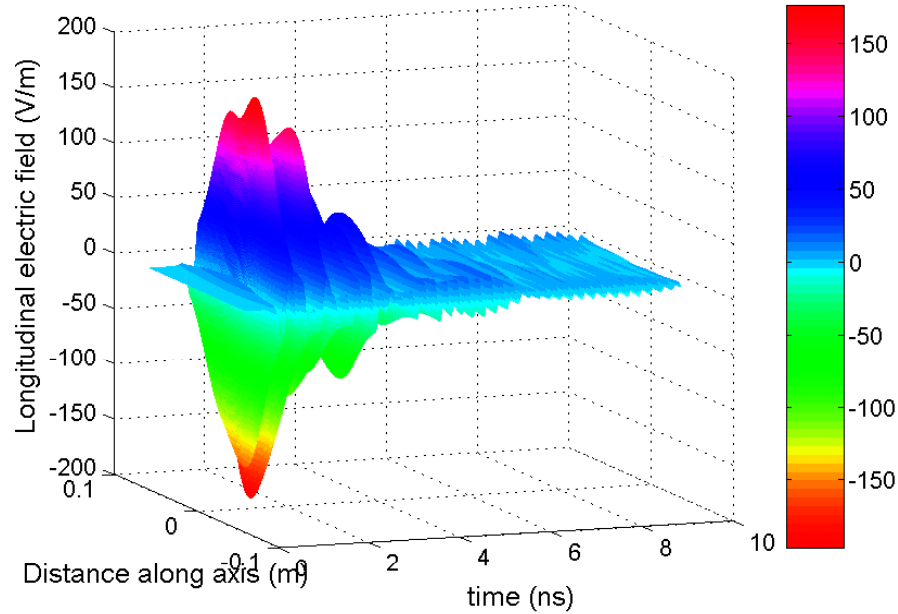


Figure 3.55: Variation of the longitudinal electric field along the feedback cavity axis with time.

band has been used as the excitation signal. The excitation signal has been fed to the cavity through one of the coaxial ports. The correction signal to the beam is to be fed through one of the coaxial ports. Therefore, it is of interest to study the variation of the electric field along the cavity axis when a coaxial excitation is used. Fig. 3.55 shows the variation of the longitudinal electric field along the cavity axis with time.

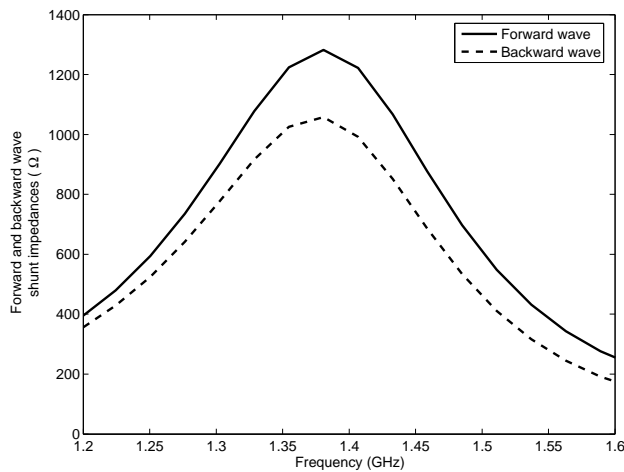


Figure 3.56: Forward and backward wave shunt impedances for the feedback cavity with the nose cones.

3. Wake Computations and Related Analysis for PETRA III

In MAFIA, the wake integration monitor computes the integral according to equations 3.2 and 3.3. The second part of the integral ($c \mathbf{e}_z \times \mathbf{B}$) does not contribute to the longitudinal component, because the orientation of this term lies in the transverse plane. Therefore, a wakefield monitor can be used to compute the accelerating voltage (V_{acc}) due to an excitation through a coaxial port of the cavity. In our case, we have considered the particle to be on axis, so the wakefield monitor has been set at $x = 0$, $y = 0$. The waveguide ports at both the ends of the feedback cavity along with the coaxial ports have been terminated with their corresponding wave impedances. All the outgoing wave amplitudes have been recorded at the coaxial ports. The exciting signal is a Gaussian pulse through the coaxial port 1 (near to the minimum of the distance axis). Two sets of computation runs have been done, one for the forward wave case and the other one is for the backward wave case. For the forward wave case, the excitation signal is fed through the coaxial waveguide ports 1 (one of the upstream couplers), while keeping the other two coaxial ports matched. It may be noted here that for the structures lacking symmetry (e.g. in case of a cavity with non-cylindrical beam pipes), all the upstream couplers should be simultaneously used for the excitations. Alternatively, the average of the results corresponding to individual excitations through the coaxial ports can also be taken. After obtaining the time domain data, a Discrete Fourier transform is used to transform them into the frequency domain. The shunt impedance (R_{shunt}) is computed according to the equation,

$$R_{shunt} = \frac{|V_{acc}|^2}{2P_{in}} \quad (3.25)$$

where P_{in} is the input power fed into the cavity through the coaxial ports. The advantage of this method is one can obtain the variation of the shunt impedance within the

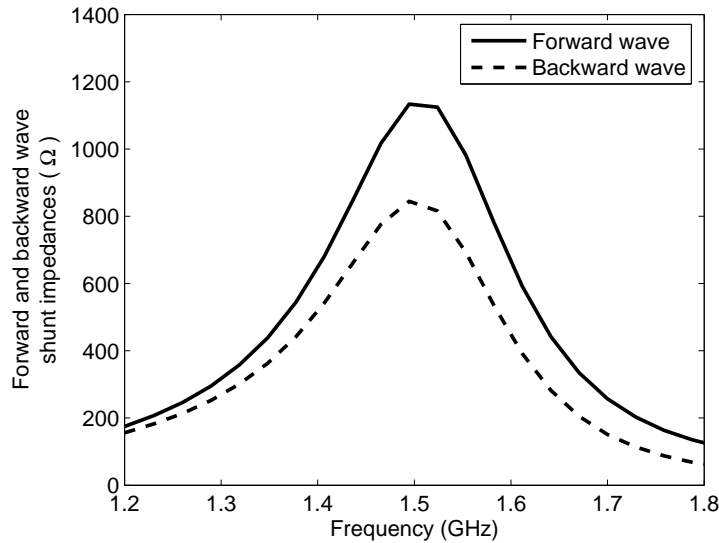


Figure 3.57: Forward and backward wave shunt impedances for the feedback cavity without the nose cones.

3.6 Simulation results for PETRA III longitudinal feedback cavity

frequency range of interest from a single simulation run.

Fig. 3.56 shows the variations of computed forward and backward wave shunt impedances for the feedback cavity. From the plot, it can be noticed that the maximum of the shunt impedances occur around 1.38 GHz with a maximum value of 1134 Ω (for the forward wave). Both the forward and the backward wave shunt impedances are a bit lower than those of ELTTRA/SLS kicker [100]. Another interesting point is to study the effect of the nose cones on the shunt impedances. To appraise this point, the same computations have been carried out for the feedback cavity without the nose cones. The computed shunt impedances are shown in Fig. 3.57. From Figs. 3.56 and 3.57, it is clear that the inclusion of the nose cones have improved the shunt impedances about 13%. The frequency corresponding to the peak of the shunt impedance have also been increased (1.495 GHz) compared to that with the nose cones.

Chapter 4

Analysis of an Ultra-wideband Antenna

4.1 Prologue

Microwave or radio frequency antennas are essential parts of many communication systems. The basic purpose of the antennas is to receive and transmit electromagnetic signals efficiently. Numerous types of RF antennas are present, depending upon their applications, working principles, operating frequency range etc. In this section the modeling and analysis of an ultra-wideband RF antenna using the commercial CEM tool MWST is presented.

Ultra-wideband characteristics of RF antennas are desirable for various applications like subsurface imaging, high power pulse transmissions etc. As an example, the case of subsurface imaging - popularly known as ground penetrating RADAR applications can be considered. The ultra-wideband antenna characteristics can lead to a significant increase in the spatial resolution in the direction normal to the surface of the ground. This is essential for the detection of the objects buried underground. The preferable features of such antenna systems include low cost, simple fabrication, compactness and portability. In present days, usage of wireless networks and various multimedia applications are ever growing. This constantly calls for development of antenna systems in various frequency bands, as different frequency bands are generally used for the individual applications. A single antenna with optimal performance over a wide frequency band can serve as the transmitting or receiving device for a number of wireless applications. This will eventually help to significantly reduce the complexity and cost of the corresponding system.

It is known from the literature that the broadband characteristics of an antenna can be achieved by minimizing the reflections from the antenna edges and transitions. In this way, a well-matched transformer between the antenna feed and the free space over a wide frequency band [101] can be achieved. Numerous two and three dimensional geometrical structures, e.g. the bow-tie antenna [102], the TEM horns [103], Vivaldi antennas [104], have been suggested in the literature to achieve the broad band frequency independent

4. Analysis of an Ultra-wideband Antenna

antenna characteristics. The antenna under analysis can be categorized as a specially tapered TEM horn antenna. The study initiated based on the design reported in [105]. The antenna under analysis is very wide band, having a moderate gain over the whole frequency band. It is compact, low cost and easy to fabricate - making it suitable for portable applications.

The main objectives to analyze the antenna are to investigate its working principle, identify the crucial parameters influencing the antenna characteristics and use these analysis to improve and customize the antenna for specific applications. It may be noted here that as the antenna shape is very complex, it is almost impossible to analyze it analytically. Due to the same reason, its modeling inside a commercial CEM tool was a problem itself. This modeling problem has been solved with the help of another well-known general purpose computational tool, MATLAB [61].

4.2 Theoretical Basics

4.2.1 Radiation field regions of an antenna

The radiation field region of an antenna can be subdivided into some regions, depending upon the characteristics of the propagating field. In general this region is broadly divided into two regions, namely, the near-field and the far-field region. The near field region can further be sub-divided into two regions - the reactive near field and the radiating near field region [101].

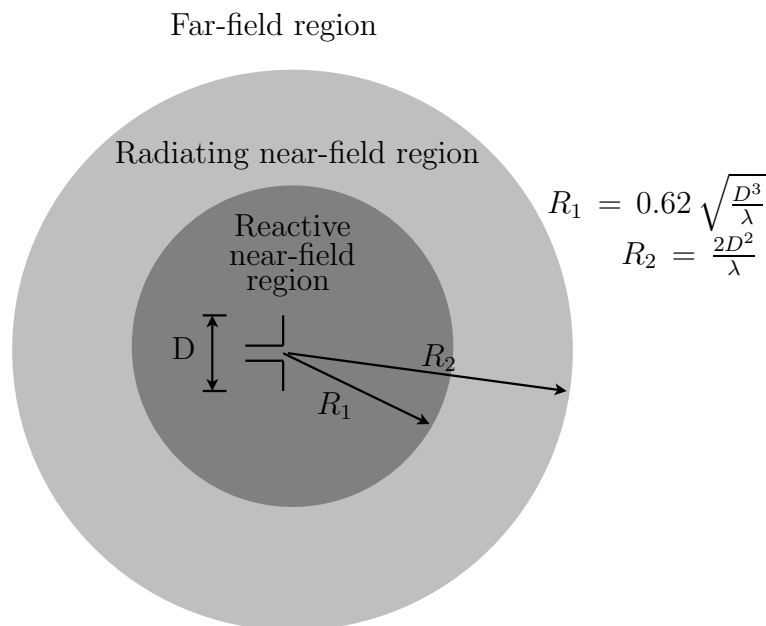


Figure 4.1: The field regions of an antenna [101].

Reactive near-field region: This is the immediately surrounding region of the antenna where the non radiating fields (reactive fields) predominate. For an antenna with electrically large aperture dimension (D), the boundary of this region is taken to be at a distance $R < 0.62\sqrt{\frac{D^3}{\lambda}}$, λ being the wavelength.

Radiating near-field region: In this region the radiation fields predominate and the angular distribution of the field is dependent upon the distance from the antenna. A radiating near-field exists if the antenna under consideration is sufficiently large so that an interference occurs between the radiations from different parts of the antenna. Due to the similarity to the optical terminology, this region is sometimes called as the Fresnel region. The lower boundary of this region is usually considered at a distance $R \geq 0.62\sqrt{\frac{D^3}{\lambda}}$ and the upper boundary at $R < \frac{2D^2}{\lambda}$.

Far-field region: The far-field region of an antenna is located sufficiently far from the antenna so that only the radiating field components are significant. In this region, the angular distribution of the fields and power are independent of the distance from the antenna. The electric and magnetic fields decay inversely with the distance from the antenna and the power density decays as the inverse squared of the distance. The far field region is commonly taken to exist at distances greater than $\frac{2D^2}{\lambda}$ from the antenna. The far-field region is also termed as the Fraunhofer region, for the analogy to the optical terminology. All the radiation field regions of antenna is shown schematically in the Fig. 4.1.

4.2.2 Definitions of different antenna parameters

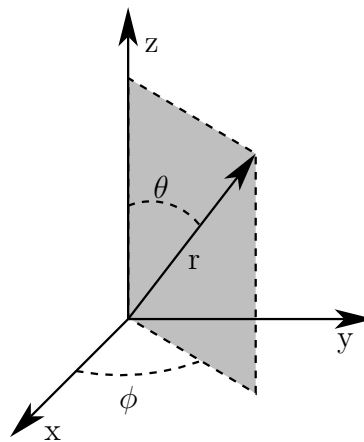


Figure 4.2: A typical spherical coordinate system for characterizing radiation patterns of an antenna.

4. Analysis of an Ultra-wideband Antenna

Radiation pattern: The radiation properties of an antenna are generally represented graphically as functions of convenient space coordinates, usually in the far-field region. The radiation properties which are mostly used include the radiation intensity, radiation field strength, polarization etc. Usually, the spherical coordinate system is used for radiation pattern evaluation. A typical coordinate system to represent antenna characteristics is shown in Fig. 4.2. The most important radiation characteristic of an antenna is the three dimensional spatial distribution of the energy radiated by it. This is usually expressed as a function of angle along a circle centered at the antenna position.

Principle radiation pattern: Performances of a linearly polarized antenna are generally described by the E- and H-plane radiation patterns which are termed as the principle patterns of the antenna. The E-plane of an antenna is defined as the plane containing the electric field vector and the direction of maximum radiation. Similarly the H-plane of an antenna is defined as the plane containing the magnetic field and the direction of maximum radiation.

Radiation pattern lobes: In general, the radiation patterns of real life antennas are not uniformly distributed over space. So, strong radiation regions are followed by regions with weak radiation characteristics. These relatively strong regions of radiation patterns are termed as the radiation pattern lobes. The radiation lobes can be classified into the main lobe, side lobes, back lobe etc. depending upon their characteristics and relative directions.

Isotropic antenna: An isotropic antenna is a radiator which radiates uniformly in all the directions. Although such an isotropic radiator is purely hypothetical, it is often used in the antenna literature as a reference to compare performances of other antennas. The radiated power density (W_{r0}) of an ideal radiator at a radial distance r is given by,

$$\mathbf{W}_{r0} = \hat{a}_r \left(\frac{P_{rad}}{4\pi r^2} \right) \quad (4.1)$$

where, \hat{a}_r is the unit vector along the radial direction and P_{rad} is the total power radiated by the antenna.

Radiation intensity: The radiation intensity of an antenna in a given direction is the radiated power in that direction per unit solid angle. The radiation intensity (U_0) of an isotropic radiator is given by,

$$U_0 = \frac{P_{rad}}{4\pi} \quad (4.2)$$

Here, it may be mentioned that 4π is the solid angle corresponding to a full sphere.

Directive gain and directivity: The directive gain in a particular direction of an antenna is defined as the ratio of its radiation intensity in that direction to the radiation intensity of an isotropic antenna. Here, it has been assumed that the isotropic antenna and the antenna under consideration have been fed with equal amounts of power. The value of maximum directive gain is called the directivity of the antenna. If the directive gain of an antenna with a radiation intensity U along a particular direction is denoted by D_g , then mathematically,

$$D_g = \frac{U}{U_0} = \frac{4\pi U}{P_{rad}} \quad (4.3)$$

$$= 4\pi \frac{\text{radiated power per unit solid angle}}{\text{total radiated power}} \quad (4.4)$$

$$D_0 = \frac{U_{max}}{U_0} = \frac{4\pi U_{max}}{P_{rad}} \quad (4.5)$$

Here, D_0 denotes the directivity of the antenna and U_{max} is the maximum radiation intensity of the antenna.

Total efficiency: The total antenna efficiency is defined as the ratio of radiated power to input power fed to the antenna. The total efficiency includes the effects of losses due to the mismatch between the transmission line and antenna and the ohmic losses. The total efficiency can be expressed as,

$$e_t = \frac{P_{rad}}{P_{in}} \quad (4.6)$$

$$= \left(\frac{P_{rad}}{P_{acpt}} \right) \left(\frac{P_{acpt}}{P_{in}} \right) \quad (4.7)$$

$$= e_{rad} e_{refl} \quad (4.8)$$

Here, P_{rad} denotes total radiated power by the antenna, P_{in} denotes total input power to the antenna, P_{acpt} denotes the power accepted by the antenna. The quantities $e_{rad} = \frac{P_{rad}}{P_{acpt}}$ and $e_{refl} = \frac{P_{acpt}}{P_{in}}$ are termed as the radiation efficiency and reflection efficiency of the antenna respectively.

Gain: Gain is another important parameter related to an antenna. It is closely related to the directivity of an antenna and takes its radiation efficiency into account. The gain of an antenna along a particular direction is defined as 4π times the ratio of the radiation intensity in that direction to the net power accepted by the antenna. Mathematically, this can be expressed as,

$$G = 4\pi \frac{\text{radiated power per unit solid angle}}{\text{accepted input power}} \quad (4.9)$$

$$= \frac{4\pi U}{P_{in}} \quad (4.10)$$

Here, P_{in} is the input power accepted by the antenna.

4. Analysis of an Ultra-wideband Antenna

4.3 Geometry of the antenna under analysis

The antenna under analysis is made of a thin metallic sheet with a SMA connector used for feeding. The first part of the antenna consists of a loop formed by the metallic sheet and the second part consists of a TEM horn. The TEM horn is formed by extending the loop further and flaring it in the opposite direction of the loop. A schematic diagram of the individual parts of the antenna is shown in Fig. 4.3. The shape of the metallic sheet and the schematic drawing of the SMA connector used to feed the antenna can be seen in the figure. The tapered portion 1a along with the straight portion 1b of the metallic sheet are bent to form a loop. The straight portion 1c is flared outwards to form the shape of a horn antenna. The small hole h1 is used to connect the metal pin 2a of the SMA connector with the metal sheet. The Teflon isolation (of the SMA connector) 2b fits exactly into the hole h2. The flange 2c of the SMA connector is soldered to the metal sheet at the connections 1b-1c. In the case of a 50 Ohm feeding line the hole h2 has a diameter of 4.1 mm, which is exactly the outer dimension of the dielectric isolation of the coaxial line. The cross section of the antenna together with the feed at the symmetric plane is shown in Fig. 4.4. The input impedance of the antenna is the same as that of the feeding line. In our case, the normal 50 Ohm coaxial feed has been used as the feeding line.

4.4 Modeling of the antenna

The modeling and simulation of the antenna has been done with the help of MWST and MATLAB. The antenna geometry is too complicated to model straightforwardly using the shape definition tools available inside MWST. For this reason, the general purpose mathematical software tool MATLAB has been used to create the antenna structure inside MWST. The parameters controlling the antenna geometry, different material parameters, simulation parameters etc. are given as inputs of the MATLAB program. The MATLAB program then creates the antenna geometry inside MWST according to the input parameters. The block diagram in Fig. 4.5 shows the working of the program.

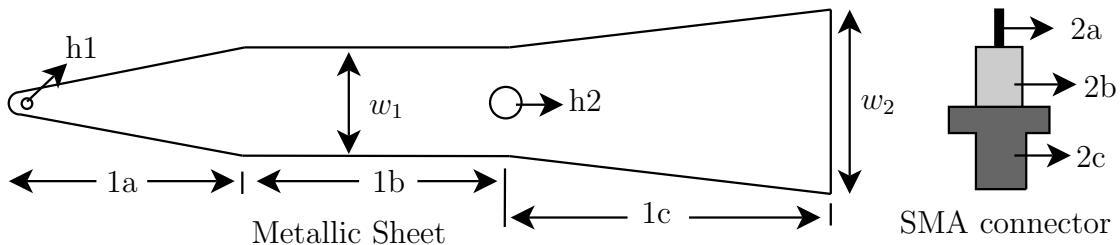


Figure 4.3: Schematic diagram of the metallic sheet used to fabricate the antenna and the 50 Ohm SMA connector used for the feed.

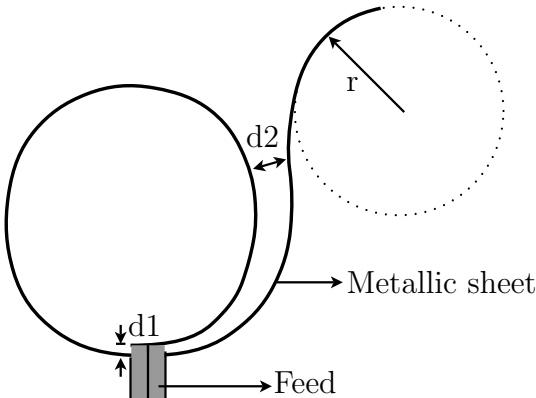


Figure 4.4: Schematic diagram of the antenna cross-section at the symmetry plane.

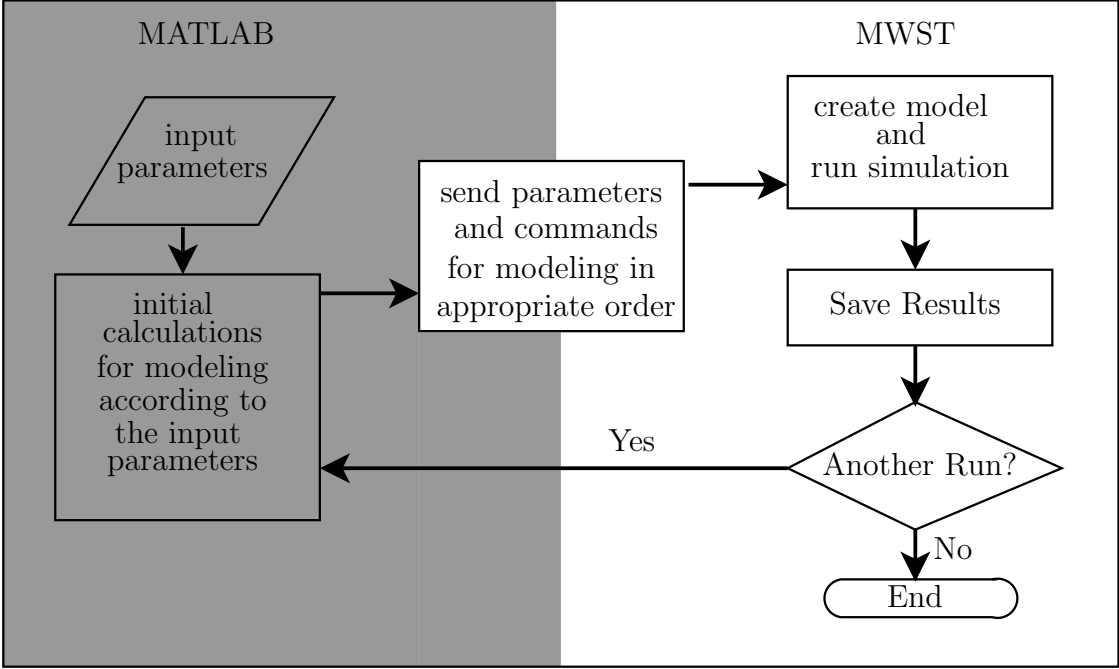


Figure 4.5: Schematic diagram of the antenna cross-section at the symmetry plane.

To create the antenna structure inside Microwave Studio, at first the rectangular cross-sections of the metallic sheet shown in Fig. 4.3 are created according to the profile of the antenna. This has been done using the polygon creation tool of microwave studio. Afterwards, these rectangular polygon curves have been joined together and the “loft” tool has been used to create the metallic sheet. At the next step, the coaxial feed of the antenna has been added using the standard shape creation tools of MWST. All these steps of antenna modeling have been controlled through the MATLAB program. After completely specifying the antenna geometry and the simulation parameters like the

4. Analysis of an Ultra-wideband Antenna

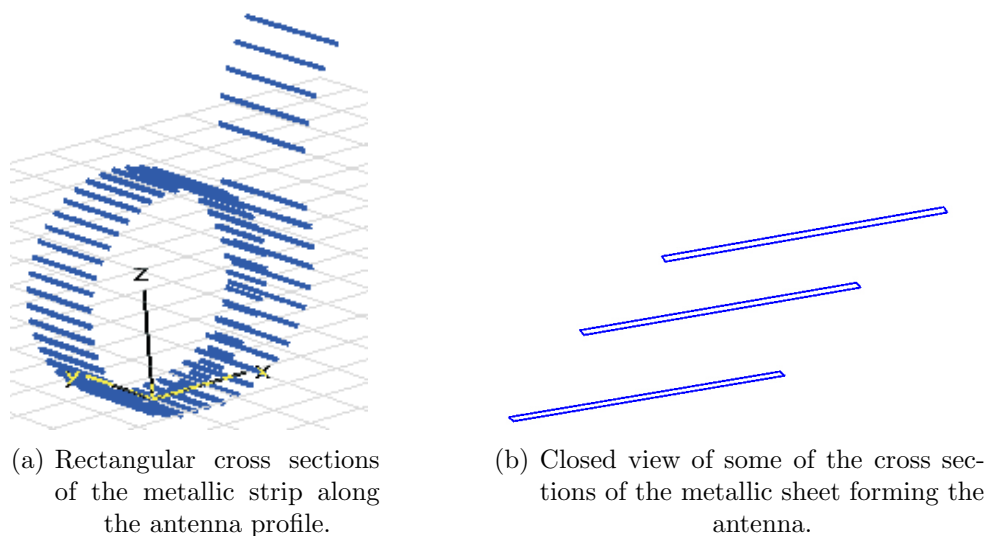


Figure 4.6: The metallic cross sections created to define the antenna geometry.

frequency range, the number of mesh lines per wavelength to be used, etc. are specified the actual simulation is started. In case of a set of parametric studies, the results after each simulation run are saved before the complete simulation circle for another set is repeated.

The antenna under consideration can be studied with respect to many degrees of freedom. But for our investigations, only a few of them have been considered. The main parameters which have been used to control the shape of the antenna are the height of the feed, the radius of the outward flaring, the distance between the loop and the flared part of the antenna. These parameters have been indicated in Fig. 4.4. The overall length of the metallic strip, hence the overall size of the antenna can also be considered as a parameter for the analysis.

4.5 Simulation and measurement results

4.5.1 Excitation

The complete antenna model along with the coordinate system used for simulations is shown in Fig. 4.7(a). The automatic meshing scheme has been used for the simulations. Under this meshing scheme, the meshing is done according to the small details of the modeled geometry. The meshing details for the antenna at a yz -plane are shown in Fig. 4.7(b). The non-uniform mesh distribution according to the antenna geometry can be noticed in Fig. 4.7(b). As the antenna is symmetric with respect to the xz -plane (Fig. 4.7(a)), a magnetic wall symmetry is used for the simulations - saving half of the computational efforts.

The excitation of the antenna is provided through a waveguide port defined at the

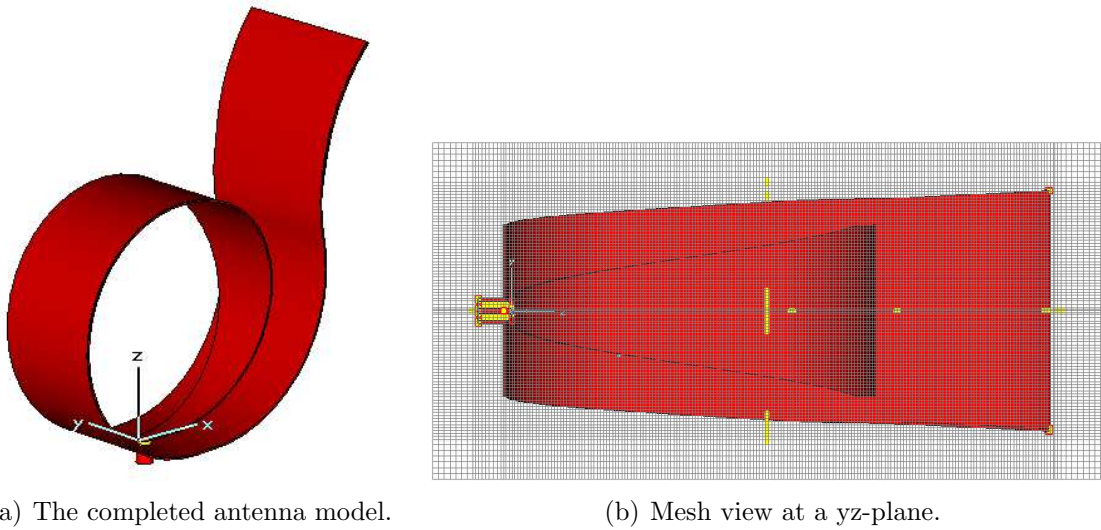


Figure 4.7: The antenna model along with the relevant coordinate system and its meshing details at a yz -plane.

coaxial SMA feed. The computed impedance of the port comes out to be very near to the actual one, i.e. 50 Ohm. This provides a cross-check for the actual excitation port and that used for simulation. The waveguide port and details of the electric field distribution of the TEM mode (waveguide port mode) used for the excitation are shown in Fig. 4.8.

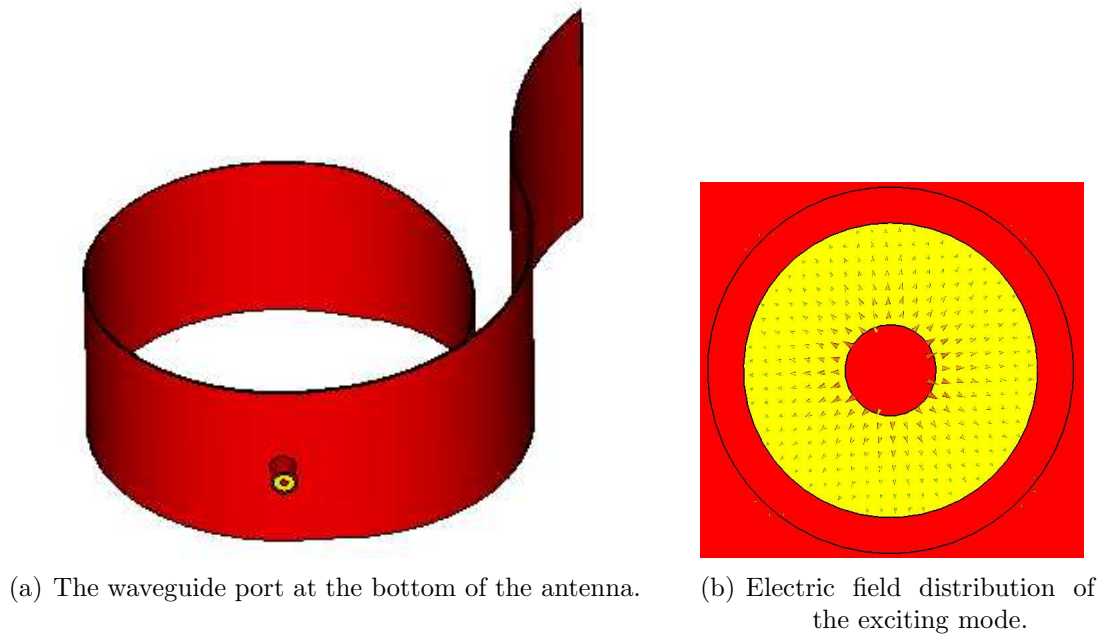


Figure 4.8: The excitation port and electric field distribution of the exciting mode.

4. Analysis of an Ultra-wideband Antenna

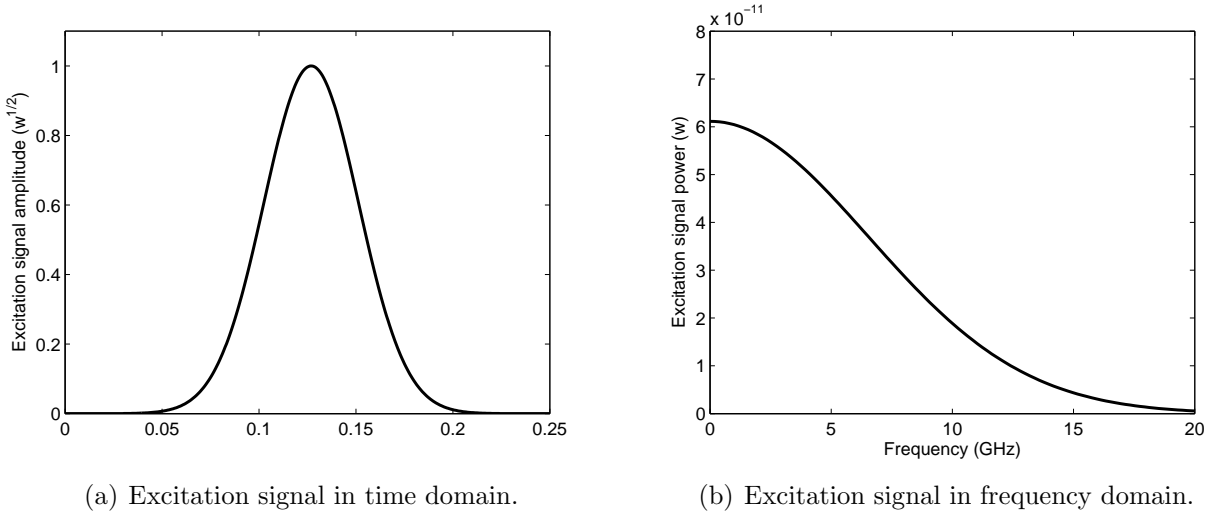


Figure 4.9: The excitation signal suitable for the frequency range 0-18 GHz in time and frequency domain.

A typical Gaussian excitation suitable to analyze the antenna response in the frequency range of 0-18 GHz is shown in Fig. 4.9 in the time and frequency domain. The computation domains for all the transient analysis have been terminated with Perfectly Matched Layer (PML) boundaries, using four PML layers with reflection coefficients 0.0001.

4.5.2 Convergence studies

To ensure the consistency of the simulations, at first convergence studies have been done to find out the optimal distance of the bounding box from the structure and the optimal number of mesh lines per wavelengths for a reasonable accuracy of the solution. The appropriate distance between the PML layers terminating the computation domain and the device under analysis still remains as a debatable issue. For this reason a convergence test on the return loss of the antenna has been performed. The distance of the bounding box from the antenna in all three directions have been varied in terms of the wavelength at mid-frequency (λ) and the corresponding return losses have been computed. All the other simulation parameters have been kept unaltered. The simulation results are shown in Fig. 4.10. From the figure it is clear that although there is a small difference in the lower frequency range (at the first minima) for different bounding box distances, the results converge for the distance of bounding box at $\lambda/8$. No notable differences in the radiation patterns have been marked for different bounding box distances. It may be noted here that the number of mesh cells for these three cases are 4892514, 5657919 and 7404129, respectively. In order to keep the computation efforts minimum, the distance of the bounding box is taken as $\lambda/8$ for the simulations. The convergence study for the optimum mesh resolution has been carried out at the next step. The return losses of

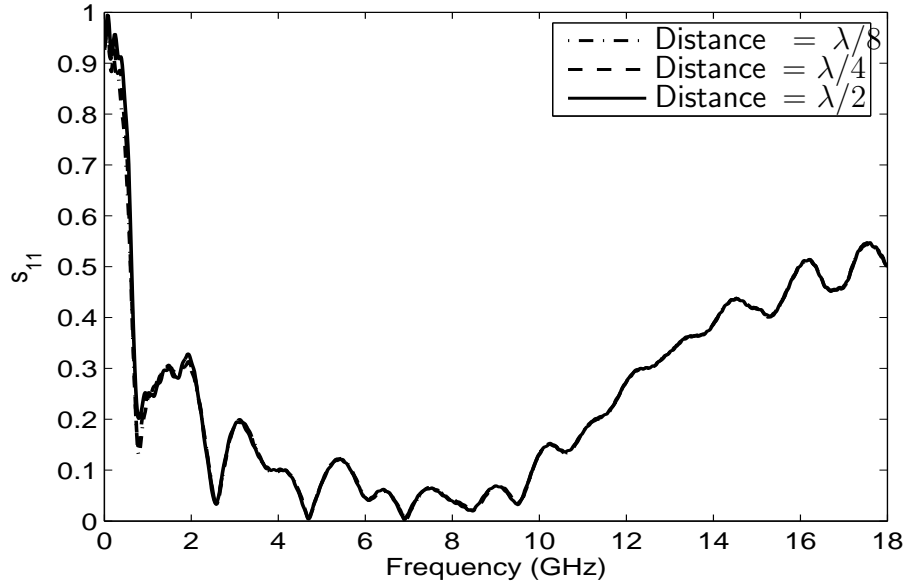


Figure 4.10: Computed return loss vs frequency for different distances between the bounding box and antenna.

the antenna have been computed for different mesh resolutions. The comparison of the return losses with mesh resolutions of 10-lines, 20-lines and 30-lines per wavelength (at 18 GHz) are shown in Fig. 4.11. The corresponding number of mesh-cells and cpu time for the computations are summarized in Table 4.1. It can be seen from Fig. 4.11 that the mesh resolution of 10 lines per wavelength is not enough to reliably determine the antenna characteristics, although the computational efforts are minimum in this case. Although, there is a small deviation between the results of 20 lines per wavelength and 30-lines per wavelength at the higher frequencies, the position of the minimas and the trend of the curves match quite well. As the resolution of 30 lines per wavelength needs more than three times the computational time of that with 20 lines per wavelength without a very big difference in accuracy, the mesh resolution has been taken as 20 lines per wavelength for the simulations.

Number of lines per wavelength	Number of mesh cells	CPU time for computation
10	795150	0 h, 41 m, 51 s
20	4892514	6 h, 5 m, 7 s
30	16434198	21 h, 10 m, 39 s

Table 4.1: Number of mesh-cells and solver times (on a computer with 64 bit, 2.39 GHz AMD Opteron processor).

4. Analysis of an Ultra-wideband Antenna

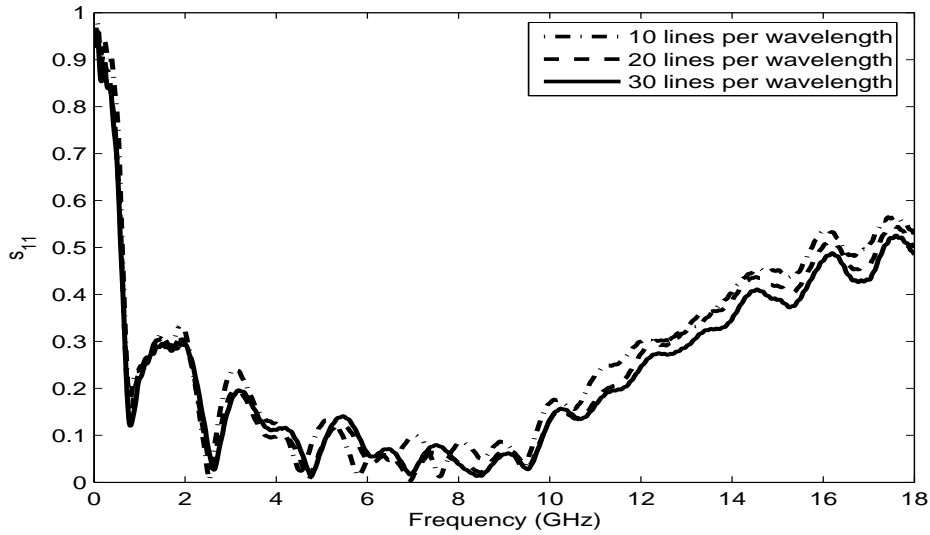


Figure 4.11: Computed return loss vs frequency for different mesh resolutions.

4.5.3 Parametric studies

To understand the influences of various antenna parameters on its performances, parametric studies have been done with the optimum simulation parameters from the convergence studies. The return loss and the radiation patterns at various frequencies have been computed for different values of d_1 , d_2 and r (Fig. 4.4) separately.

Fig. 4.12 shows the variation of the antenna return loss with frequency for different

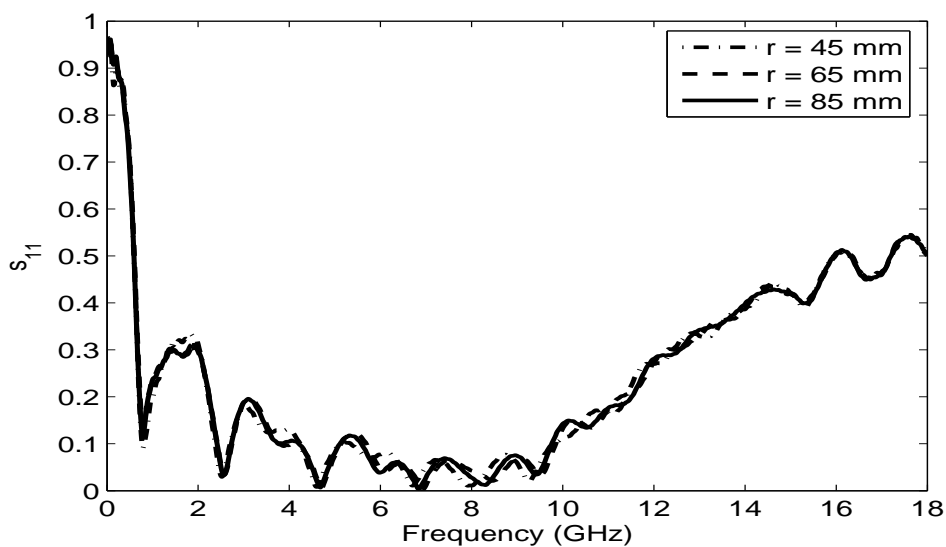


Figure 4.12: Computed return loss vs frequency for different values of 'r'.

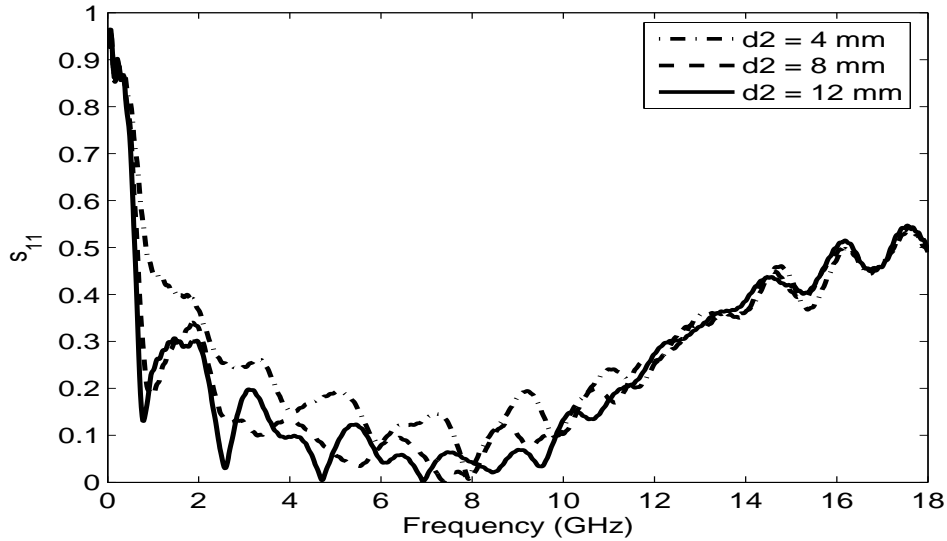
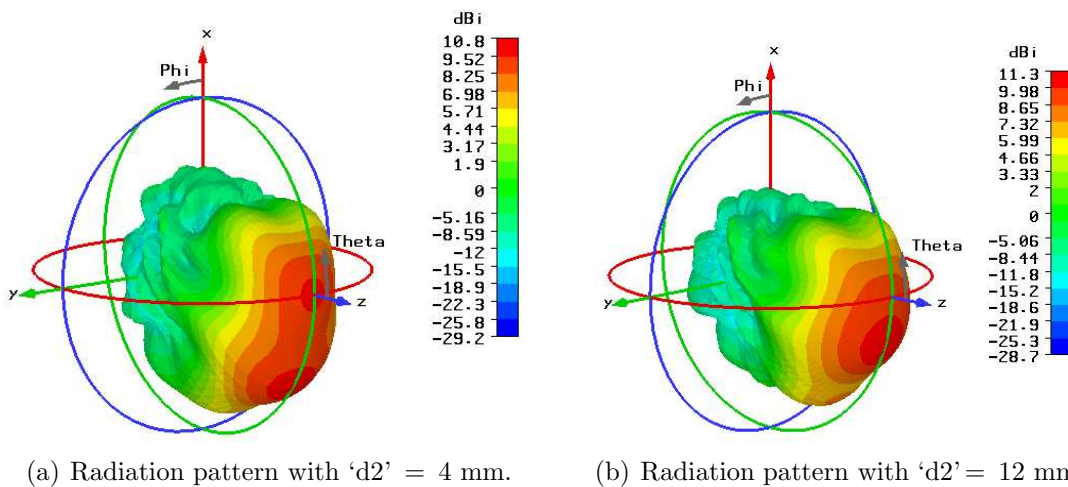


Figure 4.13: Computed return loss vs frequency for different values of ‘d2’.

values of the radius of flaring (‘r’). As can be seen from the figure, the radius of flaring does not influence the antenna return loss very much. Also no significant difference in the radiation pattern has been found for antennas with different radius of flaring (r).

The second parameter used for the parametric studies was the distance of the flaring, ‘d2’. The comparison of the antenna return loss with different ‘d2’ values is shown in Fig. 4.13. It may be noticed from the figure that ‘d2’ influences the antenna return loss in the lower frequencies. In the higher frequencies (above 12 GHz), the influences of ‘d2’ on the antenna return loss is not so significant. However, a considerable influence on the radiation patterns in the higher frequency range (above 8 GHz) have been found. The



(a) Radiation pattern with ‘d2’ = 4 mm.

(b) Radiation pattern with ‘d2’ = 12 mm.

Figure 4.14: Radiation pattern at 8.0 GHz for different distance of flaring (‘d2’).

4. Analysis of an Ultra-wideband Antenna

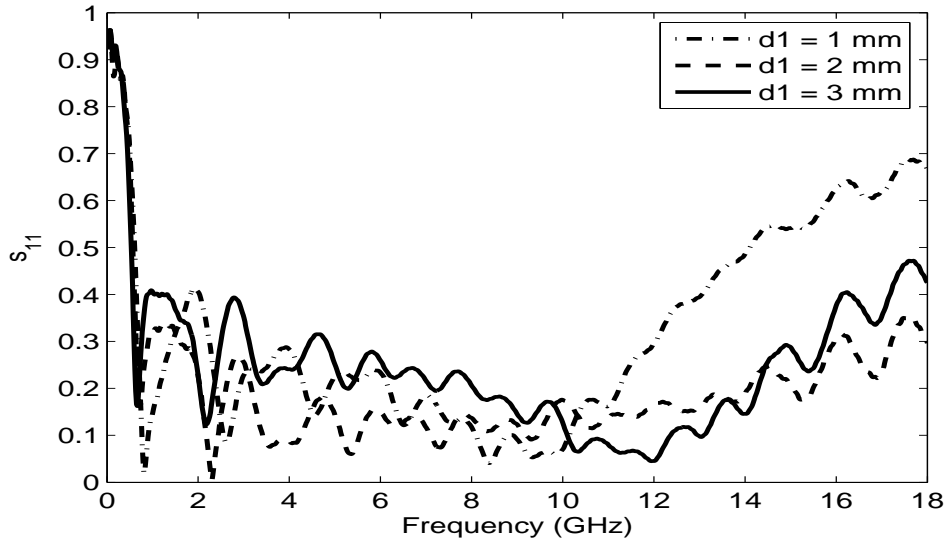
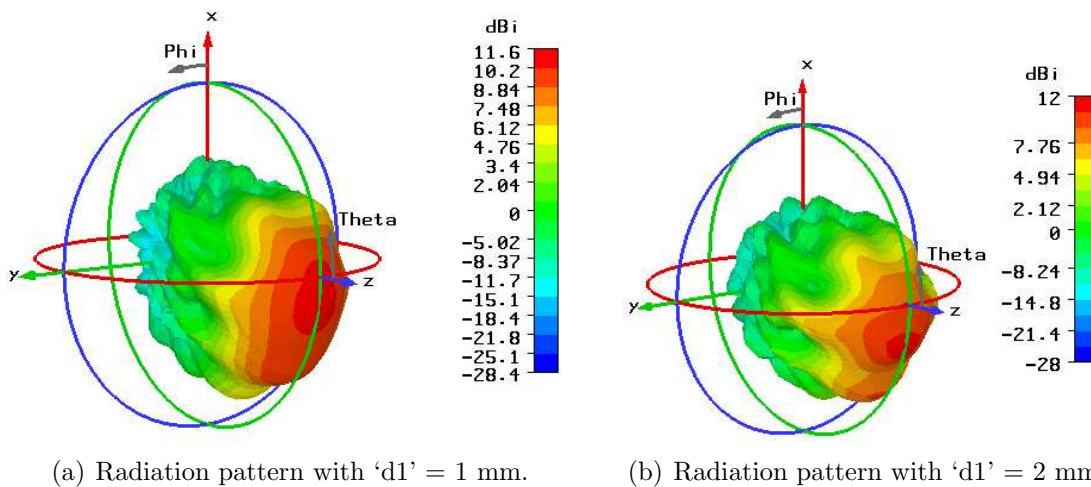


Figure 4.15: Computed return loss vs frequency for different values of ‘d1’.

three dimensional plots of the antenna directivities with ‘d2’ values 4 mm and 12 mm are shown in Figs. 4.14(a) and 4.14(b), respectively. As seen in the figure, a split in the beam has been observed for $d_2 = 4$ mm.

The influence of the height of the feed (d_1) on the antenna return loss has been investigated in the next step. The return loss of the antenna has been plotted for different ‘ d_1 ’ values in Fig. 4.15. From Fig. 4.15, it is clear that there is a very strong influence of the height of the feed on the antenna performance - even a very small change in the feed height (in the order of 1 mm) drastically changes the antenna return loss. Lowering of the feed height tends to improve the antenna characteristics



(a) Radiation pattern with ‘d1’ = 1 mm.

(b) Radiation pattern with ‘d1’ = 2 mm.

Figure 4.16: Radiation pattern at 10.0 GHz for different feed heights (‘d1’).

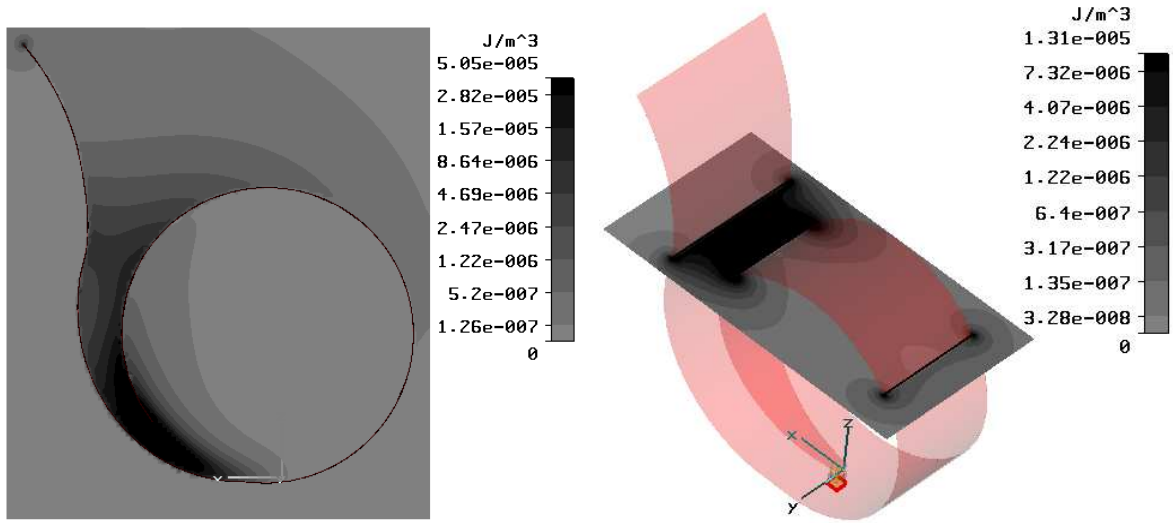


Figure 4.17: Peak electric energy density plotted at two planes.

in the lower frequencies, at the same time degrading the characteristics at the higher frequencies. The radiation characteristics of the antenna is also influenced by the feed height. Fig. 4.16 shows the antenna radiation pattern at 10 GHz for two values of the feed height. It can be seen from the figure that with 1 mm feed height the beam is broad and it splits when the feed height is increased to 2 mm. With larger feed height, the beam tends to break at lower frequencies compared to that with shorter feed height.

The electric and magnetic energy densities provide important information about the energy distribution at various parts of the antenna. To investigate the distribution of the electric and magnetic energies at different frequencies, the peak electric and magnetic energy densities have been monitored. Figs. 4.17 and 4.18 show peak electric and magnetic energies at 2.4 GHz plotted at two planes. From the plot, it is clear that the electromagnetic energy is concentrated inside the region between the loop and the flared part. It may be noted here that logarithmic scale have been used for the field plots. Another notable phenomena is the high concentration of the fields at the antenna edges. The energy densities for other frequencies (till around 14 GHz) follow the same trend.

4.5.4 The effect of the loop

To study the effect of the loop on the antenna characteristics, it has been simulated without the loop as shown in Fig. 4.19(a). The comparison of the computed return loss with and without the loop is shown in Fig. 4.19(b). Comparing the antenna return losses with and without the loop, it can be seen that the loop improves the antenna return loss in the lower frequencies (around 1 GHz). This improvement is due to the fact that the loop minimizes the reflections from the edges in the yz -plane [Fig. 4.19(a)]. The idea that the loop acts as a magnetic dipole as suggested in [105] comes out to

4. Analysis of an Ultra-wideband Antenna

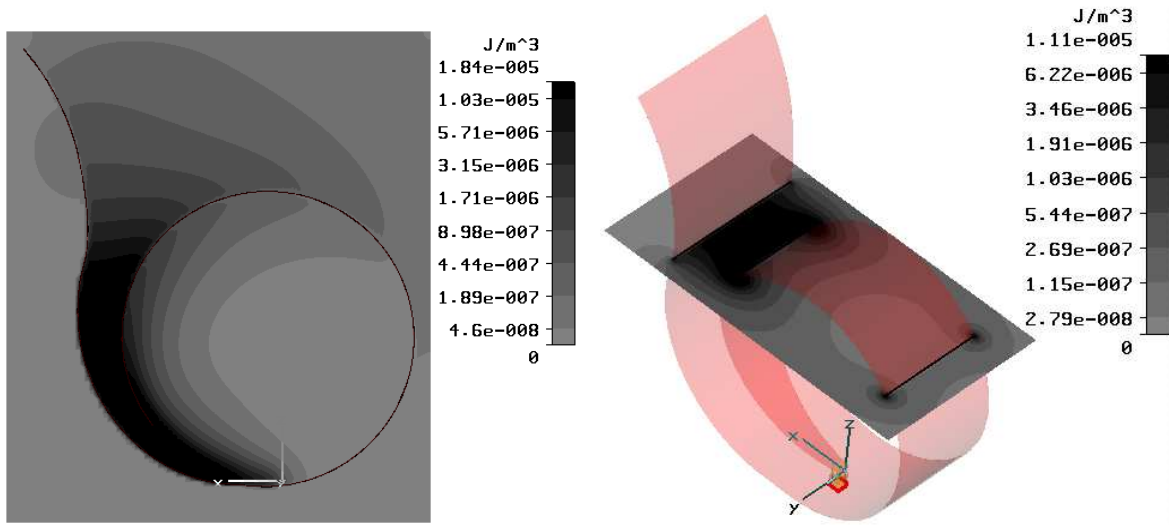
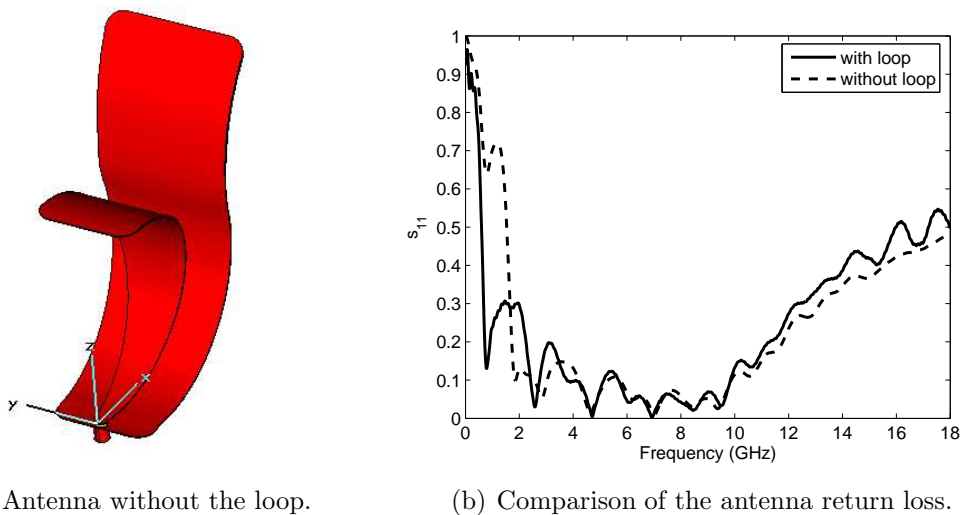


Figure 4.18: Peak magnetic energy density plotted at same planes of Fig. 4.17 .

be incorrect. The electric and magnetic fields and hence the energies remain confined inside the tapered region in the whole operating frequency band. A slight improvement of the antenna return loss in the higher frequency band (above 1.6 GHz) has been found without the loop. This may be due to the fact that the absence of the loop allows the unwanted fields to escape which leads eventually to a reduction of reflections.



(a) Antenna without the loop.

(b) Comparison of the antenna return loss.

Figure 4.19: The antenna without loop and comparison of the return loss with and without the loop.

The peak electric and magnetic energy densities at 2.4 GHz for the antenna without the loop are shown in Fig. 4.20. From the figure it can be seen that there are con-

4.5 Simulation and measurement results

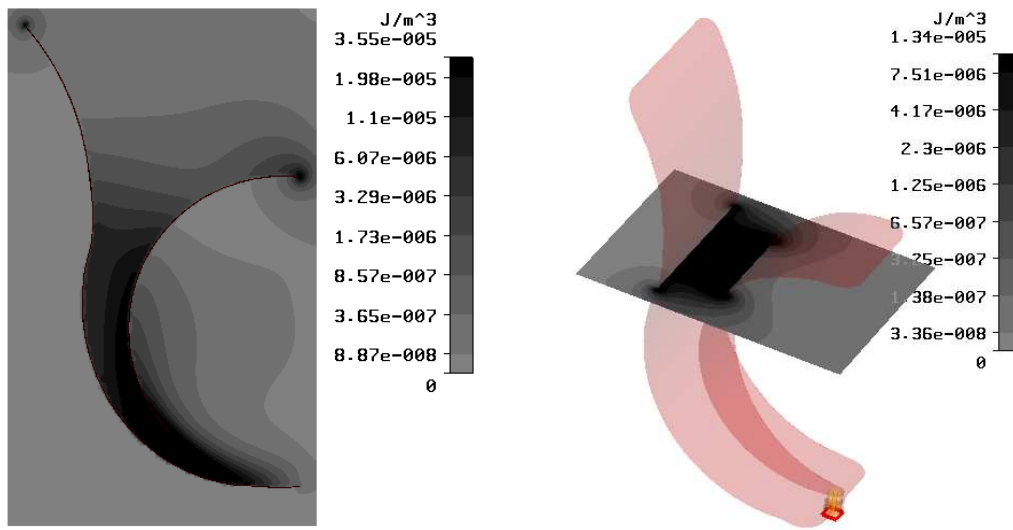
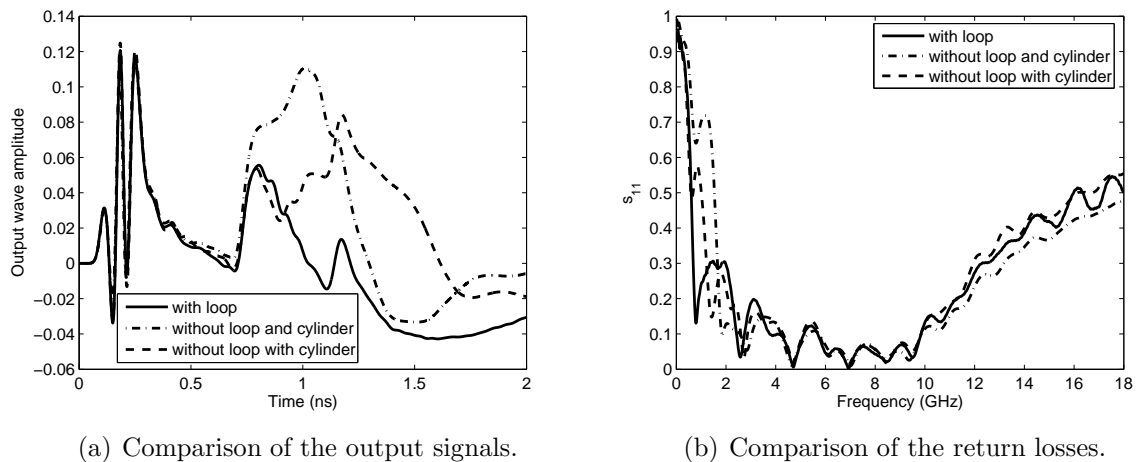


Figure 4.20: Peak electric energy densities inside the antenna at two different panes without the loop.

concentrations of electric energies at the edges of the antenna, specially the edge created by the omission of the loop. This concentration of the fields at the edge is larger at the lower frequencies (bellow 3 GHz approx.), which explains worsening of the antenna performance at lower frequencies without the loop. It is also clear form the figure that the electrical energy remains confined at the tapered region of the antenna, instead of the absence of the loop. The same trend has been found for the magnetic energy.

To investigate the effect of higher field concentrations at the edge of the antenna,



(a) Comparison of the output signals.

(b) Comparison of the return losses.

Figure 4.21: Comparison of the output signals and return losses with loop, without loop and without loop but with cylinder.

4. Analysis of an Ultra-wideband Antenna

simulations have been done with a metallic cylinder attached to the antenna edge. The comparison of the output wave amplitudes at the input port for the three cases - antenna with the loop, without the loop and without the loop but with a metallic cylinder is shown in Fig. 4.21(a). It may be noted that in all these three cases, the input pulse had same characteristics, with a maximum amplitude of 1. The comparison of the corresponding return losses can be seen in Fig. 4.21(b). From the plot of the output signal, it can be noticed that the initial reflections remains similar for all the three cases. This is expected, because the antenna geometry near the feed remains unaltered in all the three cases. The reflection peak around 0.8 ns is actually caused by the edge at the end of the flaring and is present in all three cases. It has been observed through simulations that the position of the reflections (around 1 ns and 1.18 ns) for the second and third case depend on the position where the loop has been cut. This suggests that these reflection peaks are caused by the reflections from the edge created by the absence of the loop. The total absence of this peak in the first case conforms this point. As can be seen from Fig. 4.21(a), the amount of reflection is decreased due to the addition of the cylinder at the edge. This minimization of the return loss has been translated to a betterment of the antenna return loss at can be noticed in Fig. 4.21(b).

4.5.5 Comparison between simulations and measurement

On the basis of earlier studies, an optimized version of the antenna has been designed. The simulations for the antenna suggests a very wide range of operation starting from around 800 MHz till 14 GHz. The simulated three dimensional radiation patterns of the antenna at different frequencies are shown in Fig. 4.23. One of the fabricated antenna prototype is shown in Fig. 4.22, mounted in the anechoic chamber for measurement. Comparison the simulated and measured return loss of the antenna have been shown in Fig. 4.24. From the figure, a significant deviation is noticed between the simulation



Figure 4.22: A fabricated prototype of the antenna.

4.5 Simulation and measurement results

results and the measurements. This deviation is most probably caused by the differences in the simulated and fabricated antenna geometry. The whole antenna, including the flared portion and the feed region - which have been found earlier to have very strong influences on the antenna performance, has been curved by hand. For this reason, although the antenna geometry is close to the simulated one, it is not fully identical to the fabricated one. In contrast to resonant narrow band antennas, deviations due to the fabrication tolerances are acceptable as the performance of this ultra-wideband antenna varies slowly with frequency.

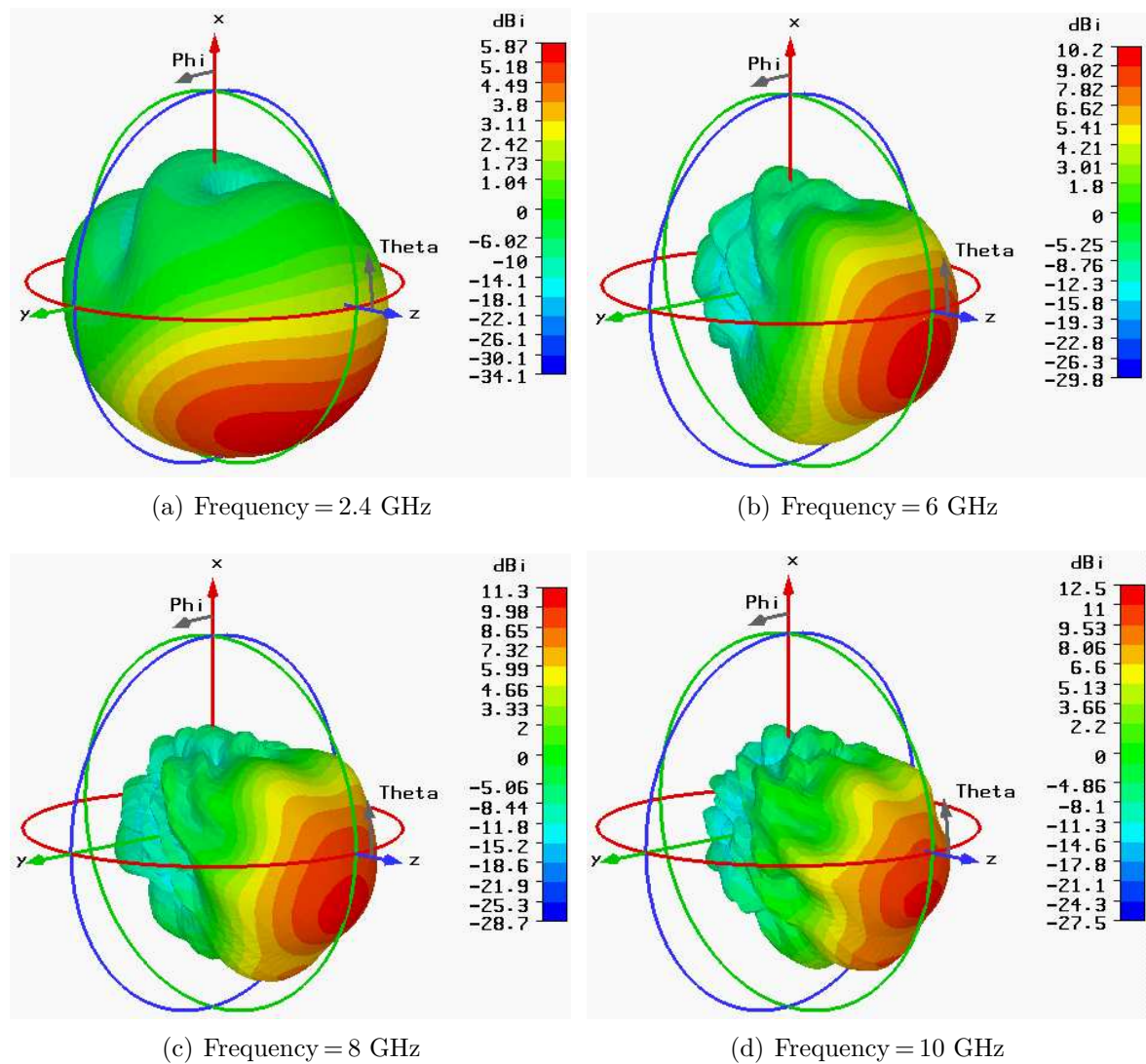


Figure 4.23: Computed antenna radiation patterns at different frequencies.

4. Analysis of an Ultra-wideband Antenna

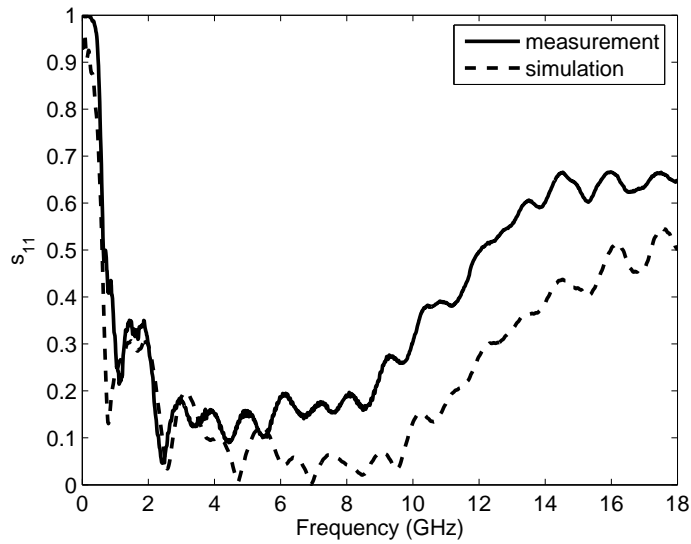


Figure 4.24: Comparison simulated and measured return losses.

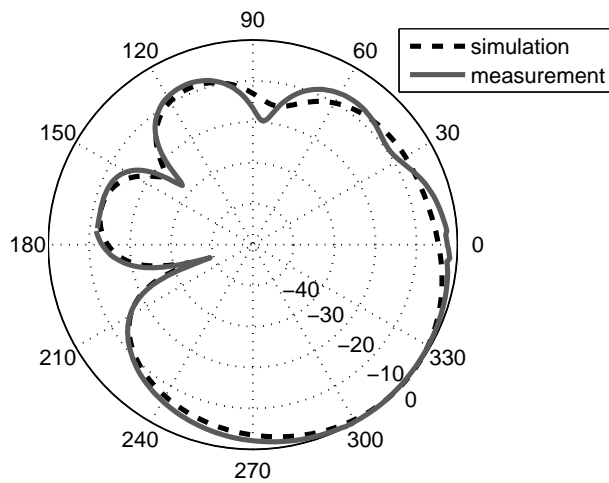


Figure 4.25: Comparison between simulated and measured E-plane radiation pattern at 2.4 GHz.

Chapter 5

Application of a Hybrid Method to Characterize Radiating Apertures

5.1 Prologue

In present days, the world has become a global village by and large due to the booming multimedia communication systems. Among the other components of a modern communication system, one of major importance is the antenna system. Even a small improvement of the antenna characteristics can be translated into higher data rate hence reducing the running costs of the communication system.

The conventional way for long distance communication are the reflector and dielectric lens antenna systems. Proper illumination of these antenna systems is usually done by aperture antennas (horn antennas). Characterization of these type of antennas is a very critical and important issue in this context.

There are numerous CEM methods to characterize radiating apertures - some of which have been mentioned in Chapter 1. Each of these methods has its merits and demerits. Many of them assume certain approximations during the field calculations (i.e infinite flange, absorbing boundaries etc.). In the fully numerical techniques like the FDTD, FEM or FIT, the radiation patterns of aperture antennas are usually computed applying near to far field transformations on the near field distributions of the aperture. This usually requires an additional post-processing step after the field computations. However, the problems concerning radiations from the aperture antennas can be considered as a combination of a closed problem (looking into the internal antenna geometry from the aperture) and an open problems (looking outside from the antenna aperture). In these cases it is possible to analyze the internal and external part separately with techniques best suited for the considered region. This type of hybridizations are aimed to achieve flexibility, numerical efficiency and accuracy for the considered problem. In this section such a hybrid method involving the MMT and GMT is presented. As both the techniques are semi analytical, this hybrid method aims for efficient computation with good numerical accuracy, without any assumptions concerning the termination of the computation domain.

5. Application of a Hybrid Method to Characterize Radiating Apertures

GMT is well-known for electromagnetic field computations due to its flexibility for modeling complex structures. Early GMT approaches can be found in the literature as the extended boundary condition method (EBCM) [106, 55]. In this method, the scattered field is represented on the boundary of the scatterer as a summation of multipole fields. When the locations, number and strengths of the multipoles are appropriately determined, the boundary conditions are satisfied and the scattered field can be computed directly from the multipole expansion. The application of GMT [107, 52] has been extended to a variety of applications like modeling of photonic crystals, nanostructures, optical devices, neuromagnetic field computations, simulation of EM problems involving biological tissues, etc. [108, 109, 110, 111].

GMT has found application also for accurate and realistic modeling of aperture antennas, as e.g. corrugated horns, used as the feed for reflector and dielectric-lens antennas. When using GMT, approximations like infinitely extended conducting ground plane or absorbing boundaries are not required for the characterization of the radiating apertures. When considering also the internal part of the horn, the modal scattering matrix can be computed by combining a modal expansion for the aperture field and a multiple multipole expansion for the external field along with a point matching technique [112, 113].

Multipoles distribution along the structure under examination is a crucial point in GMT. Improperly placed multipoles, or presence of redundant multipoles, can cause numerical instability leading to inaccurate results. There are some rules for semi-automatic multipole setting [111, 52, 114, 115], but, in many cases, the existing algorithms for automatic multipole placement are not robust, slow and not entirely suitable for complex geometries. To overcome this problem, one can start with a high density of multipoles uniformly distributed over the object under examination. The redundant multipoles can then be automatically identified and eliminated hence providing a numerically stable system. In this chapter, after presenting the MMT-GMT hybrid method for field computations, two different approaches to identify the redundant multipoles will be suggested and compared. The first procedure involves the well known Singular Value Decomposition (SVD) and the generalized angle concept [116, 117] while the second procedure involves the rank revealing QR factorizations.

In the SVD approach, the identification of the multipoles is done in two steps. In the first step, SVD [118, 119] is applied to determine the conditioning and the singular values of the involved system matrix. The number of singular values below a certain threshold value, gives the number of linearly dependent columns of the system matrix with respect to the chosen threshold. In the second step, the absolute value of the complex angles between a particular column and all the other columns are evaluated. When the columns are linearly dependent or nearly linearly dependent, then they have a small angle between them. Depending upon the value of this angle, the pair of columns are sorted and one of those pairs (having higher linear dependency, i.e. lower angle value) is removed. It may be noted here that each column in the system matrix represents one multipole. The problem conditioning increases significantly as these multipoles are removed from the expansion.

In the second approach, the rank revealing QR factorization [118, 119, 120] with a certain threshold is applied to the system matrix \mathbf{A} . From the permutation matrix, the columns which are considered to be linearly dependent with respect to the considered threshold are obtained. Afterwards the identified columns can be removed from the system matrix.

The two proposed approaches have been applied in the case of horn antennas with elliptical apertures [113]. The accuracies of both the methods have been validated through error estimation at the boundaries and with comparisons of the farfield patterns with that obtained from a commercial CEM software.

5.2 Theoretical basics

5.2.1 The Generalized Multipole Technique

GMT is a semi-analytic technique used in the frequency domain for electromagnetic field computations. Let us consider a domain D with a boundary S (on which the field distribution is known) within which the electromagnetic fields are sought. The electromagnetic fields within D are governed by Maxwell's equations and have to satisfy the boundary conditions (or the known field distributions) on S . In GMT, the enforcement of the boundary conditions are done numerically, using the point matching technique.

To represent the electromagnetic fields within D , basis functions are chosen which are already solutions of the governing equations. Although the simple harmonic functions (i.e. the sine or cosine functions) can be used as basis functions to represent the fields, the energy associated with such a field is distributed uniformly in space and the total energy is infinite. This can cause numerical problems in case the fields to be represented is concentrated in a certain area. For these reasons, it is of interest to use the solutions of the field equations which are concentrated around a certain point in space. The multipoles or p -expansions are such solutions having singularities at their origins. These

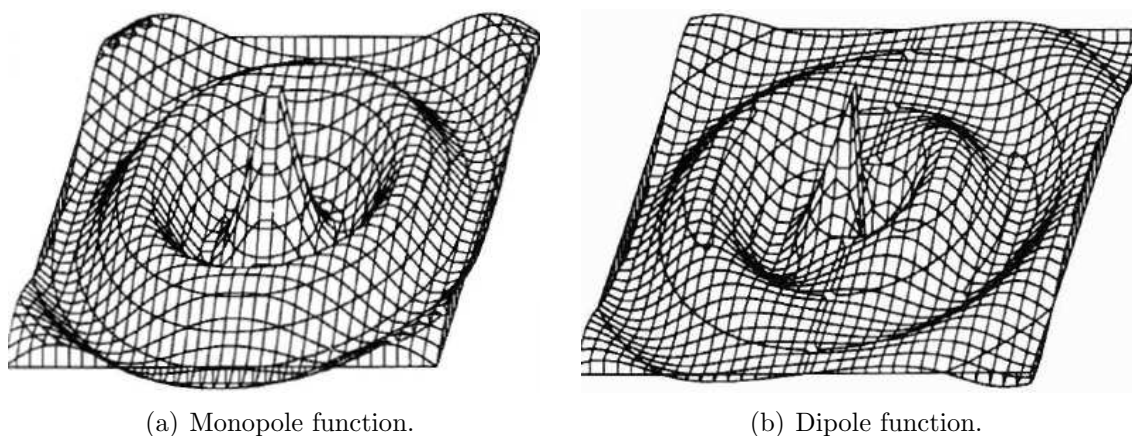


Figure 5.1: Monopole and dipole functions [52].

5. Application of a Hybrid Method to Characterize Radiating Apertures

multipole expansions have been used for the field computations in this section. Fig. 5.1 shows the amplitude plot of such a multipole function with zero-order (monopole) and with order 1 (dipole) [52]. As the multipoles are singular at the origin, the origin of the multipoles used for the field computations must lie outside the domain in which the fields have been sought.

5.2.2 The GMT-MMT hybrid technique for characterization of radiating apertures

5.2.2.1 Formulation of the problem

Let us consider the volume V which is enclosed by a surface S . The surface S consists of a metallic part S_c and an aperture S_a as shown in Fig. 5.2. The region outside V is source free and the electromagnetic fields are sought in this region, for a particular field distribution on S_a . Determination of the electromagnetic field distribution at S_a can be considered as a closed problem, which can be obtained from the analysis of the internal geometry. In this analysis, the MMT has been applied for the aperture field calculation. As the basis functions to represent the source free electromagnetic fields outside the volume V , multipole expansions are used. The multipoles are located within the volume V , near the surface of the radiating object, as shown in Fig. 5.2. The weighting factors for the multipole expansion to represent the external field is calculated by enforcing the boundary conditions at S_c and S_a . This is done by means of an extended point patching technique.

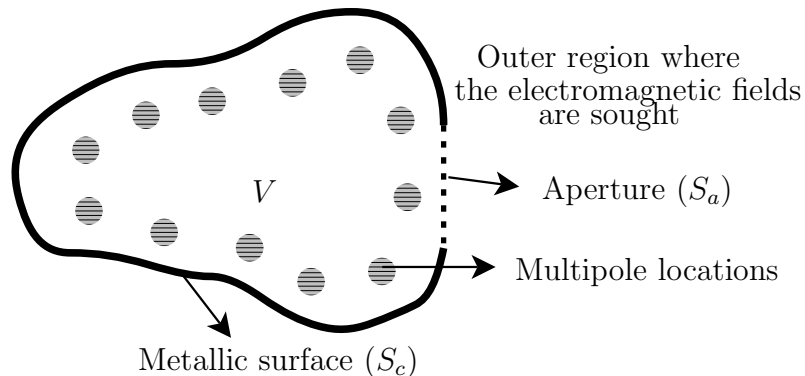


Figure 5.2: The radiating volume with the aperture.

5.2.2.2 Multiple Multipole Expansion for the external electromagnetic field

The fields radiated by a finite set of multipoles are used to represent the external electromagnetic field. The external field at a point \mathbf{r} can be expressed as,

$$\mathbf{E}^{(ext)}(\mathbf{r}) = \sum_k \sum_l Q_{kl} \cdot \mathbf{E}_l^{(mult)}(\mathbf{r} - \mathbf{r}_k) \quad (5.1)$$

$$\mathbf{H}^{(ext)}(\mathbf{r}) = \sum_k \sum_l Q_{kl} \cdot \mathbf{H}_l^{(mult)}(\mathbf{r} - \mathbf{r}_k) \quad (5.2)$$

Where, $\mathbf{E}_l^{(mult)}$ and $\mathbf{H}_l^{(mult)}$ are the multipole fields radiated by an l -th order multipole and \mathbf{r}_k denotes the location of the corresponding multipole. $\mathbf{E}_l^{(mult)}$ and $\mathbf{H}_l^{(mult)}$ are divided into TE and TM multipoles and the Q_{kl} 's are unknown excitation coefficients whose values are dependent on the geometry of the radiator under consideration (in this case, a horn antenna). The internal sum in (5.1) and (5.2) are double ones as the monochromatic multipoles have two degrees of freedom describing their polar functional dependence with respect to their local coordinates. The outer sum of the expansion is also a double summation as two dimensional multipole location distributions are considered for three dimensional radiating structures. The explicit expressions for the multipole fields can be found in [112], [121]. In order to determine the unknown expansion coefficients (Q_{kl}), the boundary conditions are enforced on the surface of the radiating object and on the aperture using the point matching technique.

Let the two mutually perpendicular vectors $\hat{\mathbf{u}}$ and $\hat{\mathbf{v}}$ represent the unit vectors tangential to the antenna surface. Let $\hat{\mathbf{n}}$ represent the unit vector normal to S which is perpendicular to both $\hat{\mathbf{u}}$ and $\hat{\mathbf{v}}$. Now, if we enforce the boundary conditions for the tangential electric field and the normal magnetic field on both S_a and S_c , we have the following equations:

$$E_u^{(ext)}(\mathbf{r}_{\mathbf{m}_a}) = \hat{\mathbf{u}}(\mathbf{r}_{\mathbf{m}_a}) \cdot \mathbf{E}^{(a)}(\mathbf{r}_{\mathbf{m}_a}) \quad (5.3)$$

$$E_v^{(ext)}(\mathbf{r}_{\mathbf{m}_a}) = \hat{\mathbf{v}}(\mathbf{r}_{\mathbf{m}_a}) \cdot \mathbf{E}^{(a)}(\mathbf{r}_{\mathbf{m}_a}) \quad (5.4)$$

$$H_n^{(ext)}(\mathbf{r}_{\mathbf{m}_a}) = \hat{\mathbf{n}}(\mathbf{r}_{\mathbf{m}_a}) \cdot \mathbf{H}^{(a)}(\mathbf{r}_{\mathbf{m}_a}) \quad (5.5)$$

$$E_u^{(ext)}(\mathbf{r}_{\mathbf{m}_c}) = E_v^{(ext)}(\mathbf{r}_{\mathbf{m}_c}) = H_n^{(ext)}(\mathbf{r}_{\mathbf{m}_c}) = 0 \quad (5.6)$$

Enforcement of the boundary conditions for the tangential magnetic field and the normal electric field on the aperture surface S_a gives:

$$H_u^{(ext)}(\mathbf{r}_{\mathbf{m}_a}) = \hat{\mathbf{u}}(\mathbf{r}_{\mathbf{m}_a}) \cdot \mathbf{H}^{(a)}(\mathbf{r}_{\mathbf{m}_a}) \quad (5.7)$$

$$H_v^{(ext)}(\mathbf{r}_{\mathbf{m}_a}) = \hat{\mathbf{v}}(\mathbf{r}_{\mathbf{m}_a}) \cdot \mathbf{H}^{(a)}(\mathbf{r}_{\mathbf{m}_a}) \quad (5.8)$$

$$E_n^{(ext)}(\mathbf{r}_{\mathbf{m}_a}) = \hat{\mathbf{n}}(\mathbf{r}_{\mathbf{m}_a}) \cdot \mathbf{E}^{(a)}(\mathbf{r}_{\mathbf{m}_a}) \quad (5.9)$$

Here, $\mathbf{r}_{\mathbf{m}_a}$'s denote the matching points on S_a , $\mathbf{r}_{\mathbf{m}_c}$'s denote the matching points on S_c , $\mathbf{E}^{(a)}$ and $\mathbf{H}^{(a)}$ are the aperture electric and magnetic field, respectively.

5. Application of a Hybrid Method to Characterize Radiating Apertures

Using equations (5.3)-(5.9) the equations (5.1)-(5.2) can be expressed in the matrix form as:

$$\begin{bmatrix} \begin{bmatrix} C^{(u-TE)_a} \\ C^{(v-TE)_a} \\ C^{(n-TE)_a} \end{bmatrix} \\ \begin{bmatrix} C^{(u-TM)_a} \\ C^{(v-TM)_a} \\ C^{(n-TM)_a} \end{bmatrix} \end{bmatrix} \begin{bmatrix} \mathbf{Q}^{(TE)} \\ \mathbf{Q}^{(TM)} \end{bmatrix} = \begin{bmatrix} \mathbf{V}^{(u)} \\ \mathbf{V}^{(v)} \\ \tilde{\mathbf{V}}^{(n)} \end{bmatrix} \quad (5.10)$$

$$\begin{bmatrix} \begin{bmatrix} C^{(u-TE)_c} \\ C^{(v-TE)_c} \\ C^{(n-TE)_c} \end{bmatrix} \\ \begin{bmatrix} C^{(u-TM)_c} \\ C^{(v-TM)_c} \\ C^{(n-TM)_c} \end{bmatrix} \end{bmatrix} \begin{bmatrix} \mathbf{Q}^{(TE)} \\ \mathbf{Q}^{(TM)} \end{bmatrix} = 0 \quad (5.11)$$

$$\begin{bmatrix} \begin{bmatrix} \tilde{C}^{(u-TE)} \\ \tilde{C}^{(v-TE)} \\ \tilde{C}^{(n-TE)} \end{bmatrix} \\ \begin{bmatrix} \tilde{C}^{(u-TM)} \\ \tilde{C}^{(v-TM)} \\ \tilde{C}^{(n-TM)} \end{bmatrix} \end{bmatrix} \begin{bmatrix} \mathbf{Q}^{(TE)} \\ \mathbf{Q}^{(TM)} \end{bmatrix} = \begin{bmatrix} \mathbf{I}^{(u)} \\ \mathbf{I}^{(v)} \\ \tilde{\mathbf{I}}^{(n)} \end{bmatrix} \quad (5.12)$$

Here $\mathbf{Q}^{(TE)}$ and $\mathbf{Q}^{(TM)}$ are column vectors containing the TE and TM multipole expansion coefficients Q_{kl} and $\mathbf{V}^{(u)}$, $\mathbf{V}^{(v)}$ and $\tilde{\mathbf{V}}^{(n)}$ are M_a -dimensional column vectors containing the u-component, v-component of the electric and n-component of the magnetic field at the aperture matching points. The column vectors $\mathbf{I}^{(u)}$, $\mathbf{I}^{(v)}$ and $\tilde{\mathbf{I}}^{(n)}$ are also of dimension M_a with their elements being the u-component, v-component of the magnetic and n-component of the electric field at the aperture matching points.

5.2.2.3 Modal expansion of the aperture field

As the aperture field is used to enforce some of the boundary conditions, it is to be calculated precisely. We use the modal analysis [58, 59] which is the most systematic and rigorous technique for this purpose. The aperture field is represented by a modal expansion in terms of a hollow waveguide whose cross-section has the same geometry and dimensions as the aperture. This will be termed as the aperture waveguide.

Let the axial magnetic field and cutoff wave number of the i^{th} TE mode of the aperture waveguide be ψ_{hi} and k_{hi} respectively. Let ψ_{ei} and k_{ei} be the same for the i^{th} TM mode of the aperture waveguide. Now, the tangential and normal components of the aperture field can be expressed by the following modal expansions:

$$\mathbf{E}_t^{(a)} = E_u^{(a)} \hat{\mathbf{u}}_a + E_v^{(a)} \hat{\mathbf{v}}_a \quad (5.13)$$

$$\mathbf{E}_t^{(a)} = \sum_i V_i^{(TE)} (\nabla_t \psi_{hi} \times \hat{\mathbf{n}}_a) + \sum_i V_i^{(TM)} \nabla_t \psi_{hi} \quad (5.14)$$

$$\mathbf{H}_t^{(a)} = H_u^{(a)} \hat{\mathbf{u}}_a + H_v^{(a)} \hat{\mathbf{v}}_a \quad (5.15)$$

$$\mathbf{H}_t^{(a)} = \sum_i I_i^{(TE)} \nabla_t \psi_{hi} + \sum_i I_i^{(TM)} (\hat{\mathbf{n}}_a \times \nabla_t \psi_{hi}) \quad (5.16)$$

$$E_n^{(a)} = \frac{-1}{j\omega\epsilon_0} \sum_i k_{ei}^2 I_i^{(TM)} \psi_{ei} \quad (5.17)$$

$$H_n^{(a)} = \frac{-1}{j\omega\mu_0} \sum_i k_{hi}^2 V_i^{(TE)} \psi_{hi} \quad (5.18)$$

Here, ∇_t is the transverse component of the gradient operator, ω is the operating frequency, ε_0 and μ_0 are the free space permittivity and permeability respectively. $V_i^{(TE)}$, $V_i^{(TM)}$ and $I_i^{(TE)}$, $I_i^{(TM)}$ are the TE and TM modal voltages and currents respectively. It has been assumed that the aperture tangential and normal directions coincide with the transverse and axial directions of the aperture waveguide and $\hat{\mathbf{u}}_a$, $\hat{\mathbf{v}}_a$ and $\hat{\mathbf{n}}_a$ are the unit vectors along the tangential and normal direction respectively. The sums in (5.14) and (5.16) are double ones as the waveguide modes have two degrees of freedom. Now we can express the column vectors $\mathbf{V}^{(u)}$, $\mathbf{V}^{(v)}$, $\tilde{\mathbf{V}}^{(n)}$, $\mathbf{I}^{(u)}$, $\mathbf{I}^{(v)}$ and $\tilde{\mathbf{I}}^{(n)}$ in (5.10) and (5.12) in terms of the modal voltages and currents as:

$$\begin{bmatrix} \mathbf{V}^{(u)} \\ \mathbf{V}^{(v)} \\ \tilde{\mathbf{V}}^{(n)} \end{bmatrix} = \begin{bmatrix} \begin{bmatrix} D^{(u-TE)} \\ D^{(v-TE)} \\ D^{(n-TE)} \end{bmatrix} & \begin{bmatrix} D^{(u-TM)} \\ D^{(v-TM)} \\ [0] \end{bmatrix} \end{bmatrix} \begin{bmatrix} \mathbf{V}^{(TE)} \\ \mathbf{V}^{(TM)} \end{bmatrix} \quad (5.19)$$

$$\begin{bmatrix} \mathbf{I}^{(u)} \\ \mathbf{I}^{(v)} \\ \tilde{\mathbf{I}}^{(n)} \end{bmatrix} = \begin{bmatrix} \begin{bmatrix} \tilde{D}^{(u-TE)} \\ \tilde{D}^{(v-TE)} \\ [0] \end{bmatrix} & \begin{bmatrix} \tilde{D}^{(u-TM)} \\ \tilde{D}^{(v-TM)} \\ \tilde{D}^{(n-TM)} \end{bmatrix} \end{bmatrix} \begin{bmatrix} \mathbf{I}^{(TE)} \\ \mathbf{I}^{(TM)} \end{bmatrix} \quad (5.20)$$

5.2.2.4 Calculation of the radiation admittance and scattering matrix

The matching of the tangential electric field and normal magnetic field on the entire surface of the radiating object ($S = S_a \cup S_c$) can be obtained from (5.10), (5.11) and (5.19) as:

$$\begin{aligned} & \begin{bmatrix} \begin{bmatrix} C^{(u-TE)_a} \\ C^{(v-TE)_a} \\ C^{(n-TE)_a} \\ C^{(u-TE)_c} \\ C^{(v-TE)_c} \\ C^{(n-TE)_c} \end{bmatrix} & \begin{bmatrix} C^{(u-TM)_a} \\ C^{(v-TM)_a} \\ C^{(n-TM)_a} \\ C^{(u-TM)_c} \\ C^{(v-TM)_c} \\ C^{(n-TM)_c} \end{bmatrix} \end{bmatrix} \begin{bmatrix} \mathbf{Q}^{(TE)} \\ \mathbf{Q}^{(TM)} \end{bmatrix} \\ &= \begin{bmatrix} \begin{bmatrix} D^{(u-TE)} \\ D^{(v-TE)} \\ D^{(n-TE)} \\ [0] \\ [0] \\ [0] \end{bmatrix} & \begin{bmatrix} D^{(u-TM)} \\ D^{(v-TM)} \\ [0] \\ [0] \\ [0] \\ [0] \end{bmatrix} \end{bmatrix} \begin{bmatrix} \mathbf{V}^{(TE)} \\ \mathbf{V}^{(TM)} \end{bmatrix} \end{aligned} \quad (5.21)$$

5. Application of a Hybrid Method to Characterize Radiating Apertures

The equation for the tangential magnetic field and normal electric field on the aperture can be obtained by combining (5.12) and (5.20) which reads:

$$\begin{aligned}
 & \begin{bmatrix} \left[\begin{array}{c} \tilde{C}^{(u-TE)} \\ \tilde{C}^{(v-TE)} \\ \tilde{C}^{(n-TE)} \end{array} \right] & \left[\begin{array}{c} \tilde{C}^{(u-TM)} \\ \tilde{C}^{(v-TM)} \\ \tilde{C}^{(n-TM)} \end{array} \right] \end{bmatrix} \begin{bmatrix} \mathbf{Q}^{(TE)} \\ \mathbf{Q}^{(TM)} \end{bmatrix} \\
 &= \begin{bmatrix} \left[\begin{array}{c} \tilde{D}^{(u-TE)} \\ \tilde{D}^{(v-TE)} \\ [0] \end{array} \right] & \left[\begin{array}{c} \tilde{D}^{(u-TM)} \\ \tilde{D}^{(v-TM)} \\ \tilde{D}^{(n-TM)} \end{array} \right] \end{bmatrix} \begin{bmatrix} \mathbf{I}^{(TE)} \\ \mathbf{I}^{(TM)} \end{bmatrix}
 \end{aligned} \tag{5.22}$$

Writing (5.21) and (5.22) in compact form, we obtain,

$$[C] \mathbf{Q} = [D] \mathbf{V} \tag{5.23}$$

$$[\tilde{C}] \mathbf{Q} = [\tilde{D}] \mathbf{I} \tag{5.24}$$

The number of columns and rows of the matrices in (5.23) and (5.24) are given in Table 5.1. Here, N_{mp} is the total number of multipoles used for the expansion of the external field and N_{md} is the total number of modes used for the modal expansion of the aperture field. For a unique determination of \mathbf{Q} , the total number of multipoles (N_{mp}) should

Matrices	Number of rows	Number of columns
C	$3 \times (M_a + M_c)$	N_{mp}
\tilde{C}	$3 \times M_a$	N_{mp}
D	$3 \times (M_a + M_c)$	N_{md}
\tilde{D}	$3 \times M_a$	N_{md}

Table 5.1: Rows and columns of the matrices.

be less than or equal to $3 \times (M_a + M_c)$ and the unique determination of the aperture scattering matrix demands the total number of modes N_{md} to be less than or equal to $3 \times M_a$. Using (5.23) and (5.24) the multipole excitation vector \mathbf{Q} and the aperture modal current vector \mathbf{I} can be obtained as:

$$\mathbf{Q} = ([C^H] [C])^{-1} [C^H] [D] \mathbf{V} \tag{5.25}$$

$$\mathbf{I} = ([\tilde{D}^H] [\tilde{D}])^{-1} [\tilde{D}^H] [\tilde{C}] \mathbf{Q} \tag{5.26}$$

Where C^H denotes the Hermitian conjugate of C and D^H denotes the Hermitian conjugate of D . The aperture modal scattering matrix can be obtained using (5.25) and (5.26) as:

$$\mathbf{I} = [Y^{(a)}] \mathbf{V} \tag{5.27}$$

$$[Y^{(a)}] = ([\tilde{D}^H] [\tilde{D}])^{-1} [\tilde{D}^H] [\tilde{C}] ([C^H] [C])^{-1} [C^H] [D] \tag{5.28}$$

The corresponding modal scattering matrix is obtained by expressing the modal voltages and currents in terms of incident and reflected waves \mathbf{A} and \mathbf{B} respectively:

$$\mathbf{V} = [Z_w]^{\frac{1}{2}} (\mathbf{A} + \mathbf{B}) \quad (5.29)$$

$$\mathbf{I} = [Z_w]^{-\frac{1}{2}} (\mathbf{A} - \mathbf{B}) \quad (5.30)$$

$$\mathbf{B} = [S^{(a)}] \mathbf{A} \quad (5.31)$$

Where $[Z_w]$ is a diagonal matrix with its elements being the modal impedances given by:

$$Z_i^{(TE)} = \frac{\omega \mu_0}{\sqrt{k_0^2 - k_{hi}^2}} \quad (5.32)$$

$$Z_i^{(TM)} = \frac{\sqrt{k_0^2 - k_{ei}^2}}{\omega \varepsilon_0} \quad (5.33)$$

and $k_0^2 = \omega^2 \varepsilon_0 \mu_0$. The aperture modal scattering matrix can be obtained as:

$$[S^{(a)}] = ([I] + [Z_w]^{\frac{1}{2}} [Y^{(a)}] [Z_w]^{\frac{1}{2}})^{-1} ([I] - [Z_w]^{\frac{1}{2}} [Y^{(a)}] [Z_w]^{\frac{1}{2}}) \quad (5.34)$$

where $[I]$ is the identity matrix.

5.2.3 Problems of ill conditioning

The matrix equations (5.10)-(5.12) are over-determined, hence requiring an approximate solution for the field equations. The over-determined system of equation is created by choosing a higher number of matching points, hence producing a higher number of matching equations than the number of unknowns. In this way the achieved matching, while not being perfect at any one of the matching points, minimizes the local residues at the intermediate matching points. Another advantage of using an over-determined system is that the matching points choice is not critical. A high density of matching points results in a significant linear dependency among the rows of C and \tilde{C} matrices. However, as we use the pseudo-inverse to evaluate the unknown expansion coefficients (5.25), errors due to this type of redundancy are automatically reduced.

A very high density of the multipoles leads us to another type of redundancy. The columns of the C and \tilde{C} matrices in (5.23) and (5.24) contain the field components of a particular multipole at all the matching points. If the multipoles or the matching points are placed very densely, the field computed at a distant matching point for more than one multipole are almost equal. This leads to a high redundancy among the columns which has to be eliminated in order to have a numerically stable system.

5.2.4 Solution approaches

5.2.4.1 Singular value decomposition and identification of redundant multipoles

A reliable and robust means to analyze the conditioning and linear dependencies for a matrix is the Singular Value Decomposition (SVD) [118, 119]; in the SVD a large

5. Application of a Hybrid Method to Characterize Radiating Apertures

condition number indicates a poor conditioning of the matrix.

The $m \times n$ rectangular complex matrix C is decomposed into

$$C = U \cdot S \cdot V^H \quad (5.35)$$

Where U and V are unitary matrices, $S = \text{diag}(\varsigma_1, \varsigma_2 \dots \varsigma_n)$ with $\varsigma_1, \varsigma_2 \dots \varsigma_n \geq 0$ and V^H denotes the Hermitian conjugate of V . In the above equation the $\varsigma_1, \varsigma_2 \dots$ are the singular values of C . Let us denote $\text{cond}(C)$ as the condition number of C defined as,

$$\text{cond}(C) = \frac{\varsigma_{max}}{\varsigma_{min}} \quad (5.36)$$

The conditioning of a problem depends upon the data accuracy (in our case the accuracy in computing the C matrix). If the data can be considered to be correct, and if the condition number of the matrix is 10^d , then about $(\epsilon - d)$ digits of accuracy in the solution can be achieved. Here, it has been assumed that the calculations are done with ϵ digits accuracy. As the condition number of a matrix with given maximum singular value (ς_{max}) is dependent on the minimum singular value (5.36), the accuracy of the solution is directly influenced by it.

It is clear from the above discussion that to improve the conditioning and hence minimize the error, we need to eliminate the very small singular values of C . The tolerable lower limit of the singular value is not unique and is dependent upon the acceptable error in the solution. We define a threshold t_{svd} which is the minimum value of the singular value that can be tolerated. If there are s singular values which are less than t_{svd} then we can say there is $N_{mp} - s$ number of linearly independent columns in C with respect to our chosen t_{svd} .

To identify the redundant multipoles (linearly dependent columns of C), we apply the concept of generalized angle between vectors. The angle θ between two n -dimensional vectors in the Hilbert space is defined as:

$$\theta = \cos^{-1} \frac{\langle u \cdot v \rangle}{\|u\|_2 \cdot \|v\|_2} \quad (5.37)$$

where $\langle u \cdot v \rangle$ denotes the inner product between the vectors u and v . When two vectors have a vanishing angle between them then they are nearly parallel. We extend this approach to detect the column redundancy in C . As all the elements of C are complex, we calculate the angle matrix A according to the following formula for each columns of C

$$A_{ij} = \cos^{-1} \left(\frac{|C_j^* \cdot C_i|}{\|C_i\|_2 \cdot \|C_j\|_2} \right) \quad (5.38)$$

Where C_i denotes the i -th column of C . Both subscripts i and j run from 1 to N_{mp} . It can be easily noticed that $A_{ij} = A_{ji}$, so we need to calculate only the upper or lower triangle of the angle matrix A . Two columns having a small angle value contain less information with respect to each other than two columns having a larger angle value. The columns having lowest angle values between them are sorted out and one of them

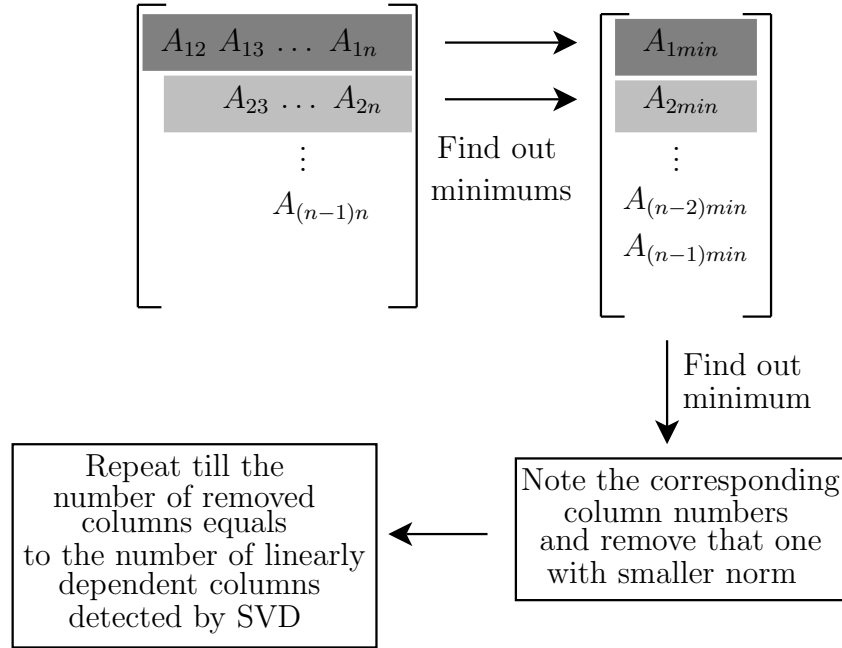


Figure 5.3: Identification of the multipoles through the angle approach.

is removed from the system. The process of sorting out is continued till s columns are removed from the system. It can be noted that removing one column from C is equivalent to removing one multipole from the system. The procedure of multipole reduction with this approach is summarized in the Fig. 5.3.

5.2.4.2 Rank Revealing QR factorizations to identify redundant multipoles

The rank revealing QR (RRQR) factorization [118, 120] is widely used for estimating the numerical ranks in case of rank deficit matrices. We can compute a decomposition for C as

$$CP = QR = Q \begin{pmatrix} R_{11} & R_{12} \\ 0 & R_{22} \end{pmatrix} \quad (5.39)$$

where P is a permutation matrix, Q has orthonormal columns, R is an upper triangular matrix and R_{11}, R_{12}, R_{22} are the submatrices of R . R_{11} is of order r , where r represents the numerical rank of C with respect to a particular threshold t_{qr} . This decomposition is called a rank revealing QR (RRQR) factorization if the following properties are satisfied:

$$\text{cond}(R_{11}) \approx \frac{\varsigma_1}{\varsigma_r} \quad (5.40a)$$

$$\|R_{22}\|_2 = \varsigma_{\max}(R_{22}) \approx \varsigma_{r+1} \quad (5.40b)$$

5. Application of a Hybrid Method to Characterize Radiating Apertures

If the numerical rank of C is well-defined, the RRQR factorization (5.39) reveals the numerical rank of C by providing a well-conditioned leading submatrix R_{11} and a trailing submatrix R_{22} of small norm [118, 120]. From the permutation matrix P we can find out the columns which are treated as numerically dependent and eliminate them from C . The ZGEPX routine [122] along with the LAPACK routines have been used for the RRQR decompositions.

5.3 Simulation results

Radiating elliptical apertures of different eccentricities mounted on a circular flange have been considered for the simulations. To simplify the calculations, the elliptical apertures have been considered to be illuminated with the fundamental TE_{11}^e mode only. One fourth of the whole geometry has been analyzed by employing the em-symmetry (i.e. electric wall at XZ plane and magnetic wall at YZ plane).

The actual boundary condition of the problem with the considered excitation is shown in Fig. 5.6(a), where the color bar represents the electric field value. When the fields produced by the multipole expansion in equations (5.1) and (5.2) match this boundary condition, then the radiated field of the aperture is well represented. The accuracy of the electric field representation on the horn boundary gives an estimation about the accuracy of the radiated field representation. Here it can be noted that the actual electric field is calculated using equations (5.29), (5.30) and (5.19) considering the fundamental TE_{11}^e mode as being the incident one.

We start with a high density of multipoles inside the analyzed structure. A total number of 1194 multipoles located in 199 locations has been considered; in particular, 400 matching points on the aperture and 1205 matching points on the metallic surface have been selected as the field matching points. The schematic diagram of a horn structure under analysis along with the relevant coordinates is shown in Fig. 5.4. The schematic diagram in Fig. 5.5 shows the multipole distribution inside the antenna and

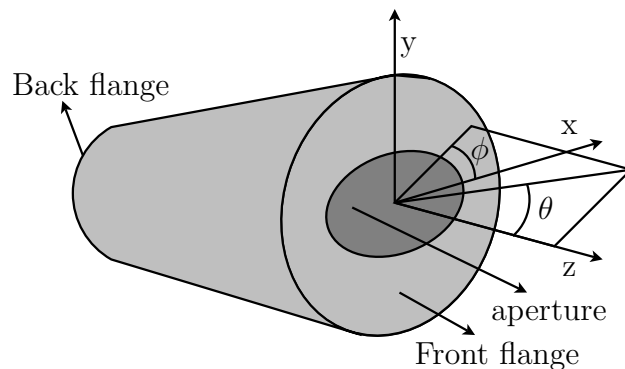


Figure 5.4: Schematic diagram of the structure under analysis.

the distance δ between the horn boundary and multipole surface. Three structures with elliptical apertures (with different eccentricities) have been considered. Both the front and back flanges have been considered as circular, with diameters 140 mm and 80 mm respectively. The length of the horn is 40 mm, the major axis of the radiating aperture is 70 mm, the minor axes are 60.62, 49.98 and 30.51 mm, respectively (corresponding to the eccentricities 0.5, 0.7 and 0.9).

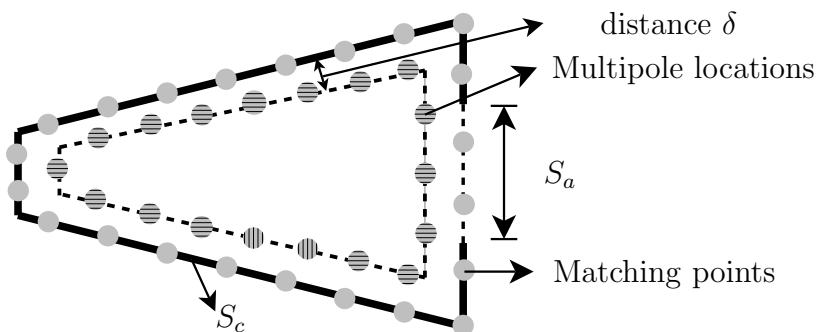


Figure 5.5: The aperture and antenna surface with the multipole locations and the matching points.

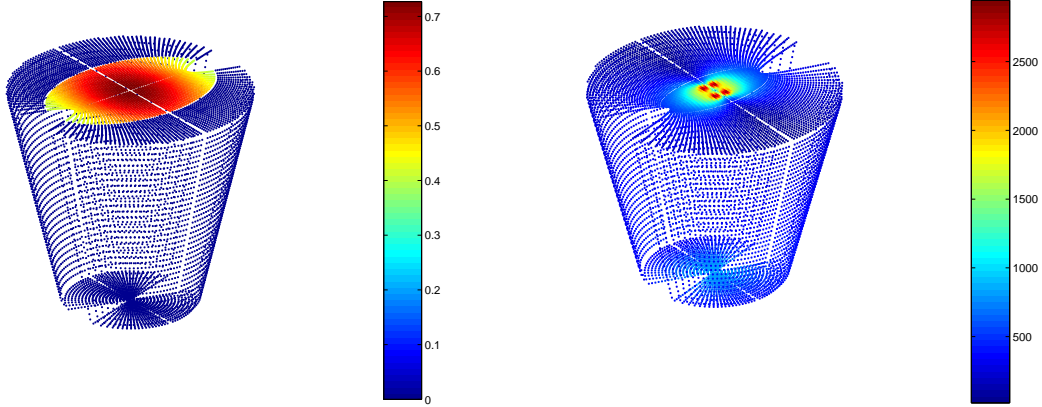
The condition number for the C matrices without any multipole reduction is of the order 10^{11} or larger. If we use these system of equations for the field computations, the obtained fields are wrong as illustrated in Fig. 5.6(b) which shows the magnitude of the computed electric field at the horn boundary without multipole reduction. The color bar represents the strength of the electric field.

5.3.1 Simulation results: SVD-angle method

The linear algebra package LAPACK [123] has been used for the first step of this approach i.e. for the SVD. We have considered a threshold (t_{svd}) and have used the angle approach to identify the redundant multipoles. As the threshold (t_{svd}) is increased, a higher number of redundant multipoles is detected. As we exclude these multipoles from the expansion, the conditioning of the problem improves. Fig. 5.8 shows the effect of increasing threshold on condition number and error in the field computation at the boundary of the structure.

In Fig. 5.8(a), the difference between the magnitudes of the actual electric field (representing the boundary condition) and calculated electric field is plotted at the horn boundaries. In Fig. 5.8(b) the improvement of the condition number is plotted against the corresponding thresholds (t_{svd}). It can be noted here that the errors are calculated at the points which are different from the field matching points. From the error plot it can be seen that the error decreases as the threshold is increased but after $t_{svd} = 10^{-3}$ the error remains constant. In order to keep the error a minimum while

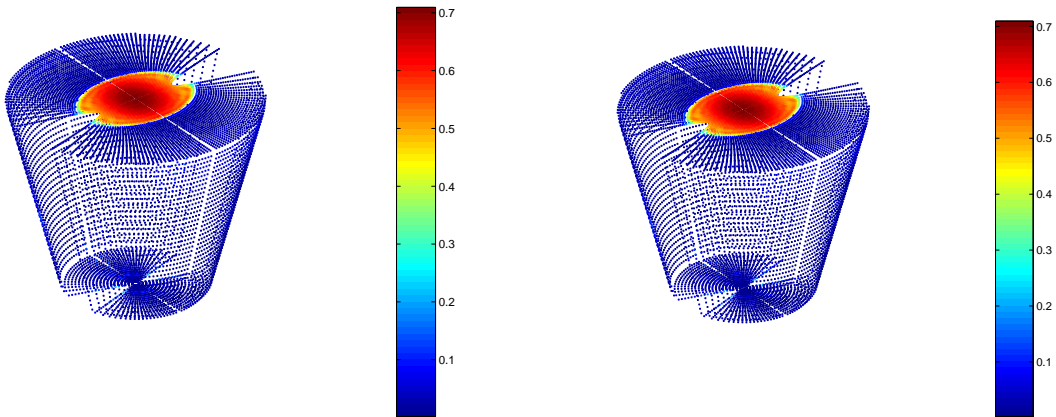
5. Application of a Hybrid Method to Characterize Radiating Apertures



(a) Magnitude of the actual electric field representing the boundary condition of the problem. (b) Computed electric field magnitude at the boundary without multipole reduction.

Figure 5.6: The actual boundary condition and magnitude of the computed electric field at the boundary without multipole reduction.

having a maximum number of multipoles, we can take the optimum threshold as 10^{-3} . It turns out that the variation of error with threshold follows the same trend in the case of elliptical apertures with different eccentricities. Fig. 5.7(a) shows the computed field after multipole reduction with $t_{svd} = 10^{-3}$.

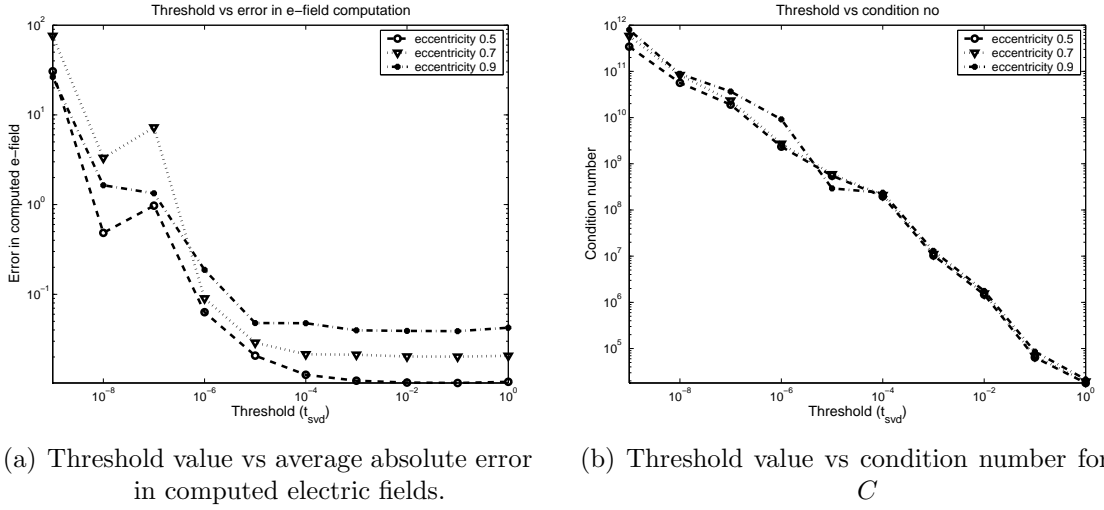


(a) Computed electric field magnitude after multipole reduction with SVD-angle approach for $t_{svd} = 10^{-3}$. (b) Computed electric field magnitude after multipole reduction with RRQR approach for $t_{rrqr} = 10^{-6}$.

Figure 5.7: Computed electric field magnitudes on the horn boundary after multipole reduction by both the approaches.

In Fig. 5.10(a), the frequency dependency of the deleted multipoles for the elliptical aperture with eccentricity 0.7 are shown. Two different cases have been considered:

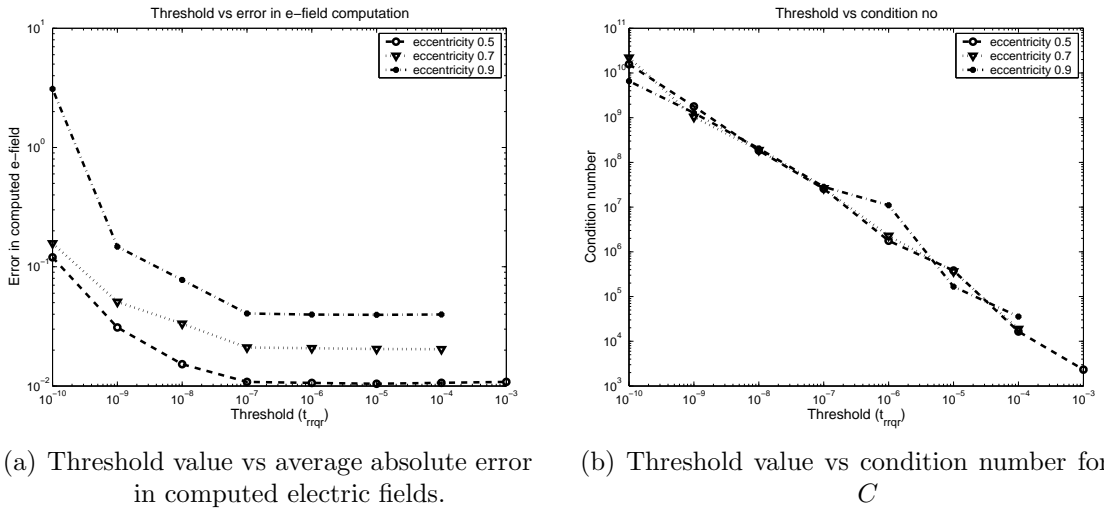
5.3 Simulation results



(a) Threshold value vs average absolute error in computed electric fields. (b) Threshold value vs condition number for C

Figure 5.8: Threshold value (t_{svd}) vs condition number for C and threshold value (t_{svd}) vs average error in electric field computation for different elliptical apertures in case of SVD-angle approach.

in the first case, the distance between the multipole surface and the horn boundary (the distance δ , with reference to Fig. 5.5) has been kept constant ($\frac{1}{8}$ th of the longest wavelength), while in the second case, a δ depending upon the operating wavelength ($\frac{1}{8}$ th of the corresponding wavelength) has been used. It can be seen that for fixed δ , the number of deleted multipoles has a very slow tendency to increase with increasing



(a) Threshold value vs average absolute error in computed electric fields. (b) Threshold value vs condition number for C

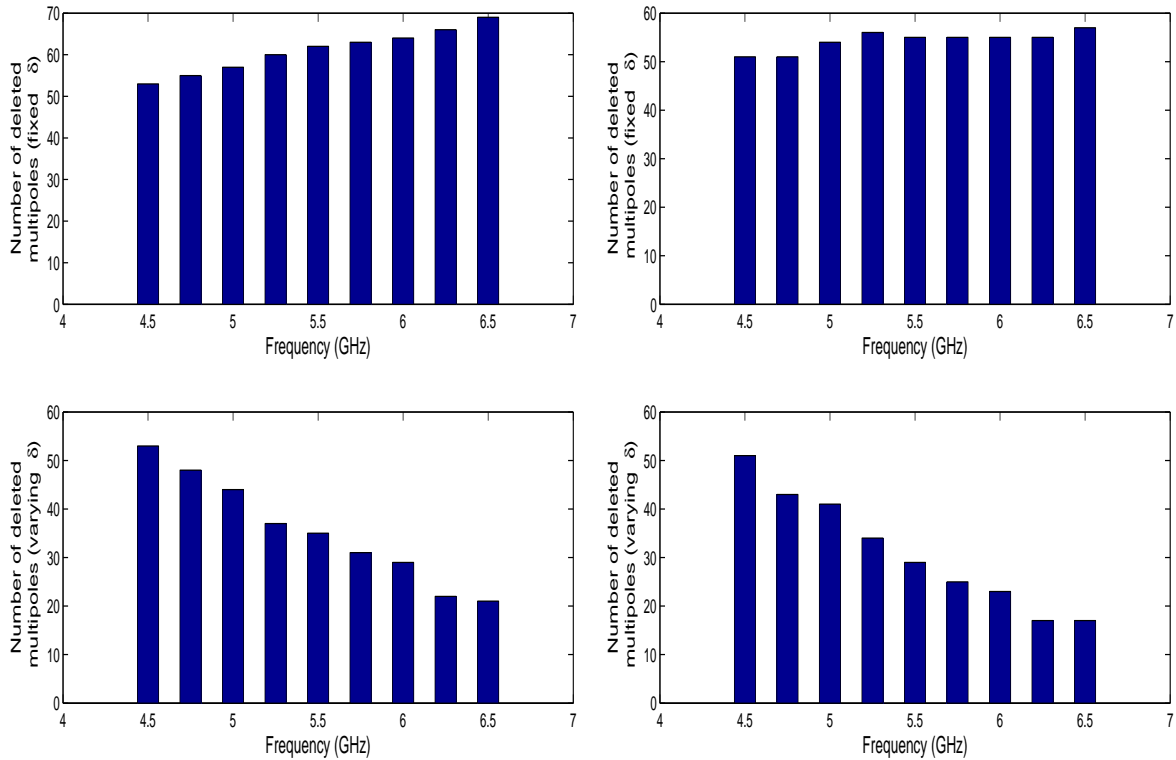
Figure 5.9: Threshold value (t_{rrqr}) vs condition number for C and threshold value (t_{rrqr}) vs average error in electric field computation for different elliptical apertures in case of RRQR approach.

5. Application of a Hybrid Method to Characterize Radiating Apertures

frequency (upper graph of Fig. 5.10(a)). It is worthy to note that in this case, about 60 percent of the deleted multipoles are common for adjacent frequencies. In the second case, the number of deleted multipoles decreases steadily with increasing frequencies as seen in the lower graph of Fig. 5.10(a). For elliptical apertures of different eccentricities, the same trend is followed.

5.3.2 Simulation results: RRQR method

The ZGEPX routine [122] along with the LAPACK routines [123] have been used for the RRQR decomposition. We have used the inverse of the threshold t_{rrqr} as the upper bound for the condition number of R_{11} (5.39). After obtaining the indices of the columns which are considered linearly dependent during the rank revealing process, they are removed from C and the condition number of the new system of equations is obtained. In Fig. 5.9, condition numbers for different thresholds (t_{rrqr}) and the average error in electric field calculation at the boundary of the structure for different thresholds (t_{rrqr}) are shown.



(a) Number of deleted multipoles at different frequencies with fixed and constant δ in case of SVD-angle approach. (b) Number of deleted multipoles at different frequencies with fixed and constant δ in case of RRQR approach.

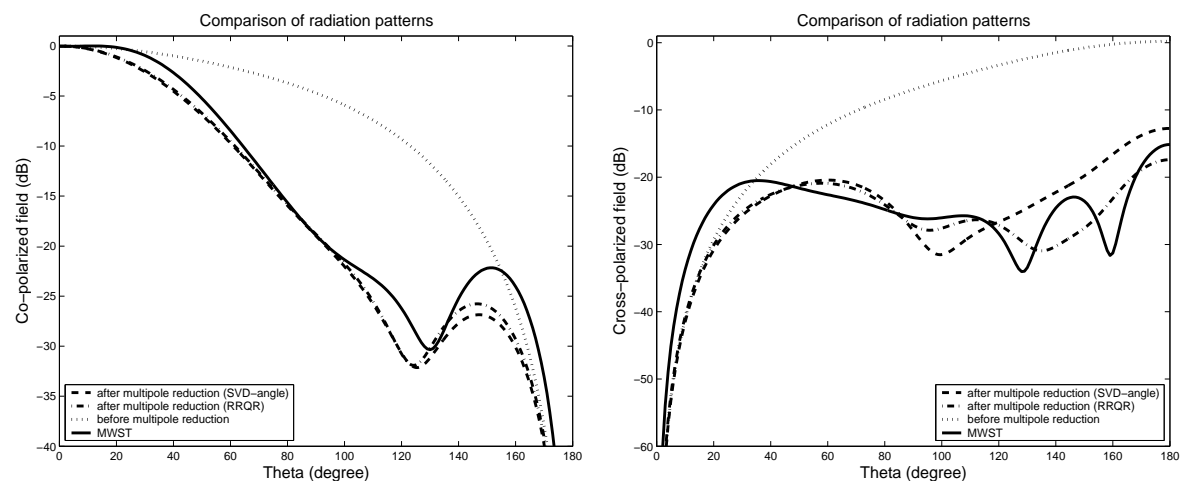
Figure 5.10: Number of deleted multipoles at different frequencies with fixed and constant δ .

It is clear from the plots that also in this case the average error decreases as the threshold is increased. The error remains constant for thresholds greater than 10^{-7} . In Fig. 5.7(b) the computed electric field after multipole reduction with $t_{rrqr} = 10^{-6}$ has been shown. The error jumps to a very high value if we go on increasing the threshold.

In Fig. 5.10(b), the frequency dependency of the deleted multipoles using RRQR decomposition (for elliptical aperture with eccentricity 0.7) are shown. Here also two different cases have been considered, one with constant δ and another with varying δ . It can be seen that the same trend of frequency dependency is also followed in this case. For constant δ , the number of deleted multipoles increases with a very slow rate (upper graph of Fig. 5.10(b)). For varying δ , here also the number of deleted multipoles decreases significantly (lower graph of Fig. 5.10(b)). Other elliptical apertures follow the same trend.

5.3.3 Comparison of the radiation patterns

A comparison of the computed co and cross-polarized radiation patterns for the aperture with eccentricity 0.7 is shown in Fig. 5.11. Radiation patterns were evaluated before and after multipole reduction (with both methods). It can be seen that the radiation pattern computed without multipole reduction as compared to that computed with multipole reduction is completely incorrect. This is because of the high numerical error due to the inversion of the ill-conditioned system matrix. Here, it may be noted that a large error in the aperture field computation produces a relatively small error on the radiation pattern - as can be noticed from Figs. 5.6 and 5.11. The radiation patterns for the same aperture have also been evaluated using MWST. A uniform waveguide (of length 30



(a) Comparison of the computed co-polarized fields (b) Comparison of the computed cross-polarized fields

Figure 5.11: Comparison of the radiation pattern for the elliptical aperture (eccentricity 0.7, $\phi = 45^\circ$) using GMT (before and after multipole reduction) and MWST.

5. Application of a Hybrid Method to Characterize Radiating Apertures

mm) with the same cross-section of the aperture was used to illuminate the aperture. The TE_{11}^e waveguide mode with a modulated gaussian temporal dependence was used for the excitation in the MWST simulations. To evaluate the backscattered radiation field with Microwave Studio software, the *Perfect Matching Layer* (PML) boundary conditions [69] has been used. Similar results have been found for the apertures with other eccentricities.

Chapter 6

Summary and Future Works

Within the framework of this dissertation, several radio frequency devices and components have been modeled and analyzed using commercial and non-commercial CEM tools. The components considered in this dissertation have very important and crucial practical applications in the field of particle accelerators and communication systems. These components have been chosen far apart from each other and belong to the category of the closed and open problems in CEM. Some numerical techniques have also been suggested and successfully applied to improve the numerical efficiency of a hybrid CEM technique to characterize radiating apertures.

As the first application, state-of-the art commercial CEM tools have been applied for the wakefield computations and related analysis of some components of the third generation synchrotron light source PETRA III. The considered components are the button-type BPMs in the normal beam-pipe, the same in the narrow beam-pipe and the longitudinal feedback cavity.

The wakefields, impedances, loss and kick parameters have been computed for the BPMs mounted in the normal beam-pipe and narrow beam-pipe. Wakes, related loss and kick parameters have been computed for the cases of on-axis and off-axis beam excitations. During the time-domain wake computations, the recorded electric field components at the gap between the BPM button and the beam-pipe suggest possible excitation of a mode with resonant frequency around 8.7 GHz. Detailed eigenmode analysis reveals that this mode is an almost degenerate dipole mode trapped in the vicinity of the BPM button - presented both in the normal and narrow beam-pipes. The estimated loss parameters, kick parameters, impedances etc. for these studies related to the BPMs can be used for the impedance database, to estimate the overall impedance of the machine.

The wake computation for the longitudinal feedback cavity show that the contributions of these cavities to the overall machine impedance is significantly high. A comparative study between the proposed feedback cavity with and without nose cone shows that the resonant frequency of the operating mode decreases slightly with the inclusion

6. Summary and Future Works

of the nose cone - which may be used for fine tuning the cavity resonant frequency. Although there are not much difference between the computed wakes for the cavity with and without nose cones, the shunt impedance can be increased by around 13% with the inclusion of the nose cones. It has been found that the terminations of the coaxial ports have strong influences on the impedance spectra of the cavity. With short circuits (electrical boundaries) at the coaxial ports, the frequencies of the impedance peaks shift towards lower values and the impedance peaks become higher compared to those with matched terminations at the same ports. Wakes and corresponding impedances due to the feedback cavity have been computed for both the cases of on and off-axis beam. As the feedback cavity has large dimensions combined with subtle geometrical details and the available computer memory is limited, it is very difficult to compute off-axis wakes with reasonable accuracies. For this purpose, a method has been suggested using one quarter of the cavity geometry and a combination of different boundary conditions at the symmetry planes. This method has been applied for small test cases to estimate the error bounds and afterwards used for off-axis wake computations due to the actual cavity.

The second application, i.e. the analysis of an ultra-wideband antenna, belongs to the category of open problems. The considered antenna has been analyzed and optimized using a commercial CEM tool. The complex shape of the antenna has been modeled using a general purpose mathematical tool. At first, the optimum simulation parameters (like the distance of the absorbing boundaries, the number of mesh-lines per wavelength, etc.) have been obtained from convergence studies. The main parameters influencing the antenna performance have been identified by means of parametric studies. Afterwards, these parameters has been used for optimization of the antenna. It has been shown that the antenna under analysis is a specially tapered TEM horn, with an added loop which eases the fabrication and minimizes reflection from the edge. The ultra-wideband nature of the antenna comes from the minimization of the edge reflections. A considerable deviation in the characteristics between the simulated antenna and the measured hand-curved one has been found. In spite of this deviation, which is most probably caused by the imperfections to fabricate the antenna shape, simulations along with the corresponding analysis provide an useful insight into the functioning of the antenna.

The presented antenna can be modeled with many degrees of freedom, besides those used in this dissertation. This work can be extended towards studies of those parameters on the antenna performance. Besides efforts can be made to manufacture the antenna taper more precisely, using the three dimensional rapid prototyping machines or other techniques.

The last part of the thesis is about the application of a hybrid technique involving the GMT and MMT for characterization of aperture antennas. This technique is based on the hybridization of a closed problem with an open one, based on the semi analytical techniques. Automatic multipole placement in the GMT generates an over-determined system with poor numerical stability. Two methods to identify the redundant multipoles in GMT have been presented and the numerical stability of the original system

and the modified systems obtained after eliminating the redundant multipoles (with both methods) has been analyzed. For the considered example of an elliptical horn antenna we have found that, for the SVD-angle approach, a threshold value of the order 10^{-3} is necessary in order to reduce the average error in the computed electric field. This threshold value provides an improvement in the condition number of the modified system as compared to the original one which has a condition number of the order 10^{11} . Similarly, when using the RRQR approach, the threshold necessary to reduce the average error in the electric field computation amounts to 10^{-6} . This has led to an improvement in the condition number of the order of 10^6 .

Elliptical apertures with different eccentricities have been analyzed and a comparison of the simulation results with a commercial electromagnetic simulation package has also been provided. Though the RRQR factorization is most suitable to reveal the numerical rank of a matrix where there is a significant gap in its singular value spectrum, still it can be applied for the redundant multipole elimination in GMT. In general, the RRQR decomposition is numerically less expensive than the SVD while the SVD is more robust. So, the SVD-angle method can be used for the cases where robustness is of primary concern and RRQR method can be used to obtain faster results. As these methods are general, their applications can also be extended to the automatic distribution of the multipoles for any complex geometries.

With the significant advancement of the computation speed and memory, the fully numerical computational electromagnetic techniques have become state of the art tools for modern day RF design and analysis - even for complex structures with large dimensions. The first two applications presented in this dissertation attest the scopes and capabilities of the modern computational electromagnetic tools. However, in case of open problems, the termination of computation domain still remain as a subject under investigation. The hybridization technique presented afterwards relies on subdividing the radiation problem into two parts - an internal and an external one. Although mode matching technique has been used in this dissertation to analyze the internal part, other techniques (like the fully numerical ones) can as well be used for the same purpose. Usually the fully numerical techniques at first compute the field distribution on a imaginary surface enclosing the antenna corresponding to the given antenna geometry and excitation. In the next step a near to far field transformation is applied to obtain the farfield distribution. This near to far field transformation can also be done efficiently using the GMT. Combination of a fully numerical technique (e.g. FIT, FEM etc.) as the computational tool for the internal part of the antenna with the GMT as the computational tool for farfield computations can be a promising extension of the present work.

Bibliography

- [1] J.C. Maxwell. A dynamical theory of the electromagnetic field. *Phil. Trans.*, 166:459–512, 1865. Reprinted in *The Scientific Papers of James Clerk Maxwell, volume 1*, New York, Dovevr, 1952, pp. 528-597.
- [2] J.C. Maxwell. *A Treatise on Electricity and Magnetism*, volume 1. Dover Publications, New York, 1954.
- [3] O. Heaviside. Electromagnetic induction and its propagation. *The Electrician*, 1885,1886 and 1887.
- [4] H.R. Hertz. *Electric Waves*. MacMillan, London, 1893.
- [5] N. Tesla. Experiments with alternate currents of high potential and high frequency. Lecture before the Institution of Electrical Engineers, February 1892. Reprint in: Lindsay Publications ISBN 0-917914-39-2 (1986).
- [6] J.C. Bose. On the determination of the wavelength of electric radiation by a diffraction grating. In *Royal Society*, volume 60, pages 167–178, London, 1897.
- [7] D.T. Emerson. The work of Jagadis Chandra Bose: 100 years of millimeter-wave research. *IEEE Transactions on Microwave Theory and Techniques*, 45(12):2267–2273, December 1997.
- [8] A.S. Popov. The apparatus for detecting and recording electrical oscillations. *Russian Physical and Chemical Society*, 28(1):1–14, 1896.
- [9] G. Marcony. Radio telegraphy. In *Proc. IRE*, volume 10, pages 215–238, 1922.
- [10] A. Einstein. Zur Elektrodynamik bewegter Körper. *Annalen der Physik*, 17:891–921, 1905.
- [11] A. Einstein. Die Grundlage der allgemeinen Relativitätstheorie. *Annalen der Physik*, 49:769–822, 1916.
- [12] B. Heim. *Elementarstrukturen der Materie*. Vol. 1 (revised). Resch Verlag, Innsbruck, 1989.
- [13] B. Heim. *Elementarstrukturen der Materie*. Vol. 2. Resch Verlag, Innsbruck, 1984.

BIBLIOGRAPHY

- [14] J.D. Barrow. *New Theories of Everything*. Oxford University Press, New York, 2007.
- [15] L.V. Kantorovich and V.I. Krylov. *Approximate Methods of Higher Analysis*. John Wiley and Sons, New York, 1964.
- [16] J.H. Richmond. Digital computer solutions of the rigorous equations for scattering problems. *Proceedings of the IEEE*, 53:796–804, August 1965.
- [17] R.F. Harrington. Matrix methods for field problems. *Proc. IEEE*, 55(2):136–149, February 1967.
- [18] R.F. Harrington. Origin and development of the method of moments for field computation. *IEEE Antenna and Propagation Magazine*, 32:31–35, June 1990.
- [19] M.D. Greenberg. *Applications of Green's Functions in Science and Engineering*. Prentice Hall, NJ, 1971.
- [20] S.M. Rao, editor. *Time Domain Electromagnetics*. Academic Press, San Diego, 2006.
- [21] FEKO, suite 5.3. <http://www.feko.info>, July 2007. EM Software & Systems.
- [22] SONNET, release 11. <http://www.sonnetsoftware.com>, 2007. Sonnet Software, Inc.
- [23] superNEC. <http://www.supernec.com>.
- [24] A. Taflove and S.C. Hagness. *Computational Electrodynamics: The Finite-Difference Time-Domain Method*. Artech House, 3rd edition, 2005.
- [25] A. Thom and C.J. Apelt. *Field computations in engineering and physics*. Van Nostrand, London, 1961.
- [26] K.S. Yee. Numerical solution of initial boundary-value problems involving maxwells equations in isotropic media. *IEEE Transactions on Antennas and Propagation*, AP-14:302307, 1966.
- [27] B. Engquist and A. Majda. Absorbing boundary conditions for the numerical simulation of waves. *Mathematics of Computation*, 31(139):629–651, July 1977.
- [28] J.P. Berenger. A perfectly matched layer for the absorption of electromagnetic waves. *Journal of Computational Physics*, 114:185–200, October 1994.
- [29] A. Farjadpour, D. Roundy, A. Rodriguez, M. Ibanescu, P. Bermel, J.D. Joannopoulos, S.G. Johnson, and G.W. Burr. Improving accuracy by subpixel smoothing in the finite-difference time domain. *Optics Letters*, 31(20):2972–2974, 2006.

- [30] EM explorer, version 4.0. <http://www.emexplorer.net>, 2007.
- [31] XFDTD, version 6.4. <http://www.remcom.com>, 2006. Remcom, Inc.
- [32] SEMCAD X, version 13.0. <http://www.semcad.com>, 2007. Schmid & Partner Engineering AG.
- [33] FIDELITY, version 5.0. <http://www.zeland.com>, 2006. Zeland Software, Inc.
- [34] EMPIRE, xcel 5.1. <http://www.empire.de>, 2007. IMST GmbH.
- [35] T. Weiland. A discretization method for the solution of maxwell's equations for six-component fields. *Electronics and Communication, (AEÜ)*, 31:116, 1977.
- [36] U. van Rienen. *Numerical Methods in Computational Electromagnetics*. Springer Verlag, Berlin, 2001.
- [37] CST microwave studio, version 5. <http://www.cst.com>, March 2005. CST GmbH.
- [38] MAFIA, release 4. <http://www.cst.com>, Nov 2004. CST GmbH.
- [39] A. Hrennikoff. Solutions of problems in elasticity by the framework method. *Journal of Applied Mechanics (Transactions of the ASME)*, 8:A169–A175, 1941.
- [40] R. Courant. Solutions of problems in elasticity by the framework method. *Bulletin of american mathematical society*, 49:1–23, 1943.
- [41] P. Silvester. Finite element solution of homogeneous waveguide problems. *Alta Frequenza*, 38:313–317, 1969.
- [42] HFSS, version 11. <http://www.ansoft.com>, 2007. Ansoft Corporation.
- [43] HFWorks, version 3.0. <http://www.electromagneticworks.com>, 2006. Electromagneticworks Inc.
- [44] RF MODULE, version 3.3. <http://www.comsol.com>, 2006. COMSOL, Inc.
- [45] W.J.R. Hofer. The transmission-line matrix method - theory and applications. *IEEE Transactions on Microwave Theory and Techniques*, MTT-33(10):882–893, October 1985.
- [46] C. Christopoulos. *The Transmission-Line modeling method (TLM)*. IEEE Press, New York, 1995.
- [47] P.B. Johns and R.L. Beurle. Numerical solution of 2-dimensional scattering problems using a transmission line matrix. *Proc. IEEE*, 118(9):1203–1208, September 1971.

BIBLIOGRAPHY

- [48] P.B. Johns. A symmetrical condensed node for the tlm method. *IEEE Transactions on Microwave Theory Techniques*, MTT-35:370–377, April 1987.
- [49] S. Lindenmeier, L. Pierantoni, and P. Russer. Hybrid space discretizing integral equation methods for numerical modeling of transient interference. *IEEE Transactions on Electromagnetic Compatibility*, 41(4):425–430, November 1999.
- [50] FLO/EMC, version 6.1. <http://www.flomerics.com>, 2005. FLOMERICS Group PLC .
- [51] MEFiSTo-3D Pro, version 4.0. <http://www.faustcorp.com>, 2005. FAUSTUS Scientific Corporation .
- [52] C. Hafner. *The Generalized Multipole Technique for Computational Electromagnetics*. Artech House, 1990.
- [53] R. Zaridze, D. Karkashadze, G. Ahvlediani, and J. Khatiashvili. Investigation of possibilities of the method of auxiliary sources in solution of two-dimensional electrodynamic problems. *Radiotechnics and Electronics*, 22(2), 1978.
- [54] Yu.A. Eremin, N.V. Orlov, and A.G. Sveshnikov. Electromagnetic scattering analysis based on discrete sources method. *Applied Computational Electromagnetics Society*, 9(3):46–56, 1994.
- [55] M.F. Iskander, A. Lakhtakia, and C.H. Durney. A new procedure for improving the solution stability and extending the frequency range of the EBCM. *IEEE Transactions on Antennas and Propagation*, 31(2):317–324, March 1983.
- [56] Ch. Hafner. MaX-1. John Wiley & Sons, November 1998. <http://max-1.ethz.ch/>.
- [57] N. Marcuvitz. *Waveguide Handbook*. (Vol. 10 of MIT Radiation Laboratory Series). McGraw-Hill Book Company Inc., New York, 1951.
- [58] A. Wexler. Solution of waveguide discontinuities by modal analysis. *IEEE Transactions on Microwave Theory and Techniques*, 15(9):508–517, september 1967.
- [59] G. Conciauro, M. Guglielmi, and R. Sorrentino. *Advanced Modal Analysis*. John Wiley and Sons LTD, 2000.
- [60] WASP-NET, version 4.0. <http://www.mig-germany.com>, 2002. MiG GmbH & Co. KG.
- [61] MATLAB, version 7.0. <http://www.mathworks.com>, 2005. The MathWorks Inc.
- [62] T. Weiland. A discretization method for the solution of maxwell’s equations for six-component fields. *Electronics and Communication, (AEÜ)*, 31:116, 1977.

-
- [63] R. Marklein. *Review of Radio Science: 1999-2002 URSI*, chapter The Finite Integration Technique as a General Tool to Compute Acoustic, Electromagnetic, Elastodynamic, and Coupled Wave Fields, pages 201–244. Wiley-IEEE Press, August 2002.
- [64] R. Marklein. *Numerische Verfahren zur Modellierung von akustischen, elektromagnetischen, elastischen und piezoelektrischen Wellenausbreitungsproblemen im Zeitbereich basierend auf der Finiten Integrationstechnik*. Shaker Verlag, Aachen, 1997.
- [65] Computer simulation technology. <http://www.cst.com>.
- [66] U.van Rienen. *Numerical Methods in Computational Electrodynamics Linear Systems in Practical Applications*. Springer, Berlin, 2001.
- [67] T. Weiland. Time domain electromagnetic field computation with finite difference methods. *International Journal of Numerical Modelling: Electronic Networks, Devices and Fields*, 9:295–319, 1996.
- [68] M. Clemens and T. Weiland. Discrete electromagnetism with the finite integration technique. *Progress In Electromagnetics Research*, 32:6587, 2001.
- [69] CST microwave studio - advanced topics. Version 5, 2005. CST GmbH.
- [70] R. Courant, K. Friedrichs¹, and H. Lewy¹. Über die partiellen Differenzgleichungen der mathematischen Physik. *Mathematische Annalen*, 100(1):32–74, 1928.
- [71] F.J. Harris. On the use of windows for harmonic analysis with the discrete fourier transform. *Proceedings of the IEEE*, 66(1):5183, 1978.
- [72] I. Daubechies. *Ten Lectures on Wavelets*. Society for Industrial and Applied Mathematics, 1992.
- [73] G. Mur. Absorbing boundary conditions for the finite-difference approximation of the time-domain electromagnetic field equations. *IEEE Transactions on Electromagnetic Compatibility*, EMC-23(4):377–382, 1981.
- [74] B. Engquist and A. Majda. Absorbing boundary conditions for the numerical simulation of waves. *Mathematics of Computation*, 31(139):629–651, 1977.
- [75] D.M. Sullivan. A simplified pml for use with the fdtd method. *IEEE Microwave and Guided Wave Letters*, 6(2):97–99, 1996.
- [76] T. Li, W. Sui, and M. Zhou. Extending PML absorbing boundary condition to truncate microstrip line in nonuniform 3D FDTD grid. *IEEE Transactions on Microwave Theory and Techniques*, 47:1771–1776, 1999.

BIBLIOGRAPHY

- [77] AutoCAD. <http://www.autodesk.de>. Autodesk Inc.
- [78] D.T. Attwood. *Soft X-Rays and Extreme Ultraviolet Radiation: Principles and Applications*. Cambridge University Press, New York, 1999.
- [79] A. Liénard. The electric and magnetic field produced by an electric charge concentrated at a point and in arbitrary motion (in french). *L'Éclairage Électrique*, 16, 1898.
- [80] G.A. Schott. *Electromagnetic Radiation*. Cambridge University Press, Cambridge, 1912.
- [81] T. Weiland and R. Wanzenberg. Wakefields and impedances. Joint US-CERN particle accelerator school, Hilton Head Island, SC, USA, November 1990. Edited by M. Dienes, M. Month and S. Turner.
- [82] A. Chao. *Physics of Collective Beam Instabilities in High Energy Accelerators*. John Wiley and Sons, New York, 1993.
- [83] P.B. WILSON. Introduction to wakefields and wake potentials. U.S. Particle Accelerator School, Batavia, Illinois, July-August 1987.
- [84] B.W. Zotter and S. Kheifets. *Impedances and Wakes in High Energy Particle Accelerators*. World Scientific, London, 1998.
- [85] T. Weiland. Parasitic energy loss due to cavities in PETRA. Internal Report M-81/04, DESY, 1981.
- [86] T. Weiland. PETRA's impedance. Internal Report M-81/23, DESY, 1981.
- [87] K. Balewski. Analyse der transversalen Moden-Kopplungsinstabilität für lokalisierte HF-Strukturen und ihre Kompensierbarkeit durch Rückkopplungssysteme. DESY 89-108, Aug. 1989.
- [88] K. Balewski, W. Brefeld, W. Decking, H. Franz, R. Röhlsberger, E. Weckert, Eds. PETRA III: A low emittance synchrotron radiation source. Technical Design Report, DESY 2004-035, February 2004.
- [89] P.B. WILSON. High energy electron LINACS: Applications to storage ring RF systems and linear colliders. SLAC-PUB-2884 (Revised), Stanford, California, November 1991.
- [90] H. Henke. Point charge passing a resonator with beam tubes. *Archiv für Elektrotechnik*, 69:271–277, 1986.
- [91] T. Weiland. Comment on wakefield computation in time domain. *Nuclear Instruments and Methods*, 216:31–34, 1983.

-
- [92] W.K.H Panofsky and W.A. Wenzel. Some considerations concerning the transverse deflection of charged particles in radio-frequency fields. *Review of Scientific Instruments*, 27:967, 1956.
- [93] M. Dohlus and A. Jöstingmeier. Private communications.
- [94] A. Jöstingmeier. Private communications.
- [95] J.N. Corlett, J. Johnson, G. Lambertson, and F. Voelker. Longitudinal and transverse feedback kickers for ALS. In *4th European Particle Accelerator Conference (EPAC)*, pages 1625–1627, London, June 1994.
- [96] R. Boni, A. Gallo, A. Ghigo, F. Marcellini, M. Serio, and M. Zobov. A waveguide overloaded cavity as longitudinal kicker for the dafne bunch-by-bunch feedback system. *Particle Accelerators*, 52:95–113, 1996.
- [97] L.H. Chang, W.K. Lau, and T.T. Yang. Development of the RF kicker for the longitudinal feedback system at SRRC. In *6th European Particle Accelerator Conference (EPAC)*, pages 1708–1710, Stockholm, June 1998.
- [98] M. Dehler. Private communications.
- [99] R. Wanzenberg. Private communications.
- [100] M. Dehler. Kicker design for the ELETTRA/SLS longitudinal multi-bunch feedback. In *8th European Particle Accelerator Conference (EPAC)*, pages 2070–2072, Paris, France, 2002.
- [101] C.A. Balanis. *Antenna Theory: Analysis and Design*. John Wiley and Sons, 2 edition, 1996.
- [102] J.F. Huang and C.W. Kuo. CPW-fed bow-tie slot antenna. *Microwave and Optical Technology Letters*, 19(5):358–360, 1998.
- [103] A. Teggtatz, A. Jöstingmeier, and A.S. Omar. A new TEM double-ridged horn antenna for ground penetrating radar applications. In *German Microwave Conference - GeMiC*, Karlsruhe, Germany, 2006.
- [104] P.J. Gibson. The vivaldi aerial. In *9th European Microwave Conference*, pages 101–105, Brighton, UK, 1979.
- [105] V.I. Koshelev, Y.A. Andreev, Y.I. Buyanov, V.V. Plisko, and K.N. Sukhushin. Ultrawideband transmitting antennas, arrays, and high power radiation sources. In E.L. Mokole, M. Kragalott, and K. R. Gerlach, editors, *Ultra-Wideband Short-Pulse Electromagnetics 6*, pages 357–367, 2003.
- [106] P.C. Waterman. Scattering by dielectric obstacles. *Alta Freq.*, 38:348–352, 1969. speciale.

BIBLIOGRAPHY

- [107] A.C. Ludwig. A comparison of spherical wave boundary value matching versus integral equation scattering solutions for a perfectly conducting body. *IEEE Transactions on Antennas and Propagation*, 34(7):857–865, July 1986.
- [108] J. Smajic, Ch. Hafner, and D. Erni. On the design of photonic crystal multiplexers. *Optics Express*, 11(6):566–571, March 2003.
- [109] J. Haueisen, Ch. Hafner, H. Nowak, and H. Brauer. Neuromagnetic field computation using the multiple multipole method. *International Journal of Numerical Modelling: Special Issue on Computational Magnetism*, 9:145–158, 1996.
- [110] N. Kuster. Multiple multipole method for simulating em problems involving biological bodies. *IEEE Transactions on Biomedical Engineering*, 40(7):611–620, July 1993.
- [111] E. Moreno, D. Erni, Ch. Hafner, and R. Vahldieck. Multiple multipole method with automatic multipole setting applied to the simulation of surface plasmons in metallic nanostructures. *Journal of the optical society of America A*, 19(1):101–111, January 2002.
- [112] A.S. Omar and E. Kuehn. Near field analysis of the modal scattering at radiating apertures. *International Journal of Electronics and Communications, (AEÜ)*, 55(5):355–362, 2001.
- [113] C. Tomassoni, M. Mongiardo, E. Kühn, and A.S. Omar. Generalized-multipole-technique - mode-matching-technique hybrid method for elliptical stepped horn antennas analysis. In *Proc. 31-st European Microwave Conference*, pages 433–436, ExCeL, London, September 2001.
- [114] E.M. Soriano. *MMP Modeling and Optimization of Photonic Crystals, Optical Devices, and Nanostructures*. PhD thesis, Swiss Federal Institute of Technology, Zurich, 2002.
- [115] K.I. Beshir and J.E. Richie. On the location and number of expansion centers for the generalized multipole technique. *IEEE Transactions on Electromagnetic Compatibility*, 38(2):177–180, May 1996.
- [116] A.K. Bandyopadhyay, C. Tomassoni, and A.S. Omar. A numerical approach for automatic detection of the multipoles responsible for ill conditioning in generalized multipole technique. In *Proc. IEEE MTT-S International Microwave Symposium*, Fort Worth, Texas, June 2004.
- [117] A.K. Bandyopadhyay, C. Tomassoni, M. Mongiardo, and A.S. Omar. Improving the numerical efficiency of generalized multipole technique by non-redundant multipole choices. In *The 20th Annual Review of Progress in Applied Computational Electromagnetics*, Syracuse, NY, April 2004.

BIBLIOGRAPHY

- [118] G.H. Golub and C.F. van Loan. *Matrix Computations*. Johns Hopkins University Press, 3 edition, 1996.
- [119] B.N. Datta. *Numerical Linear Algebra and Applications*. Brooks/Cole Publishing Company, 1995.
- [120] C.H. Bischof and G. Quintana-Ortí. Computing rank-revealing QR factorizations of dense matrices. *ACM Transactions on Mathematical Software*, 24(2):226–253, june 1998.
- [121] P. Morse and H. Feshbach. *Methods of Theoretical Physics*. McGraw Hill, 1953.
- [122] C.H. Bischof and G. Quintana-Ortí. Algorithm 782: Codes for rank-revealing QR factorizations of dense matrices. *ACM Transactions on Mathematical Software*, 24(2):254–257, june 1998.
- [123] E. Anderson, Z. Bai, C. Bischof, J. Demmel, J. Dongarra, J. Du Croz, A. Greenbaum, S. Hammarling, A. McKenney, and D. Sorensen. *LAPACK Users' Guide*. Society for Industrial and Applied Mathematics, 3rd edition, 2000.